Instrumented Indentation for Characterization of Irradiated Metals at Room and High Temperatures

Zur Erlangung des akademischen Grades

Doktor der Ingenieurwissenschaften

der Fakultät für Maschinenbau

Karlsruher Institut für Technologie (KIT)

genehmigte

Dissertation

von

Dipl.-Ing. Irène Sacksteder

aus Marseille, Frankreich

Abstract

The reliability and sustainability of future fusion power plants will highly depend on the aptitude of materials to withstand severe irradiation conditions induced by the burning plasma in reactors. The so-called reduced-activation ferritic-martensitic (RAFM) steels are the current promising candidates for the structural applications considering the reactor's first wall. These steels exhibit irradiation embrittlement and hardening for defined irradiation conditions that are mainly characterized by the irradiation temperature and the irradiation dose. A proper characterization of such irradiated steels implies the use of adapted mechanical testing tools. In the present study, the instrumented indentation technique makes use of a post-processing tool based on neural networks. This technique has been selected for its ability to examine tensile properties by multistage indents on miniaturized irradiated metallic samples. The steel specimens studied in this project have been neutron-irradiated up to a dose of 15 dpa. They have been subsequently tested at room temperature in a Hot Cell by means of an adapted commercial indentation device. The significant irradiation-induced hardening effect present in the range of 250-350 °C could be observed in the hardness and material's strength parameters. These two material parameters show a similar evolution with increasing irradiation temperatures. Post-irradiation annealing treatments of Eurofer97 have been realized and leads to a partial recovery of the irradiation damage.

Considering the demands for characterization in irradiated steels at high temperature and for post-irradiation annealing experiments, the existing instrumented indentation device has been further developed during this work. A conceptual design has been proposed for an indentation testing machine, operating at up to 650 °C, while remaining the critical temperature limit for tensile strength of the newly developed oxide dispersion strengthening ferritic-martensitic (ODS-RAFM) steel. A heating system as well as an optical sensing system have been both conceived for the high temperature testing facility. The former system relies on the use of cartridge heaters heating the sample and the indenter by thermal conductivity, and is further investigated by numerical analyses. The latter system is used for measuring the indentation depth at displacement resolutions up to 20 nm and is based upon an existing method of digital image processing. Two main parts feature the design suggested for the machine. The first one stands for the basic structure and the force application system, while the second makes the connection between the vacuum chamber, the heating-cooling and the sample positioning systems. The integrated vacuum chamber acts for a significant diminution of oxidation at the specimen and the tip. The final design of the machine takes into account the spatial constraints existing in a Hot Cell.

Kurzfassung

Sowohl die Zuverlässigkeit als auch die Nachhaltigkeit künftiger Kernfusionsreaktoren hängen stark von der Widerstandsfähigkeit ihrer Materialien gegen durch das Plasma hervorgerufene Bestrahlungsschädigungen ab. Die sogenannten niedrigaktivierbaren ferritisch-martensitischen (RAFM) Stähle sind die aktuell am besten geeigneten Strukturmaterialien zum Einsatz in der ersten Wand des Reaktors. Diese Stähle weisen ein bestrahlungsinduzierte Verfestigungs- und Versprödungsverhalten auf, das stark von Bestrahlungsdosis und-Temperatur abhängt. Zur Charakterisierung bestrahlter, radioaktiver Stahl-Proben werden Versuchsanlagen benötigt, die an diese Bedingungen speziell angepaßt sind. Die in der vorliegenden Arbeit angewandte Untersuchungsmethode basiert auf dem instrumentierten Eindringverfahren und ermöglicht die Bestimmung des Zugverhaltens anhand zyklischer Belastungen auf miniaturisierten Proben unter Verwendung einer Auswertemethode mittels neuronaler Netze.

Die untersuchten Stähle wurden zuvor bis zur Schädigung von ca. 15 dpa bei unterschiedlichen Temperaturen mit Neutronen bestrahlt. Anschließend wurden sie bei Raumtemperatur in einer Heißen Zelle mittels eines kommerziellen Eindringprüfstands getestet. Zwischen 250 und 350 °C entsteht ein erhebliches bestrahlungsinduziertes Verfestigungsverhalten, was über Härte bzw. Streckgrenze nachgewiesen wird. Nachbestrahlung-Ausheil-experimente wurden realisiert und haben zur Ausheilung der bestrahlungsinduzierten Schäden geführt.

Mit dem Ziel, die oben genannten Materialien bei hohen Temperaturen zu characterizieren und Nachbestrahlung-Ausheilexperimente durchzuführen, wurde im Rahmen dieses Projekts die bestehende Anlage für Eindruckversuche weiterentwickelt. Ein Konzept wird vorgeschlagen, anhand dessen eine maximale Betriebstemperatur von 650 °C erreicht wird. Diese entspricht der Grenztemperatur der Materialfestigkeit neu entwickelter Oxiddispersionsgehärteter (ODS-RAFM) Stähle. Zum Erreichen der Betriebstemperatur werden Heizpatronen verwendet, die durch Wärmeleitung die Probe und die Prüfkörper aufheizen. Die Eindringtiefe wird durch die optische Messung der Eindringkörperbewegung gemessen. Dieses Verfahren bietet mit einem digitalen Bildbearbeitungsprozess die erforderliche Wegauflösung bis zu 20 nm. Es wird ein Design der Maschine vorgestellt, das darüberhinaus aus zwei Hauptteilen besteht: zum einen die Basis-Struktur der Anlage für die Kraft Übertragung und-Messung, zum anderen die Einbindung einer Vakuumkammer mit dem Heiz-Kühl und Probenpositionierungs-System. Der Zweck der integrierten Vakuumkammer ist es, die Oxidation an der Probe und am Indenter deutlich zu reduzieren. Das endgültige Design der Maschine berücksichtigt die räumlichen Randbedingungen der Heißen Zelle, die zum Untersuchung radioaktiven Proben bedürtig ist.

Acknowledgments

Irène Sacksteder, May 2011

Contents

List of Symbols

α	(-)	Empirical constant
β	(-)	Work hardening parameter
γ	(m^{-2})	Initial work of slope hardening
η	(-)	Viscosity parameter
ϵ_e	(-)	Elastic strain
ϵ_i	(-)	Plastic strain
λ	(m^{-1})	Wavelength
ξ	(Pa)	Kinematic rate coefficient
a	(m^2)	Contact area
b	$(-)$	Kinematic hardening parameter
A	(m^2)	Contact area at maximal load
c	(m)	Length of the radial crack
c	(Pa)	Kinematic hardening parameter
C	$(\text{m} \cdot \text{N}^{-1})$	Constraint factor
C_m	$(\text{m} \cdot \text{N}^{-1})$	Machine compliance
C_{sp}	$(\text{m} \cdot \text{N}^{-1})$	Specimen mount compliance
C_{lf}	$(\text{m} \cdot \text{N}^{-1})$	Load frame compliance
d	(m)	Diagonal of Vickers residual indent
$DBTT$	(°C)	Ductile to brittle transition temperature
E	(Pa)	Specimen elastic modulus
E_a	(J)	Activation energy
E_i	(Pa)	Indenter elastic modulus
E_r	(Pa)	Reduced Young Modulus
F	(Pa)	Overstress
h	(m)	Indentation depth
h_0	(m)	Indentation depth at first cycle
h_c	(m)	Indenter contact depth
h_f	(m)	Final indentation depth
h_{max}	(m)	Maximal indentation depth
H	(Pa)	Hardness
H_v	$(\text{kgf} \cdot \text{mm}^{-2})$	Vickers hardness
k	(Pa)	Isotropic hardening

k	(Pa)	Rate coefficient
k_0	(Pa)	Yield stress
K_{IC}	$(\text{MPa} \cdot \text{m}^{\frac{1}{2}})$	Critical K_I
K_{ID}	$(\text{MPa} \cdot \text{m}^{\frac{1}{2}})$	Critical K_{IC}
K_C	$(\text{MPa} \cdot \text{m}^{\frac{1}{2}})$	Fracture toughness
L_P	(m)	Pixel's length
m	(-)	Viscosity exponent
n	(-)	Magnification
P	(N)	Applied indentation depth
P_0	(N)	Applied force for first indentation cycle
P_{max}	(N)	Maximal applied indentation depth
$\dot{P}$	$(\text{N} \cdot \text{s}^{-1})$	Loading rate
R	(m)	Ball indenter radius
R	$(\text{J}/(\text{mol} \cdot \text{K}))$	Gas constant
$R_{p0.2}$	(Pa)	Offset yield strength
S^*	$(\text{N} \cdot \text{m}^{-1})$	Contact stiffness
T	(°C)	Temperature
T_{irr}	(°C)	Irradiation temperature
USE	(J)	Upper Shell Energy
W_p	(J)	Plastic work of indentation
W_{tot}	(J)	Total work of indentation
W_u	(J)	Elastic work of indentation
Y	(Pa)	Flow stress in compression

Chapter 1

Introduction

1.1 General Research Context and Motivation

1.1.1 Nuclear Fusion

In the current context of increasing worldwide energy demand, nuclear fusion is considered to have a high potential as an energy source. The main goal is to convert the kinetic energy of neutrons released by the easiest realizable fusion reaction, Equation 1.1, of the two hydrogen isotopes deuterium and tritium inside the reactor into heat which will then be converted into electricity. This can be achieved either inside a tokamak configuration (see Figure 1.1) or a stellerator one in order to magnetically confine the plasma which needs to reach temperatures higher than 100 million degrees [1].

$$D^+ + T^+ \longrightarrow He^{++}(3.5\,MeV) + n(14.1\,MeV) \qquad (1.1)$$
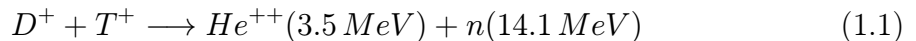
Research and development activities in this area started more than 50 years ago. Generally, the main issue is the improvement of the energy balance induced by the fusion reaction. The construction of new fusion reactors, such as ITER (International Thermonuclear Experimental Reactor) [2] and DEMO (DEMOnstration Power Plant) [3; 4] will allow demonstrating the technical feasibility of generating more than $500\,MW$ thermal power for extended periods of time and the possibility of producing continuous electricity.

1.1.2 Material for Nuclear Fusion

Focus on materials research and development for nuclear fusion applications remains one of the most important current activities to ensure the reliability and sustainability of reactors. The structure, defined by the reactor's first wall, is the first barrier exposed to the plasma, and is subject to harsh conditions, such as high temperatures, stress-strain histories as well as plasma particles and electromagnetic radiations. As shown in Figure 1.2, the radiation effects are mainly responsible for changes in the electrical, chemical, and mechanical properties. Regarding the mechanical properties, radiation damages generally imply embrittlement and hardening effects, leading to a degradation of fracture toughness, and irradiation-induced creep. On the other hand, the swelling effect issued from the helium production was found to be irrelevant for the case of the present studied low activation steels. The two main sources for radiation
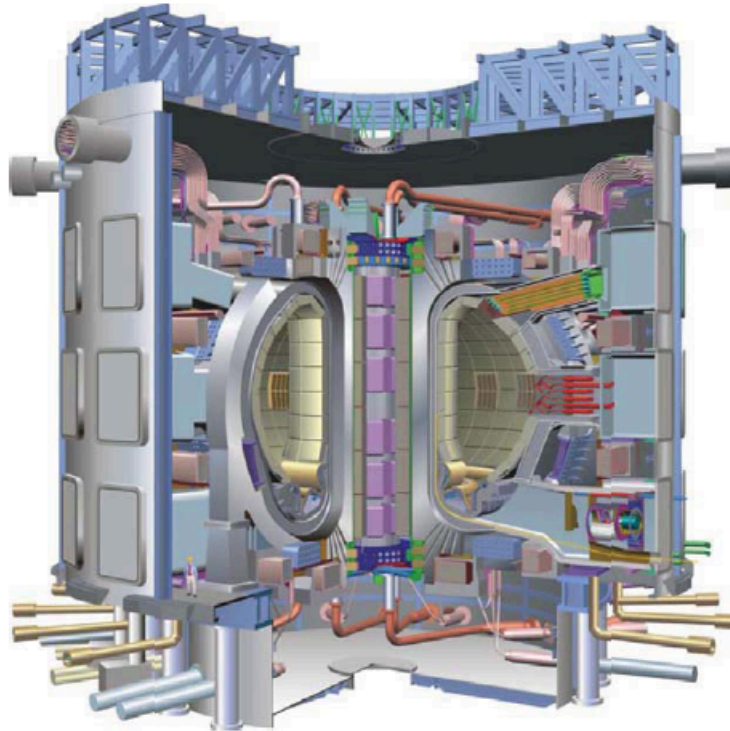
Figure 1.1: Nuclear Fusion reactor - ITER Tokamak [5]

damage having an impact on the mechanical properties are atomic displacement, also called "bulk damage", and transmutation. The former consists of atomic displacement cascades of the recoiling atoms which are originally produced by the interaction of the non-charged high-energy neutrons within the nuclei of the material [6]. The latter damage source is helium and hydrogen gas production which subsequently modifies the microstructure and, thus, the mechanical behavior of the original material [7].

The final material's irradiation defects depend upon the different irradiation parameters, such as temperature, T_{irr}, neutron fluence, and neutron spectrum, but also on the material's original properties, such as the chemical content and heat treatment. The neutron irradiation-induced damage is often defined by the total displacement induced in the material or displacements per atom (dpa). The resulting behavior of the materials has to be studied to validate the potential candidates for future use in a reactor or to improve them with regard to the specified requirements. The operation scheduled for the International Fusion Materials Irradiation Facility (IFMIF) aims at evaluating more precisely the materials' behaviors through post-irradiation examinations (PIEs). This facility will provide irradiations leading to a damage rate, a helium generation, and a hydrogen generation approaching the expected irradiation conditions present at the reactor's first wall (see Table 1.1) [8].
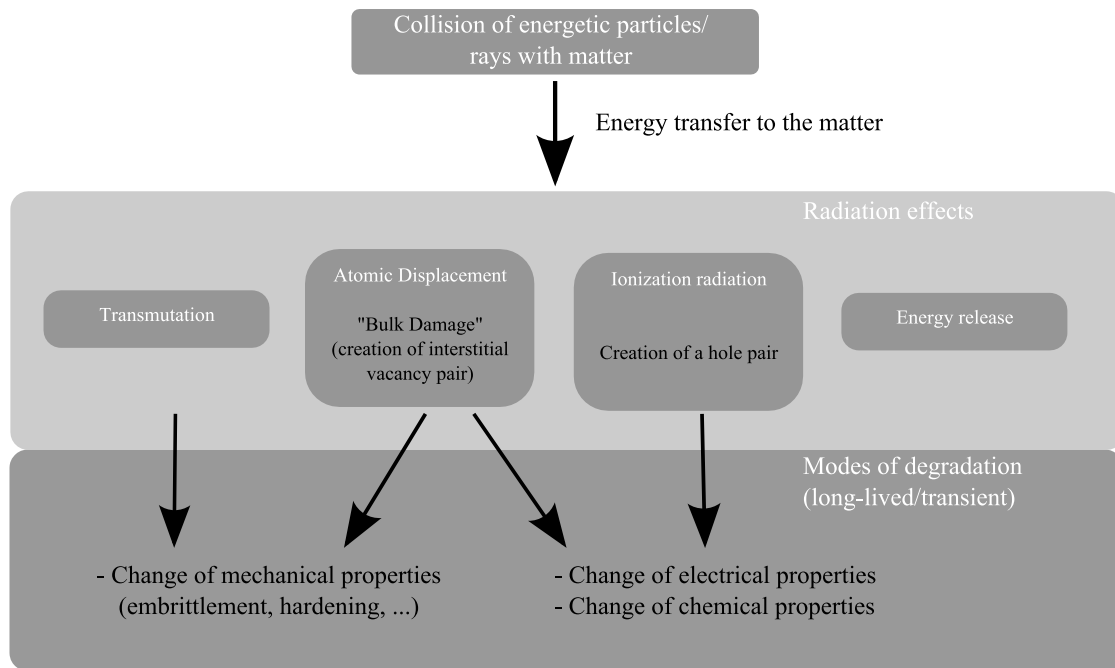
Figure 1.2: Radiation effects and degradation modes

Table 1.1: Irradiation conditions in reactors [8]

Defect production (in steels)	Fusion neutrons (3-4 GW reactor, first wall conditions)	Fission neutrons (BOR 60 reactor)	High-energy protons (590 MeV proton accelerator)	IFMIF (high flux test module)
Damage rate [dpa/year]	20-30	~ 20	~ 10	20-55
Helium [appm /dpa]	10-15	$\precsim 1$	~ 130	10-12
Hydrogen [appm/dpa]	40-50	$\precsim 10$	~ 800	40-50

1.1.3   Structural Materials for Fusion Reactors

Three main categories of materials are used in fusion reactors: plasma-facing, functional, and structural materials. The last family of materials ensures the basic structure at the reactor's first wall. Properties such as high strength, ductility and fracture toughness at relevant temperatures, good creep resistance over long periods of time, low activation, high erosion resistance, and high thermal conductivity, are particularly required for these structural materials. Low-activation materials are defined by a low level and fast decay of remaining activity after use [9]. Indeed, the amount of long half-life radioactivity can be significantly reduced by an appropriate selection of chemical elements so that the materials become innocuous after an approximate 100 yr decay period. The most promising candidates for the present application are the so-called reduced-activation ferritic-martensitic (RAFM) steels and the

oxide dispersion-strengthened RAFM-ODS steels that presently represent the best compromise between neutron irradiation strength, temperature strength, mechanical strength, and thermo-mechanical strength. However, the use of RAFM steels is still subject to a specific temperature range. This range is defined by irradiation-induced hardening and embrittlement effects below 625 K and the limited strength and loss of creep strength at temperatures above 825 K. This directly influences the outlet/inlet temperatures of the coolant and, thus, limits the reactor´s thermal efficiency.

1.2   Objectives and Proceedings

1.2.1   Irradiation of Materials

The samples investigated later in this study come from the irradiation campaign of the project SPICE standing for "SamPle Holder for Irradiation of Miniaturized Steel SpeCimEns" [10]. These irradiations were performed by the Institute for Energy (IE) of the Joint Research Centre (JRC) of the European Commission (EC) in the High Flux Reactor (HFR) in Petten [11], The Netherlands. The aim of this irradiation project was to evaluate the mechanical properties of samples after neutron irradiation up to a dose level of 15 dpa and at different irradiation temperatures. Specimens of Eurofer97, the European reference for reduced-activation ferritic-martensitic (RAFM) steel, and F82H-mod, the Japanese reference material, were irradiated in specific holders on different target temperature levels at 250, 300, 350, 400, and 450 °C. Three types of specimen holders were used; thus allowing the irradiation of miniaturized tensile, Charpy, and low-cycle fatigue (LCF) specimens as shown in Figure 1.3. The average neutron fluence of the irradiation experiment reached $10^{26} \, \text{m}^{-2}$ leading to an average induced damage level of 15 dpa. To this day, various types of PIE have been performed on samples irradiated at this irradiation dose [12; 13; 14; 15], previous experiments had been realized on samples irradiated in the HFR at lower doses in the framework of the MANITU programme [16; 17; 18].

1.2.2   Characterization of RAFM Steels

1.2.2.1   Suitability of the Indentation Method for the Characterization of RAFM Steels

The indentation technique has been selected for the characterization of irradiated materials. Besides the fact that this quasi non-destructive testing method requires small irradiated testing volumes only, a multiple use of already tested specimens is possible. This is of high interest, considering the high costs existing for irradiation volume. Furthermore, an post-processing tool based on neural networks and developed in recent years [19; 20; 21; 22], has proven to be capable of identifying the tensile behavior of metallic materials by interpreting data from sophisticated indentation experiments [23].
In this context, the irradiated volume corresponding to the specimen to be tested becomes relevant with regard to the damages induced by the neutron irradiation. Indeed, the method used for the identification of material parameters which is explained later in Section 3.3 assumes testing samples having a relative homogenous microstructure. The irradiation induced defects such as small point defects, clusters, dislocation loops,
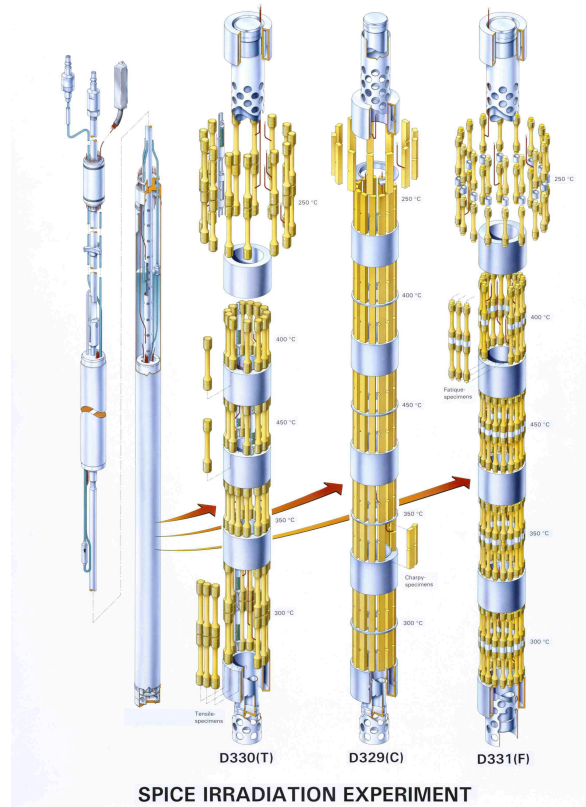
Figure 1.3: Irradiated SPICE specimens [10]

voids/bubbles or precipitates have to be diffused relatively homogenously in the material, in order to consider the size of the specimen to be acceptable for tests performed at the macro and micro scale. This assumption becomes realistic when considering the observations made by Klimenkov for Eurofer97 on SPICE transmission electron microscopy (TEM) samples irradiated at $300\,°C$ [24]. A defect size between 5 and 25 nm and a volume density of defects up to $4 \cdot 10^{21}\,m^{-3}$ were identified, thus leading to an estimated relative large number of defects of $1.3 \cdot 10^{9}$ in the average indented volume. Finally, the combination of this post-processing tool and an indentation device installed in a Hot Cell for radioactive sample testing makes the indentation technique attractive for the characterization of irradiated materials.

1.2.2.2 Characterization of RAFM Steels by Indentation

The materials investigated by indentation are RAFM steels, such as Eurofer97 and F82H-mod. Broken halves of tested miniaturized Charpy specimens are reused for the indentation tests. This project focuses on the study of phenomena, such as hardening and repairing of defects by heat treatment, with a view to define more accurately effects of irradiation on the material's behavior. Indentation results are also compared to tensile test results in order to analyze the differences between the two methods. Such experiments are carried out at the Fusion Materials Laboratory (FML) of the KIT's Institute for Applied Materials (IAM-WBM). A commercial indentation testing device (Zwick/Roell Z2.5) [25], operating at room temperature and accommodated in a Hot Cell designed for a sure enclosure of radioactivity and for protection of operators against radiation, allows carrying out post-analyses on the effects of irradiation dose

and irradiation temperature.

1.2.3   Development of a "Hot Indenter"

1.2.3.1   Development Needs

A more thorough comprehension regarding the mechanical behavior of irradiated steels at high temperatures is required. For this purpose, a new instrumented indentation device needs to be developed to perform tests on irradiated samples at high temperatures. The main purpose is to reproduce and characterize the mechanical behavior of irradiated materials subjected to high thermal loadings in the fusion reactor. The heating of materials should be achieved correspondingly with the range of operation temperatures of RAFM steels in future thermonuclear reactors. According to these criteria, a "hot indenter" needs to be developed for both heating of irradiated samples up to $650\,^{\circ}\mathrm{C}$ and measuring test parameters, such as force and indentation depth at high resolutions [26]. Furthermore, the indenter has to be adapted for a use in Hot Cells.

1.2.3.2   Challenges of Indentation at High Temperature

Generally, the challenge in high-temperature indentation is to manage the heat in the testing installation. Thermal drift occurs when thermal equilibrium is not achieved in the indentation system and leads to a virtual indentation displacement due to thermal expansion or contraction. As a result, such a phenomenon plays a significant role in the stability of the testing conditions and should be minimized for a good reproducibility of the measured data.

A relevant part of the instrument development resides in the adaptation of a suitable heating system and the limitation of warming at critical locations of the testing machine. Such critical areas are electronic units or transducers which are particularly sensitive to temperature elevations. They have to be protected effectively against the heat. Otherwise, the accuracy of the measurement may be affected significantly.

The control of a vacuum/neutral atmosphere within a sealed chamber is another important issue to be taken into account in order to prevent the specimens from oxidation. According to the thickness of the oxide layer formed at the surface of the indented specimen, changes of the mechanical behavior may be expected. This heat-induced effect is thus to be considered, when characterizing the material. In addition, the use of a sealed chamber will help minimize effects due to thermal drift.

An essential part of this project is to find and adapt a system measuring displacement for future integration within the high-temperature testing device. In relation to the force data, the displacement data obtained from the depth-sensing system during the test are required to assess the properties of the materials using the post-analysis tool based on neural networks. To ensure the reliability of the measurement, the displacement transducer will have to be sufficiently protected against thermal radiation.

1.3   Outline

Chapter 2 will introduce in general the technique of indentation. After giving an insight into the theory of indentation and its standard analysis method, the indenta-

tion instruments currently available on the market will be reviewed as well as their operation and technical specifications.

Chapter 3 will present the work in Hot Cells and some constraints regarding the remote handling of the equipment relevant to the construction of new devices. Then, the experimental procedure and the specificity of the analysis method used to determine the material parameters will be described. Additional details about the sources of uncertainties in indentation will be provided.

Chapter 4 will outline the work conducted with respect to the indentation of irradiated RAFM steels. The known irradiation effects will be introduced. Results concerning the measured hardness and the strength identified by the post-analysis tool will be detailed afterwards. Finally, a correlation between hardness and strength will be proposed for irradiated RAFM steels and a comparison between indentation results and tensile test results will be discussed in the last part.

Chapter 5 will present further research into irradiated materials. First, the use of the indentation technique for post-irradiation mechanical analyses of annealed specimens will be reported. According to the degradation of the fracture toughness in highly irradiated specimens, a first tentative assessment of fracture toughness will be made.

Chapter 6 will focus on the concept of the high-temperature indentation device to be developed and detail the functionalities of the relevant components after having outlined the force, displacement, heating, and vacuum requirements for indentation at high temperatures.

Chapter 7 will detail the principle of the heating system to be integrated in the high-temperature testing device. An initial overview of potential heating systems will be given, leading to the selection of one type of heating based on heat cartridge resistors. An analysis of the power required to separately heat the sample and the tip will be performed by means of numerical simulations for the given modeled configurations.

Chapter 8 will give an overview of existing linear displacement transducers and outline the principle of the selected optical measuring method based on digital image processing. An optical rig designed for adaptation to the high-temperature indentation machine will be proposed. Displacement analyses will be carried out and further improvements suggested.

Chapter 9 will cover the final design of the high-temperature indentation instrument based on the requirements mentioned and previously developed units. Machine operation will be reported as well as the characteristics of the main functional units.

Chapter 10 will summarize the research and development work accomplished and make recommendations for future work.

Chapter 2

State of the Art

Indentation is an attractive tool in the field of materials research and quality control inspections. The experimental technique of indentation combined with appropriate analysis methods is used to determine mechanical properties of a large range of materials from metals to polymers. This mechanical testing technique is particularly useful to study material's hardness and strength, residual stresses, time dependent behaviors, and even fracture toughness of brittle materials. In addition to that, indentation devices may offer other testing abilities such as scratching tests, fiber pushing, micropillar testing, or microelectromechanical systems (MEMS) testing. In this chapter, an introduction to the technique of indentation is given and shows the interest of the instrumented indentation technique (IIT). This part is then followed by an overview of technologies used in standard indentation devices, as well as a state of the art of existing equipments performing indentation at the nano or micro scale and operation at higher temperatures.

2.1 Technique of Indentation

2.1.1 Principle of Indentation

The indentation test is the application of a controlled load P through a hard indenter tip on the surface of a specimen. Generally, a diamond tip is used in order to test all types of materials. The resulting impression of the tip after unloading is conventionally used to measure the hardness (see Figure 2.1) that can be defined as the resistance of materials to plastic deformation.
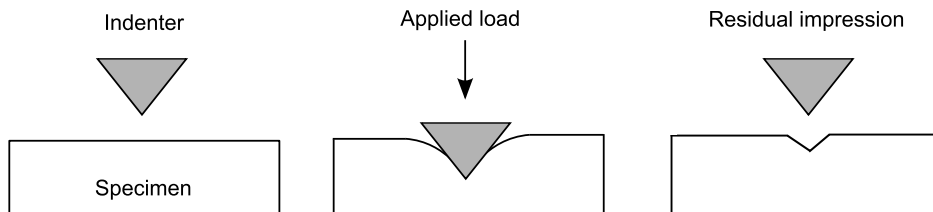
Figure 2.1: Hardness measurement principle

Conventional hardness tests consist in a single static force application for a corresponding dwell time, the output is a single indentation hardness value. Advanced techniques provide the measurement of the penetration depth h, down to the nano

scale, simultaneously with the measurement of the applied force P. Indentation testing devices characterized by this ability differ from traditional hardness ones and are referred to as the instrumented indentation technique (IIT), also called the depth-sensing indentation technique.

2.1.2   The Instrumented Indentation

Instrumented indentation testing machines have been developed because of their potential to evaluate, in addition to the hardness, several mechanical properties on the basis of the recorded indentation load-depth or P-h curve (see Figure 2.2). The interest for the development of such devices has notably grown according to the demands in investigation of thin films or surface layers with micron or submicron indentations [27; 28]. The simultaneous-continuous control and measure of P and h allow the application of a specified force or displacement histories. In general, a unique force-controlled cycle is carried out consisting of both a loading and an unloading phase with a constant loading rate $\dot{P}$. Other types of tests can be performed with the IIT such that several displacement-controlled cycles with additional relaxation phases, or force-controlled cycles with additional creep phases, respectively at constant displacement or loading rate can be applied in order to analyse the time dependent response of materials. The indentation procedure used in the present work makes use of such an experimental approach and will be more detailed in Chapter 3.
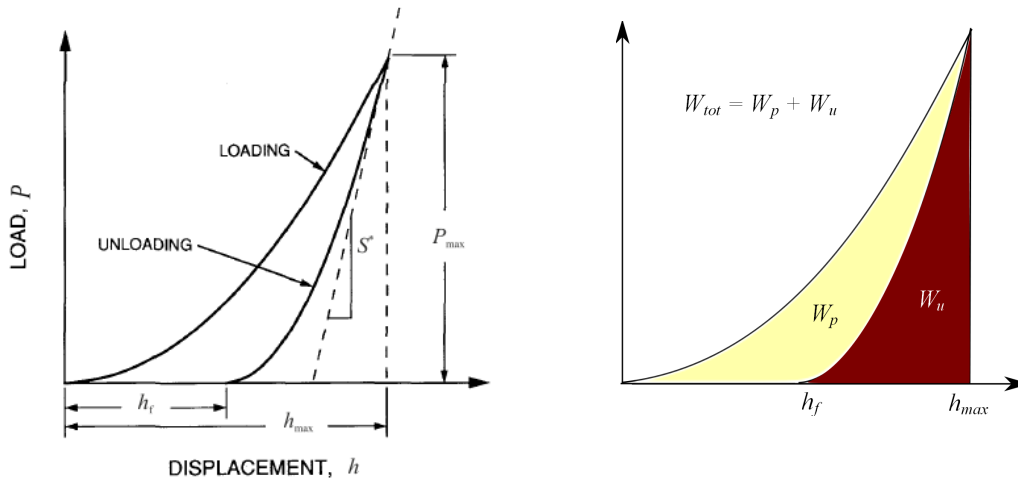
Figure 2.2: (a)Loading, unloading and contact stiffness, S^*, of an indentation load-displacement curve; (b) elastic work of indentation, W_u, and plastic work of indentation, W_p

One significant advantage of the IIT is that nearly all types of materials can be characterized thanks to the combination of high force-displacement resolutions associated with relative large ranges of applied forces and displacements. According to the fact that the load and the depth are continuously monitored, optical observations used for the measurement of residual impression areas are no longer absolutely necessary. Hardness can notably be determined by methods based on the calculation of the tip-sample contact area. Such methods are presented in the coming sections.

2.1.3   Standard Analysis Method of Experimental Data

The most successful model used for indentation data analysis is based on the Hertzian contact assuming that the unloading data result from a purely elastic contact. The contact between a ball and flat surface can be defined as follows [29]:

$$a^3 = \frac{3}{4} \times \frac{PR}{E_r} \qquad (2.1)$$

where a and R are the radius of contact and the ball, respectively, and E_r is the reduced Young's modulus defined later in Equation 2.5. Several approaches utilized for extracting mechanical material properties from experimental P-h curves were developed in the last 40 years. Most contributions came from Doerner and Nix [30], Oliver and Pharr [31] and Sneddon [32]. The approach presented in the following is known as the Oliver and Pharr approach and is widely-used in the domain of indentation.

The relationship between the force P and the indentation depth h for the unloading is given in the following form:

$$P = \alpha \cdot (h - h_f)^m \qquad (2.2)$$

Where P is the indenter load, h is the elastic displacement of the indenter, h_f is the final unloading depth as it is displayed in Figure 2.3, α and m are both geometric constants.
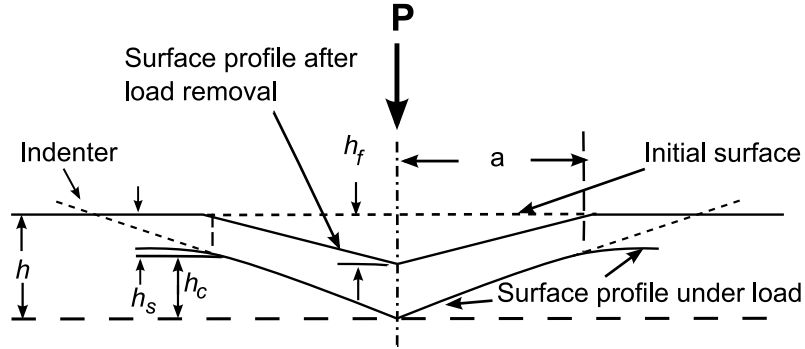
Figure 2.3: Schematic representation of the contact during indentation

Contrary to the loading portion involving both elastic and plastic behaviors, the unloading portion consists mainly of elastic recovery as it is visible in Figure 2.2. This portion is defined in Equation 2.3 by the total stiffness S^* which describes the slope of the tangent line to the unloading curve at the maximum loading point P_{max}.

$$S^* = \frac{dP}{dh} = \alpha \cdot m \cdot (h_{max} - h_f)^{m-1} \qquad (2.3)$$

Also, the total work W_{tot} of indentation results from a plastic contribution, W_p and an elastic one W_u, that recovers after unloading, and can be calculated by:

$$W_{tot} = \int P \cdot dh \qquad (2.4)$$

The way to identify the Young's modulus E of the investigated material was initially proposed by Tabor [33] who defined a reduced modulus, E_r in Equation 2.5. This additional modulus describes the elasticity of the contact between indenter and

specimen considering that the indenter tip is not perfectly rigid and elastically deforms.

$$\frac{1}{E_r} = \frac{(1 - \nu^2)}{E} + \frac{(1 - \nu_i^2)}{E_i} \tag{2.5}$$

where E and ν represent Young's modulus and Poisson's ratio of the specimen whereas E_i and ν_i characterize the same indenter properties. The calculation of E_r derives from the calculation of the contact stiffness S:

$$S = \frac{2}{\sqrt{\pi}} \cdot E_r \cdot \sqrt{A} \tag{2.6}$$

where A stands for the contact area at peak load. The contact stiffness S is determined from the experimentally measured total stiffness S^*. Indeed, the total compliance is related to the total stiffness S^* by $C^* = 1/S^*$ that includes the sample compliance $C = 1/S$ and the machine compliance C_m, which is based on the fact that the total measured indentation depth h is the result of the displacement of the machine and the sample.

$$C^* = C + C_m \tag{2.7}$$

This approach supposes to know the machine compliance C_m usually including the compliance of the load frame C_{lf} and the specimen mount C_{sp} [34].

$$C_m = C_{lf} + C_{sp} \tag{2.8}$$

Hardness

The hardness H is defined as the mean pressure the material supports under load [29] and can be thus determined from the projected area of contact, A, at the maximum load as shown in Equation 2.12. This implies to calculate previously the contact area at peak load by a tip area function from Equation 2.9 and Equation 2.10 at the maximal indentation depth and for a given geometry of the used tip.

$$h_c = h_{max} - \frac{\epsilon_i}{S^*} \left(\epsilon_i = 0.45 \text{ for Vickers} \right) \tag{2.9}$$

$$A = F(h_c) \tag{2.10}$$

$$H = \frac{P_{max}}{A} \tag{2.11}$$

It should be mentioned that this calculation method has been developed according to the fact that the residual hardness impression may correspond to a different plastic state than at the peak load. In addition to that, uncertainties regarding of the optical measure of the residual impression at the nano-scale become quite significant due to the resolution limitations of visualization standard techniques. Nevertheless, such errors of estimation of the residual impression area with optical measurement techniques have a lower impact on the final calculated hardness at the micro and macro-scale than at the nano-scale. A good approximation of the hardness at micro and macro scales takes into account the maximal applied load P_{max} and the area of the residual impression as it is defined in Equation 2.12 for the case of Vickers diamond hardness. Calculation of H_v hardness is performed in the present study by an
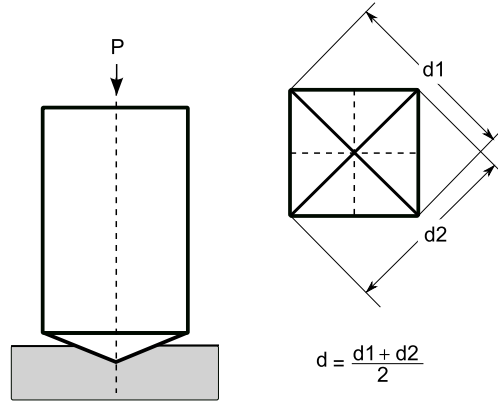
Figure 2.4: Residual impression of a Vickers indent (d is used for the optical measurement
of the Vickers hardness

optical measurement of the length of the diagonal from corner to corner on a Vickers
residual impression (see Figure 2.4).

$$H_v = \frac{2 \cdot P}{d^2} \cdot sin(\frac{136°}{2}) = \frac{1,854 \cdot P}{d^2} \qquad (2.12)$$

H_v is expressed in kgf·mm^{-2}.

2.2   Experimental Techniques

2.2.1   Standard Indentation System

Most of existing commercial instrumented indentation systems operate on the same
indentation principle, but may differ from each other by the use of different tech-
nologies. The main differences concern the systems used for application and measure
of force and displacement. A schematic of the global operating principle of standard
indentation systems is illustrated on Figure 2.5.
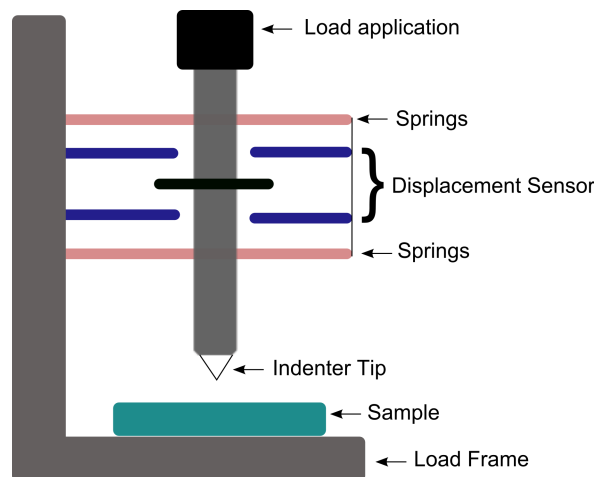
Figure 2.5: Schematic of indentation system

The design of an indentation system is generally broken down into four major
parts: the indenter, the loading system including the load application system as well as

the load frame, the displacement measuring system and the specimen mount system. For high temperatures testing conditions, a vacuum system as well as a temperature control system are additionally integrated. The functionalities of the different system parts are described in the coming sections.

2.2.2 System Units and Functionalities

2.2.2.1 Indenter

The common indenter geometries are sorted out according to their tip shapes as shown in Table 2.1.

Table 2.1: Indenter geometries

Indenter shape	Projected Area	Centerline-to-face Angle
Sphere	$\pi(2Rh_c\text{-}h_c{}^2)$	–
Vickers	$24h_c{}^2$	$68\,°$
cube corner	$2.598h_c{}^2$	$35.26\,°$

Generally, we distinguish sharp indenters from blunt indenters. Sharp indenters are commonly used to test relative hard materials. For an identical applied force, Vickers, Berkovich or cube corner indenters impose due to their smaller contact area higher stress at the indentation zone and thus more plastic strains than spherical indenters. Almost infinite stress is generated at the location of indentation so that the elastic deformation cannot be separated from the plastic one even at the beginning of indentation. In brittle materials, such sharp indenters can induce cracks which can be afterwards put into relation with the fracture toughness of the investigated material. On the contrary, spherical indenters, like for Rockwell indentation, induce smoother contacts and are usually used for softer materials. The stress field evolves as defined by Huber in a sphere-plan contact [35] (see Figure 2.6) with a distinguishable transition phase from elastic to plastic states. Therefore, indentation stress-strain curves can be derived from the load-displacement data and the yield point can be determined.
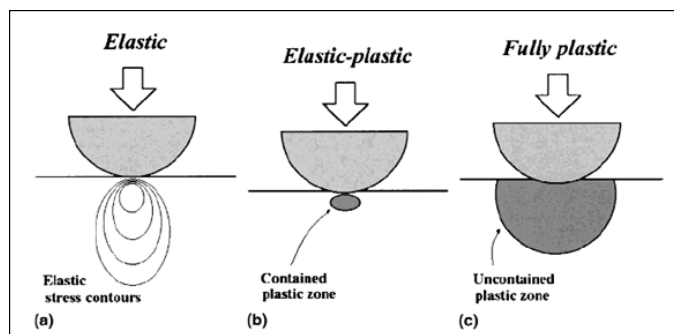
Figure 2.6: Elastic-plastic transition for ball indentation after Huber [35]

In this work, a Vickers indenter was employed for hardness measurement in metals, a Rockwell C (see Figure 2.7) was used for the procedure of assessment of elastic and plastic mechanical properties of the studied metals, and finally a cube corner was additionally used for cracks initiations in embrittled irradiated metals.
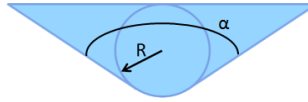
Figure 2.7: Rockwell C indenter geometry (Radius, R: 200 μm ±10 μm , angle, α: 120°
        $\pm0.35°$

2.2.2.2   Specimen Mounting/Positioning

The specimen mounting system holds the sample in a stable state for the indentation test. Especially in the domain of nanoindentation, samples are classically fixed by a thin layer of glue on the surface of a small hardened steel cylinder acting as specimen mount. Other techniques based on spring clamping, magnetic or vacuum chucks systems are also employed for that purpose. The specimen holder has to be selected taking into account the size of the samples to be tested, it has to provide means of securing the specimen, and finally it has to be stable enough to prevent itself from bouncing during indentation. The manufacturing of a flat testing surface and the parallelism of faces are essential. As mentioned in [34], a coplanarity of 20 µm over 10 mm is acceptable. Additionally, the specimen positioning system allows the motion of the specimen for the definition of indentation sites at the surface of the sample. Positioning units commonly used are motorized cross-tables allowing displacement in both X and Y axis. In certain cases, the positioning in the Z axis is also provided. If it is not the case, the positioning of the loading shaft has to be designed in order to provide different height positioning states.

2.2.2.3   Force Actuation

A loading system is needed to generate the required force of indentation. The loading system is composed of a force actuator, a force control electronic and a force transfer body corresponding to the indenter shaft in the case of indentation. Technologies based upon electromagnetic or piezo-electric actuation are often used in the field of indentation.
Such systems are selected considering the requirements in positioning range, accuracy and resolution. The former type of system is mostly used in macroindentation according to its long displacement range ability, while electrostatic or piezo-electric systems are more suitable in the field of micro or nanoindentation for application of force at high force resolution.

2.2.2.4   Displacement and Force Sensing System

Force and displacement sensing units are also required for forced-controlled and displacement-controlled indentation tests. Load cells made up of a strain gauge are commonly used in mechanical testing device as force sensing unit. Displacement sensing systems are capacitive inductive, resistive and optical systems. The selection of a transducer is principally made according to its metrological characteristics such as the measuring range, accuracy, resolution.

2.2.2.5   Imaging System

Before starting an indentation test, the location of the indent has to be well defined. This is commonly carried out by a viewing system integrated to the indentation equipment. It is composed of an optical microscope related to a camera which transmits a live image to the computer monitor. The hardness can be automatically calculated thanks to the optical measure of the indent´s dimensions. The optical microscope provides lenses usually from $\times 5$ to $\times 20$, and $\times 40$, $\times 60$ objectives. The microscope has to be positioned in the setup in a way that it does not need any further realignment of the specimen.

2.2.2.6   Vacuum System

At high temperatures, the kinetics of atmospheric reactions increases. Especially in ambient air, such reactions lead to the formation of oxide for most materials. On the contrary, a vacuum atmosphere helps minimizing the amount of oxygen present in the testing room and thus notably prevents the oxidation of the tested sample. This allows a more appropriate analysis of the original materials mechanical properties. Vacuum pumps and inert gas pumping systems provide a clean atmosphere inside the vacuum chamber. High vacuum (HV) and ultra high vacuum (UHV), respectively starting from a pressure of 10^{-3} mbar and 10^{-9} mbar, are mostly used in the indentation technique, where UHV is more relevant for applications at testing temperatures over $1000\,°C$.

2.2.2.7   Temperature Monitoring and Control System

The indentation testing device can be equipped of a heating module, when the material´s mechanical behaviour has to be investigated at high temperature as it is the case in this study. The heating module has the function to heat the sample at the required temperature; an additional module can be needed for the tip for more accurate applications of temperature testing conditions. In such a case, a set of units for heating, temperature measurement, and temperature control is primordial for the continuous monitoring and control of the applied temperature. The technologies are various depending on the type of application. More details about existing heating systems are provided in Chapter 7.

2.2.2.8   Computer

A computer is used for the monitoring and acquisition of measured data. The indentation instrument is usually related to the monitoring software of the instrument's company which notably stands for the visualization of force-displacement curve of the in-situ test and which provides an option to extract the recorded data. Nowadays, no particular high computer performances are necessary for in-situ indentation tests.

2.3   Indentation Instruments

2.3.1   Review of Commercial Instruments

Table 2.2 gives an overview of characteristics of the most used commercial instrumented indentation devices [36] [34]. This listing is not exclusive and custom appara-

Table 2.2: Main characteristics of commercial instrumented indentation devices

Type of indentation instrument	Indentation scale	Force factor	Displacement transducer	Force range / resolution	Displacement range / resolution	Heating system
Zwick/Roell, "ZHU/Zwicki Z2.5"	Macro-Micro	Electromagnetic	Incremental encoder	200 N ±0.01%	250 µm/ 20 nm	Room temperature
MTS (now Agilent), System Corporation, "Nanoindenter"	Nano	Electromagnetic	Capacitive	500 mN/ <75 nN	500 µm/ <0.02 nm	up to 300 °C
Hysintron Inc., "Triboindenter"	Nano-Micro	Piezoelectric	Capacitive	30 mN-5 N/ 1 nN-0.35 µN	10-80 µm/ 0.3 nm	up to 410 °C
MicroMaterials, "NanoTest"	Nano-Micro	Electromagnetic	Capacitive	20 N/ <60 µN	100 µm/ 0.1 nm	up to 500 °C
CSM Instruments, "Nano-Hardness Tester"	Nano-Micro	Electromagnetic	Capacitive	300 mN-30 N/ 1 µN-0.3 mN	200 µm/ 0.3 nm	up to 450 °C
CSIRO, UMIS	Nano-Micro	Piezoelectric	Inductive (LVDT)	50-500 mN/ 500 nN	2-20 µm/ 0.03 nm	up to 500 °C
Michalex, ONERA device	Micro	Piezoelectric	Capacitive	3 N / 1 mN	-/ 20-30 nm	up to 1000 °C

tuses are not listed.

In the last years, more interest has been accorded to the development of nanoindentation instruments. This is notably explained by the fact that there is a need to investigate the mechanical material's behavior at a lower scale for characterization of thin films structure of several nanometers. As a consequence, it is seldom to find commercialized instrumented indentation devices which are adapted for tests at both the micro-and macrometer scales. One exception is the Z2.5 device of the german manufacturer Zwick, for which a description is given in the indentation procedure of Chapter 3. Both micro-and nanoindentation devices are included in the list. The listed technologies can be of interest for the development of the indentation device within this study according to the fact that some of them are suitable for testing at larger scales.

Similarities concerning technologies of sensing and controlling units can be identified. Electromagnetic coil and piezo-actuator systems are most commonly systems used to generate the load. Capacitance technologies are also often employed for the measurement of indentation depth at subnanometer resolutions. Additionally, most of the devices integrate an antivibration stage for a better stability during the measurement. Specific characteristics of the selected instruments are mentioned in the following.

The Hysitron and the MicroMaterials Ltd instrument provide the maximum loading of 30 N and 20 N of all listed devices. Moreover, the latter one is based on a pendulum system so that the indentation axis is reversed and remains in a vertical orientation contrary to the other presented instruments belonging to the category of axial-loading instruments.

The MTS instrument provides the finest depth resolution of all listed instruments, and is mainly characterized by its abilities to measure continuously the hardness and the Young's modulus along the indentation depth by taking the evolution of the contact stiffness during the test into account [31] [37].

The specificity of the UMIS indentation device remains in its efficiency in minimizing thermal drift and vibration disturbances by means of a specified housing and anti-vibration module.

All listed devices perform tests at room temperature and provide an additional heating module for the elevated temperature. The temperature range of the Hysitron and CSM instrument is limited to a maximum temperature of 450 °C [38] [39], both

UMIS-2000 and MicroMaterials Ltd integrate a heating stage providing temperatures up to ca. 500 °C, whereas the Michalex-ONERA machine has developed micro ovens reaching a temperature of more than 1000 °C at the location of the sample and the tip and remains therefore till now the instrument with the highest temperatures. Further information about the operating principles and the used technologies of selected indentation instruments, representative of the current technologies used in the indentation field, are given in the next section.

2.3.2   Operation Principle of Indentation Instruments

NanoTest Micro Materials Ltd.

A schematic of the MicroMaterials Ltd (Werscham, United Kingdom) pendulum loading system is provided in Figure 2.8. The load is applied through an electromagnetic coil allowing the deflection of the pendulum pushing the tip towards the sample at its turn. A capacitor plates system is integrated at the indenter and used for the measure of indentation depths. The MicroMaterials instrument operating at up to 500 °C is based upon the same loading principle (see Figure 2.8) [40]. In this system, both samples and tip are heated in air atmosphere by resistance heaters in order to ensure thermal stability before the beginning of the experiment. By this way, thermal expansion in the pendulum can be significantly reduced and stabilized. The protection of the capacitor depth-sensing electronics is carried by the use of a static aluminum heat shield.
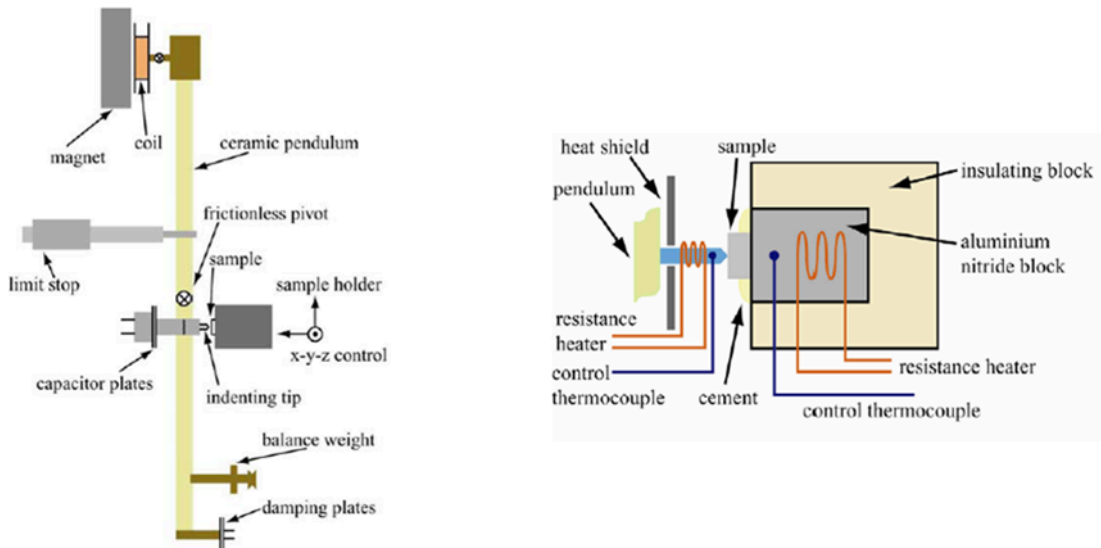
Figure 2.8: Principle of operation of the MicroMaterials Ltd instrument [41]

MTS Nano-Indenter II

The mounting stage of the MTS nanoindenter is controlled by an electro-motorized spindle drive system allowing a motion of the sample in the three space directions with an accuracy of 0.2 μm. The testing machine integrates a standard light microscope with an additional AFM (atomic force microscopy) module for accurate measurements of indents topography at the nanometer scale. It is also pneumatically damped in order
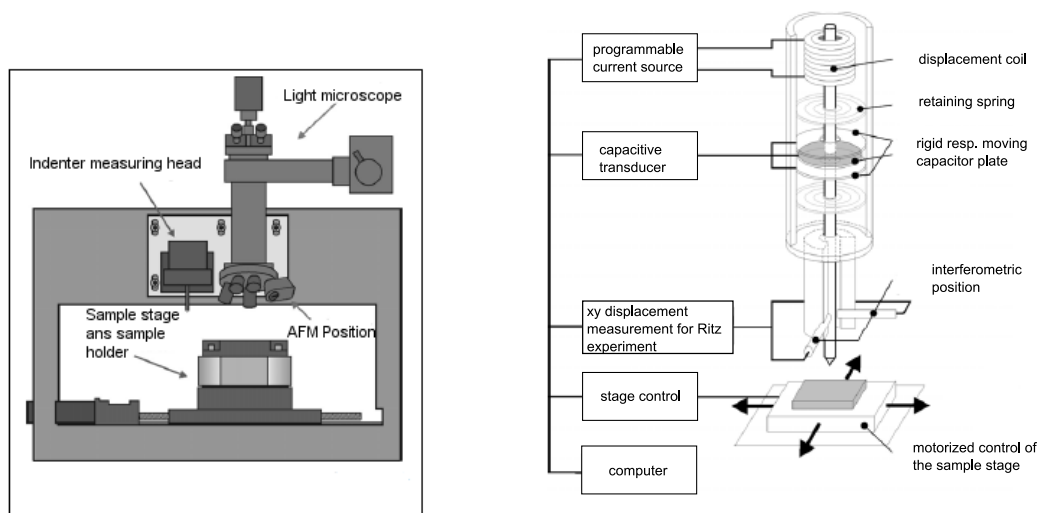
Figure 2.9: MTS NanoIndenter device and principle of operation

to minimize effects due to vibrations and temperature variations. The indenter is an independent part mounted to indenting shaft which is removable.

In Figure 2.9, it is illustrated that the force is induced from an electromagnetic coil. A current is passed through a coil so that the force at the indenting shaft is controlled by the regulation of current at the magnetic core system. The resolution of force measurement is of $75\,nN$ for a force range of $500\,mN$. The displacement of the indenter shaft is generated by the force acting against the retaining spring. The initial contact with the specimen is then detected by a discontinuity of the stiffness; during the indentation, the occurring displacement is allowed by the spring's elongation and results both from the constant stiffness of the retaining spring and the stiffness of the specimen. The measurement of the indention depth is effectuated by a three plates-capacitive sensor. The achieved displacement resolution is of $0.02\,nm$. The middle plate is directly attached to the shaft and thus follows its motion. The two other sensor plates are fixed to the shaft's housing itself attached to the frame of the machine. The position of the shaft is finally detected through the variations of voltage induced by the motion of the middle plate of the three-plates capacitor.

UMIS-2000 Nanoindenter:

The UMIS-2000 instrument (Fischer-Cripps Laboratories, Austrialia) [42] is based on a robust design with small compliance; it has been also developed to be less sensitive to thermal drift and vibrations. The nanoindenter integrates an anti-vibration stage. Moreover, it is housed in an electric conductive lagged enclosure to minimize sensitivity to thermal drift, thus leading to a drift rate of $0.01\,mm{\cdot}s^{-1}$ in a temperature environment of $2\,K$ variations.

The working principle is illustrated in Figure 2.10. A variable load is applied by means of a piezo driver. It expands or contracts by varying the applied voltage using a closed loop control for the applied force. The driver induces by this way the motion of the main carriage fixed at its bottom by a spring element, which finally generates the parallel motion of the indenter shaft directly attached to the main carriage by means of
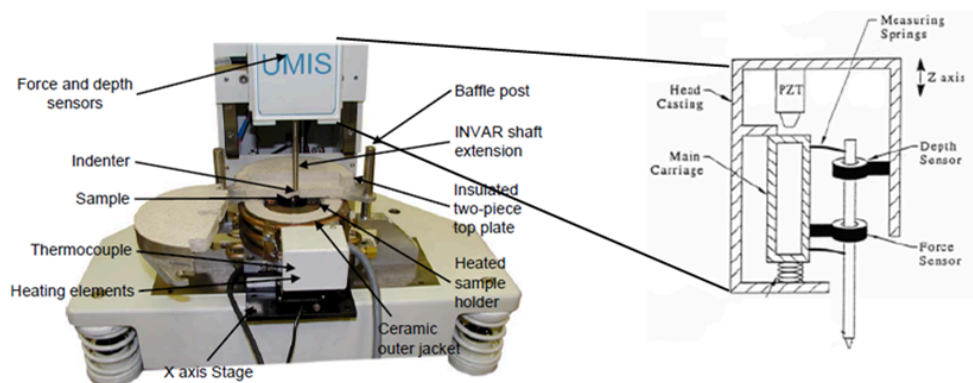
Figure 2.10: UMIS-2000 Nanoindenter device and principle of operation [42]

two leaf springs. The measurement of the force and the displacement are performed by two separate linear variable differential transformer (LVDT) transducers. The depth sensor is attached to the frame, whereas the force one is attached to the main carriage and both surround the moving shaft. The measurement of the shaft position is made by monitoring the deflection of the upper elastic spring both linked to the shaft and the main carriage. The measurement of the applied force is carried out by the lower sensor detecting the deflection of the lower leaf spring when contact occurs at the surface of the sample. The datum of the contact detection is then recorded and in parallel the depth output of the upper transducer is put to zero as reference for the start of the depth indentation measurement.

The UMIS instrument disposes of an optional 500 °C hot stage for the heating of the sample. In that case, the tip is not heated and the specimen has to be held in contact with it during several hours or days if necessary to reach the thermal equilibrium between both units. The electronic force feedback control of the instrument ensures for that purpose the initial contact force to be maintained when thermal strains occur at the heated parts. The heating module is composed of cartridge heaters and a sample holder fixed on a silica ring. A ceramic insulation encloses the whole heating unit. Additionally, water cooling is provided at the outer ceramic casing for a better temperature stability. The monitoring and control of the heaters is carried out by a Eurotherm controller that receives thermal signals from K-type thermocouples. A shaft made of Invar has been manufactured to minimize thermal expansion and contraction at the indentation area.

Michalex-ONERA Microindenter:

The indentation instrument has been recently developed at the ONERA research center [43; 44] and has been commercialized by the company Michalex (France). This equipment is adapted to perform tests up to 1000 °C, and even more up to 1200 °C in a more recent version. This has been realized by the development of micro-furnaces

surrounding both the sample and the indenter. The whole heating system provides a temperature stability of $\pm\,2\,°C$ and a heating rate of $10\,°C.\text{min}^{-1}$. A translation stage authorizing motion of the sample in X and Y axis at a resolution of ca. $1\,\mu m$ is used as base to fix the sample holder, the sample, the furnace and also the load sensor. The whole setup is integrated in a vacuum chamber equipped with a cooling system. The cooling system has notably the function to protect the inside electronic units from heating. Thermal drift is minimized on displacement and load sensors when stabilizing them thermally by flowing water. A primary vacuum of $5\times10^{-2}\,\text{Pa}$ is carried out by the use of a Roots pump combined with a turbomolecular pump, and a neutral atmosphere is ensured by the introduction of pure argon in the chamber. In the Michalex indentation system, the load is applied by means of a piezo actuator which ensures the displacement of the indenter and its penetration into the sample up to a maximum force of $3\,N$. The force signal is continuously measured at a resolution of ca. $1\,mN$ by a strain gauge sensor and corrected by the piezo system by means of a feedback regulation. The measurement of the indenter displacement is carried out by the use of a differential capacitive technology offering a displacement resolution of the instrument of $20\,nm$ at room temperature and $30\,nm$ at $1000\,°C$. Finally, the instrument is additionally equipped with a microscope, including a motorized focussing in the Z axis, and a camera for the visualization of indents at high temperatures.
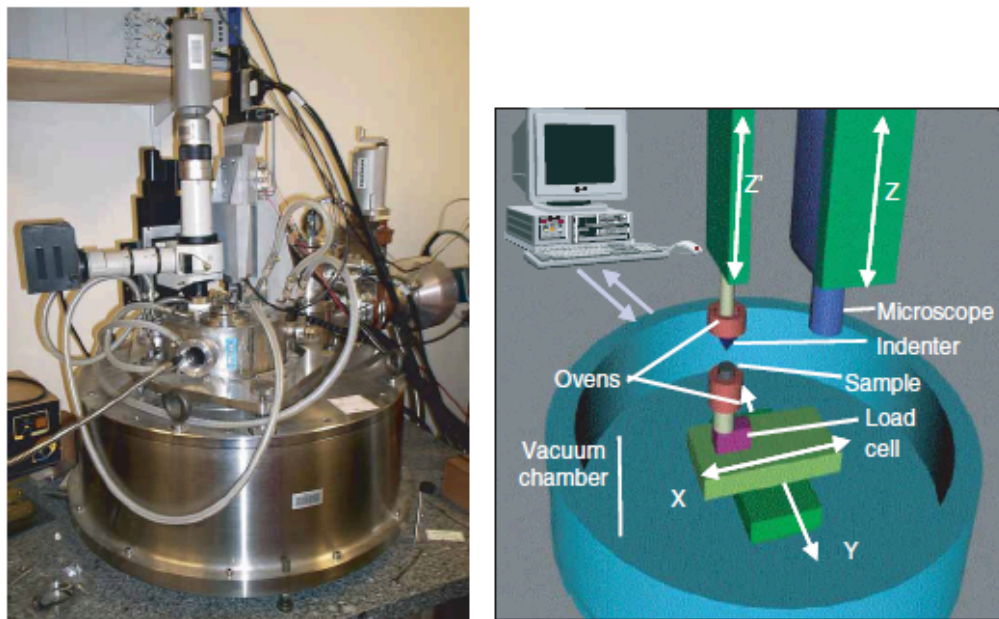
Figure 2.11: ONERA indentation device [43]

Chapter 3

Indentation Procedure

3.1 Facilities

3.1.1 Hot Cells

Investigations on irradiated materials are realized in specified laboratory conditions. In the Fusion Materials Laboratory (FML), the irradiated materials are handled inside working stations also called "Hot Cells" [45]. To protect operators and environment from the radiation of irradiated and thus activated specimens, such cells, in particularly the one where the indentation testing device is installed, have been specifically designed to reduce significantly the exposure to gamma radiations emanating from the irradiated samples to be tested. The Hot Cell consists of a lead shielding of 200 mm and 500 mm of a specific lead glass used for inspection inside the box (see Figure 3.1). The usual radiation dose of the tested irradiated indentation specimens is of $180\,\mathrm{mSv\cdot h^{-1}}$ in contact, five of such irradiated samples are allowed to be deposited in the Hot Cell, otherwise the radiation exposition is too high for glass and electronic components. This protection measure has its importance if considering the observed lifetime decrease of electrical and optical apparatuses submitted to irradiation [46; 47]. Apparatuses such as glasses and transistors are particularly affected from radiation exposure [48]. Standard glasses exposed to radiations lose their transmittance properties until a dose rate of ca. 100 Gy. Using a standard glass would lead to a lifetime of approximately 1000 h for an exposure corresponding to 1000 tests with the tested indentation specimens. For that reason, apparatuses used in Hot Cells have to be carefully selected or if possible additionally protected from radiations.

The inner housing of the cell is made of stainless steel and prohibits the diffusion of contamination. The filters integrated to the air conditioning system have the function of protecting against released radioactive particles or more generally radioactive aerosols coming from the radioactive matter. The Hot Cells are gas tight so that all the radioactive particles remain confined into the box in case of a failure of the ventilation system - a depression of 3 mbar is always maintained in the cell to prevent diffusion of radioactivity in case of leakage or the cell. An additional system of nitrogen filling inside the box is also provided for needs in working conditions requiring a small amount of oxygen in the box, $0.5\,\%$ of O_2 volume concentration can be reached with this system in approximately one hour.

Furthermore, it has to be noted that the handling in such boxes is generally enabled by to the use of two manipulators. In the Hot Cells of the FML, such manipulators
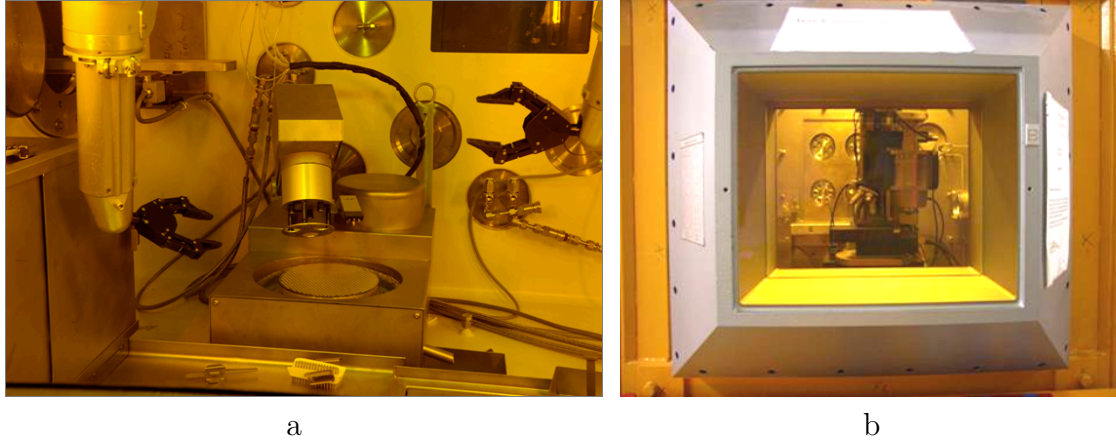
Figure 3.1: Hot Cell: (a) Inside of the metallography cell (polish apparatus, two manipulators), (b) Outside of the indentation cell (lead box, lead inspection glass, indentation device, two manipulators)

consist of two clamping fingers (see Figure 3.1); this implies that all the devices inserted inside the cell have to be thought as remote handling equipment to ensure simple and low time consuming remote handling action. This aspect as well as the limitation of access with the manipulators to certain areas of the cell point out the high importance that is to be attached for the design of devices employed in Hot Cells.

3.1.2   Equipment for Indentation Investigations

3.1.2.1   Specimen Preparation

As the indentation method only requires small testing volumes, the miniaturized Charpy specimens of the SPICE irradiation program are adapted for the present application. The two broken halves of irradiated KLST Charpy-V notched specimens (see Figure 3.2) are reused for indentation tests (see Figure 3.3). Indeed, such specimens are only damaged at one end, but the main part of each specimen remains undamaged. In order to significantly minimize the effects of deformation of the broken side, the indentation tests are not performed in the last 3 mm of the damaged side. As shown in Section 3.2, a specimen holder was specially designed for this geometry.

The samples are mechanically polished to get a flat mirror surface. Samples were initially polished in a final step with diamond suspension grain size of 3 μm [49]. It has been considered that for a maximum indentation depth of approximately 30 μm, surface effects may affect the course of the indentation P-h curve and consequently the assessment of the material parameters. For further improvement, the best surface quality has been achieved by using an aluminum oxide polishing suspension with 0.02 μm grain size.

According to ISO 14577 [50] for instrumented indentation tests, ball indentations with an average residual impression of 175 μm as it is the case here for Eurofer97 up to a force of ca. 50 N require a spacing of ca. 1 mm. In section 3.4, further numerical simulations were made to analyze the changes in the residual stress-state after indentation up to 20 μm. The total number of ball and pyramid type indents per sample was then restricted to less than 8 considering the total length of the small-sized Charpy specimen.
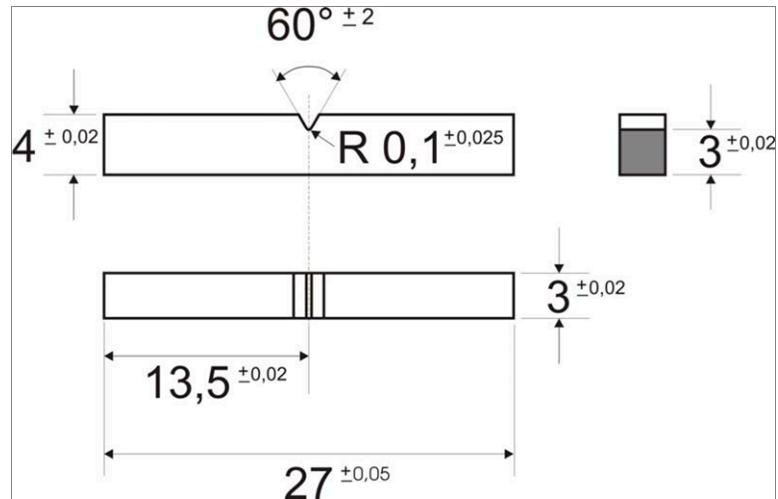
Figure 3.2: KLST-Charpy specimen dimensions used for indentation tests

a   b   c
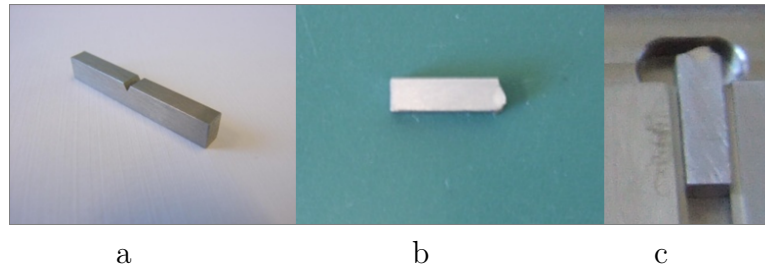
Figure 3.3: Charpy Specimen: (a) geometry of the whole Charpy specimen, (b) broken halve of Charpy specimen, (c) positioning of the specimen in the specimen holder

The non-radioactive samples are prepared in a standard laboratory, whereas a preparation in a specific metallographic Hot Cell with adapted techniques for sample preparation is needed for the radioactive specimens (see Figure 3.1).

3.1.2.2   Indentation Device

In the present study, a Zwick/Roell-Z2.5/TS01 instrumented indentation device is used to perform test at room temperature. The main characteristics of the device are summarized hereunder and displayed in Figure 3.4.

- Force range: $2 - 200\,\mathrm{N}$

- Force resolution $+$/-0.01%

- Displacement resolution $0.02\,\mathrm{\mu m}$

- Load frame compliance $208\,\mathrm{nm.N^{-1}}$

- Rockwell, Vickers and cube corner Indenter

- Motorized XY cross-table

- Coaxial Light-microscope

- CCD-camera

- Test Software: testXpert V 12.0

<div align="center">a   b</div>
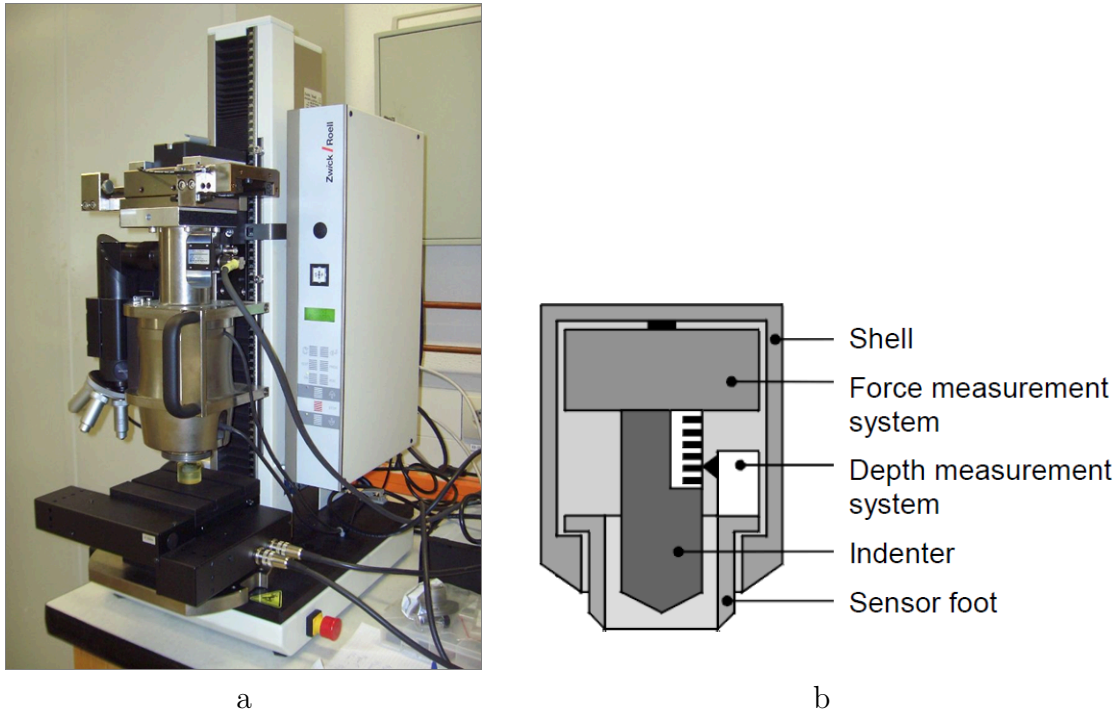
Figure 3.4: Z2.5 Zwick indentation device: (a) View of the machine, (b) hardness measurement head [25]

The specificity of the system relies on the methods for transfering the load to the tip and for measuring the displacement of the tip. The load is applied electrome- chanically by a precise spindle. A patented hardness measurement head integrates the indenter and the transducers for measurement of force and indentation depth. A pressure load cell is employed as force measurement system, while a Heidenhain linear encoder is used to monitor the indentation depth [51]. The linear encoder is composed of an optical scanning reticle reading periodic structures or graduations on a scale made of glass. The glass takes its advantage in its low coefficient of thermal expansion which ensures more stability in the measurement of the graduations. The displacement measurement is realized when the glass scale and the scanning reticle are moving relative to each other. The photoelectric scanning reticle uses the interfer- ential scanning principle based on the analysis of variations of light intensity to count the individual increments of the scale at a resolution of $0.02\,\mu m$. It also determines the current position thanks to reference markers.

The testing procedure can be divided into six main phases as sketched in Fig- ure 3.5. A working distance, denoted as LE, between the transducer foot and the surface of the sample is initially defined (step 1) in order to avoid any non-expected contact between the indenter and the sample before the test is started. The measuring head is automatically driven down until the transducer foot is put into contact with the surface of the sample, the measurement head follows its course (step 2) until the indenter contacts the sample (step 3). The distance to reach the contact is then mea- sured by the encoder between step 2 and 3. The detection of the contact is measured

by the load cell by a force increase of $42\,\mathrm{mN}$. In step 4 and 5, loading and unloading are applied at the indenter, and measurements of indentation depths are still achieved by the incremental transducer from the relative motion of the indenter related to the graduation scale position to the fix position of the scanning reticle attached to the transducer foot. When the defined loading history is finished and the force is equal to zero, the measuring head is finally driven to its initial starting test position (step 6).
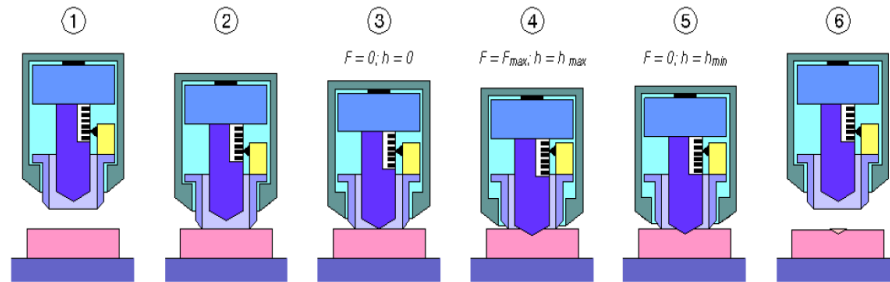
Figure 3.5: Principle of the Zwick indentation measurement head [25]

The instrument's software "testXpert" helps the operator to monitor the force and displacement signals by displaying the load-displacement P-h curve, and acquires the corresponding data. The software also provides an option for the visioning of the sample surface to allow hardness measurements from residual impressions. The positioning of the microscope is required in that case. The software acquires images from a CCD-camera related to the microscope displaying magnifications from $5\times$ up to $60\times$. The association of the microscope to a motorized cross table for X and Y positioning allows defining indentation places on the surface of the sample.

Different kinds of indenters can be employed with the Zwick device and are removable by means of a screw system. In the present work, the Vickers indenter is employed for standard hardness measurement, the Rockwell indenter is required for the indentation procedure allowing other assessment of material´s properties, whereas the Cube Corner has been selected for indentation at higher depths with a view to initiate cracks in embrittled irradiated steels.

A mounting device has been developed for indentation tests on miniaturized broken halves of Charpy specimens (see Figure 3.6). It is based on a clamping system featured by two plates. The main screw can be easily managed by the manipulators with an adapted dynamic torque, it clamps the sample onto a secondary plate which can rotate along the surface of the holder for an optimization of the contact surface with the sample. A small hole is foreseen for the broken zone of the sample in order to guaranty a full contact the sample with the surface of the holder. Sample sizes up to three times the width of the standard-tested indentation samples can be tested in this holder. The clamping force is maintained identical between the tested samples by the use of a modified dynamic torque in order to minimize effects caused by the pre-constrained state of the specimen. A study was realized to investigate the influence of the clamping force on the material's response to indentation, results are shown in Section 3.4.

a   b
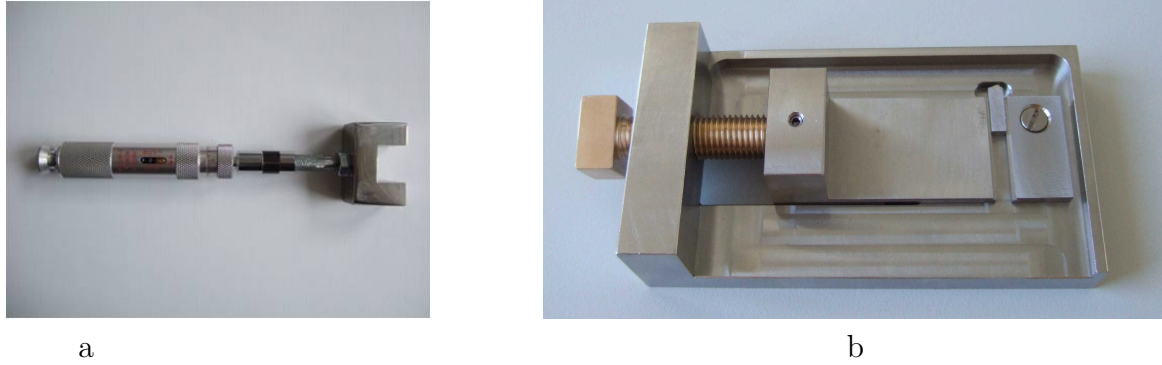
Figure 3.6: Specimen holder (b) developed, with its adapted dynamic torque (a), for in-
dentation on small-sized specimens

3.2   Experimental Procedure

The second step of the indentation procedure consists in parameterizing the test. Two
experimental indentation procedures are performed for the identification of material
properties. Both of them are force-controlled. Standard hardness tests and multi-
ple cycles-loadings tests are required for the neural networks-based analysis tool to
calculate material properties. The hardness of the material is directly derived from
the Vickers indents of $20\,\mathrm{N}$ comparable to $H_{v2.0}$, as a fast, simple and reliable way
to quantify hardening in the irradiated specimen. The multiple cyclic loading test
requires a Rockwell indenter with a spherical apex of $200\,\mathrm{\mu m}$ radius. This specific
load-controlled test has to follow a particular loading history which consists of four
loading segments, each followed by one creep segment of a duration of $100\,\mathrm{s}$ ($600\,\mathrm{s}$ for
the final creep segment at the maximum load)(see Figure 3.7). A fifth cycle can be
additionally performed to obtain information about the kinematic hardening of the
tested material.
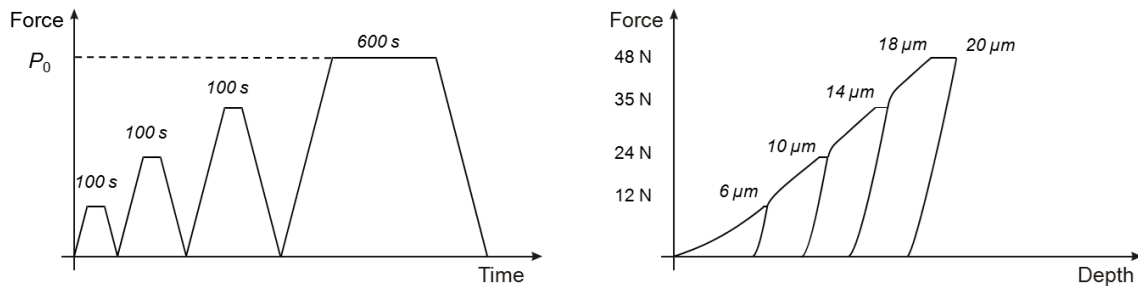
Figure 3.7: Multi-cycle indentation loading required for the neural networks based analysis
and corresponding force-depth response of Eurofer97

Since the neural networks of the post-analysis program were trained for selected
ranges of test conditions, the maximum force P_0 has to be chosen in order to achieve
an indentation depth h_0 corresponding to the depth at the end of the fourth loading
segment, between $8\,\%$ and $12\,\%$ of the nominal indenter radius R. The validity domain
for the identification of materials parameters can be summarized by Equation 3.1.

$$0.08 < \frac{h}{R} < 0.12 \tag{3.1}$$

3.3 Identification of Material Parameters

A neural network-based analysis method initially developed by Huber and Tsakmakis [52] for interpretation of spherical indentation data has been selected in view of further investigations by macroindentation on irradiated metallic materials. The analysis tool is based on a unified viscoplasticity model adapted for the characterization of the mechanical behaviors of materials planned to be tested. This approach has been successfully applied to irradiated Eurofer97 and to tungsten coatings on Eurofer97 substrate [21]. The idea is then to further investigate this ability to characterize general irradiated steels. The next sections describe the main characteristics of the selected analysis method. The interpretation of the indentation load-displacement curves by the tool is additionally presented.

3.3.1 Material Model

A constitutive model proposed by Tsakmakis [53] was selected. This model describes the elastic-viscoplastic behavior of a large range of metals and is thus adapted for the characterization of the structural steels that will be employed at the first wall of fusion reactors. The interests of using such a model in the context of the characterization of irradiated steels are multiple. At first, the hardening behavior can be detected, the material's response is also determined from complex loading histories as it will be used in the experimental indentation procedure. Finally, this model can describe a temperature-dependent material behavior only by using additional temperature dependent material properties. This last aspect of the model explains the interest in using the neural-networks based tool for the analysis of data from the indentation instrument working at high temperatures. The model is applicable for the case of large deformations but the model's constitutive equations listed hereafter are simplified for the case of small deformations.

$$\epsilon = \epsilon_e + \epsilon_i \tag{3.2}$$

$$\sigma = E \cdot \epsilon_e \tag{3.3}$$

$$\dot{\epsilon}_i = \frac{\langle F \rangle^m}{\eta} \tag{3.4}$$

$$F = |\sigma - \xi| - k (= (\eta \dot{\epsilon}_i)^{1/m}) \tag{3.5}$$

$$k = k_0 + \frac{\gamma}{\beta} \cdot (1 - e^{-\beta s}) \tag{3.6}$$

$$\dot{\xi} = \frac{3}{2} \cdot c \cdot \dot{\epsilon}_i - b \dot{s} \cdot \xi \tag{3.7}$$

$$s = \int_{\tau=0}^{\tau} |\dot{\epsilon}_i(\tau)| \cdot d\tau \tag{3.8}$$

ϵ represents the total strain, which is set by the elastic strain contribution ϵ_e and the inelastic strain ϵ_i. The stress σ is defined by Hook's law and depends on the

Young's modulus E and ϵ_e in the elastic domain, whereas it is the result of three different contributions in the plastic domain, one coming from the overstress F, another from the isotropic hardening k and a last one from the kinematic hardening ξ. In the case of a plasticity model including a pure elastic domain, an operator is necessary to be defined in order to distinguish when plastic loading occurs. The operator $\langle F \rangle$ is used for that purpose and is defined equal to F for $F > 0$ in the case of viscoplastic loading and equal to 0 in the case of elastic loading and unloading. The non-linear hardening behavior is described from the Armstrong- Frederick approach by the isotropic hardening k, and kinematic hardening ξ. In Equation 3.8, s defines the accumulated plastic strain over the time, τ, and the materials constants: k_0, γ and β stand for the yield stress, the initial slope of work hardening, and the work hardening parameter, respectively. Other material constants c and b in Equation 3.7 help defining the kinematic hardening. The strain rate $\dot{\epsilon}_i$ is directly related to the two viscosity parameters m and η that both describe strain rate, creep and relaxation effects. m is the viscosity exponent and characterizes the strain rate sensitivity, for increasing values of m the strain rate sensitivity decreases, whereas η is the viscosity parameter that, related to m, is responsible for the amount of overstress at a given strain rate.

3.3.2 Principle of Identification of Material Parameters

Generally, the aim of calculation methods based on neural-networks systems is to reproduce the functional aspects of biological neural networks. These "thinking" systems, also called artificial neural networks (ANNs), are in certain cases adaptive as in the real human neural networks system, and can thus modify their structure relative to additional received information during the learning phase also called "training" phase [54]. The present neural networks post-processing tool has a non-evolving data basis; the networks were trained for a limited predefined number of data. One fundamental aspect of characterizing those analysis methods is that the provided information comes from a non-linear data calculation process.

Tyulyukovskiy developed an ANNs tool that is able to determine viscoplastic material parameters taking isotropic and kinematic hardening into account from a specific load-displacement response including creep segments [20]. Indeed, the tool is suitable for the identification of velocity dependent strain-stress behavior of homogeneous metals from their P-h indentation response.

The development of the tool is summarized as follows. At first, the constitutive model presented in the previous section was implemented in a finite element software for numerical simulations. Numerical analyses were implemented to simulate indentation experiments with pre-defined material parameters. Variations of materials, in a selected pre-defined range, were achieved to determine the different corresponding P-h trajectories. The data from finite element analyses were used to train and validate the neural networks afterwards (see Figure 3.8). The improvement of the neural networks tool relies on the fact that the more the data have been provided to the tool, the more the tool is trained and is likely to interpret the material behavior correctly. Finally, the ANNs are generally used to solve the inverse problem (IP1), as illustrated in Figure 3.8, thus allowing the identification of materials properties from real experimental data.

The main interest of using this tool is that it can determine mechanical properties of

a specific material even when it was not previously trained with this specific material. This can be achieved from the neural networks by a kind of interpolation and even extrapolation when the material's parameters are situated outside the training range of the tool. However, the domain of interpolation remains the confidence domain, whereas extrapolation is more likely to lead to lower quality assessments.
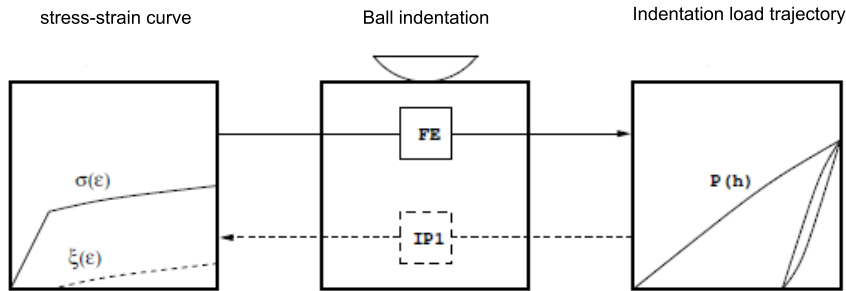
Figure 3.8: Validation of the direct (FE) and inverse problem (IP1) for ball indentation by Tyulyukovskiy [20]

3.3.3 Identification of Material Parameters

In order to identify material parameters, a specific indentation test procedure defined previously in Section 3.2 should be applied. The tool requires the experimental data of the *P-h* indentation curve extracted from the indentation instrument's monitoring software testXpert. It also requires as input data the radius R of the spherical indenter used for the indentation test and the compliance C_m of the machine's system. Therefore, the compliance of the testing system is needed to be determined by a previous calibration. The parameter's evaluation results from a processing of the original *P-h* curve which is reduced with a specified algorithm to a total number of 100 points in order to perform a faster calculation (see Figure 3.9) , 10 equidistant increments for each segments of the curve are selected, the arrows indicate the indentation depths h/R= 0.01,0.02,0.04,0.06,0.08 at which additional force values are required [20].

The identified parameters are principally E, k_0, F, γ, β, c, and b. As illustrated in Figure 3.10, each neural network is in charge of the identification of one or several specified material parameters. An initial correction of the offset of the experimental *P-h* curve is realized from the network ZeroNet. The quality of the assessment of all other material parameters depends strongly on this correction. The other networks ENet, ViskNet, SigmaNet, and XiNet are then needed to calculate respectively the Young's modulus E, viscosity parameters (m and F), the true equilibrium stresses at different true plastic strains, and optionally the kinematic hardening parameters c and b.
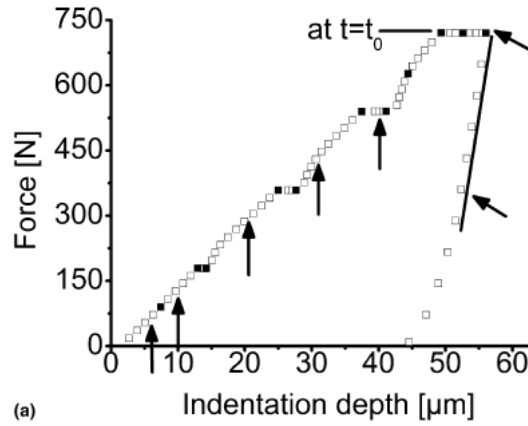
Figure 3.9: Selection of data points from the experimental *P-h* curve for the input definition of the neural networks by Klötzer et al. [23]
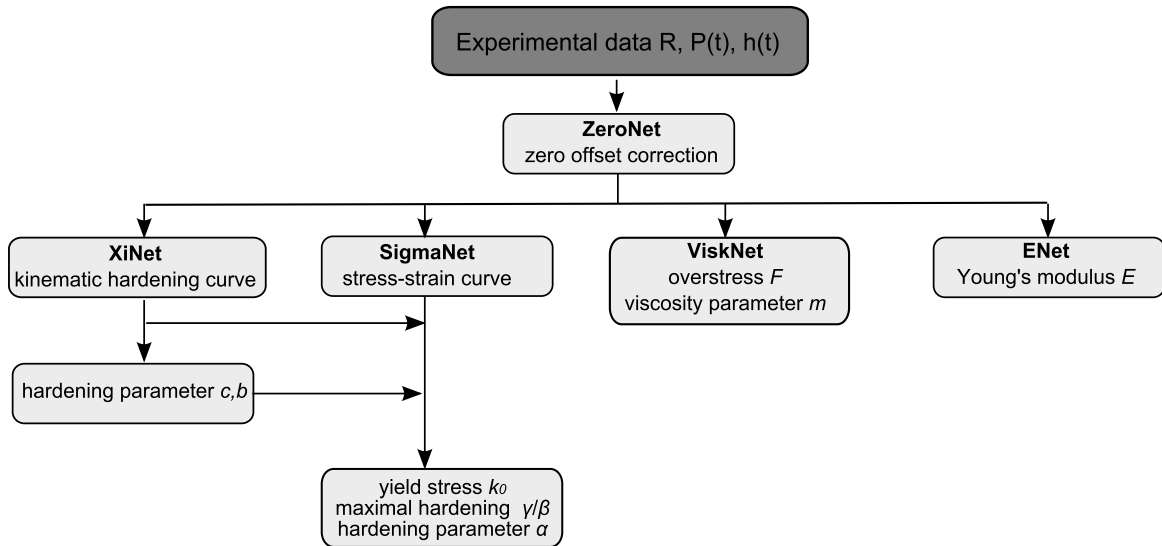
Figure 3.10: Identification of material parameters by the neural-networks tool

3.4 Influence of Testing Conditions

The aim of this section is to point out some of the testing conditions that might affect the course of the measured experimental curve and thus lead to misinterpretations concerning the mechanical behavior of materials. The main influence parameters tested in this work are summarized as follows:

- The testing parameters (applied force, loading rate)

- The mechanical state of the specimen due to the induced plasticity of neighbor indents

- The mechanical state of the specimen due to the clamping force of the holder system

All of these factors are sources of uncertainty in the measurement and should be further studied in order to ensure the accuracy of the measurement.

3.4.1 Influence of Test Parameters

In a load-controlled indentation test, the most relevant test parameters are the peak indentation load and the loading speed considering that the unloading speed should be taken as equal to the loading speed. Before interpreting results from samples tested at a specific maximum applied load and loading speed, it is of interest to analyze the load-displacement behavior of a same material in response to different loading parameters. Since Eurofer97 is considered as the reference material in this work, Vickers indentations were performed on Eurofer97 in as-received specimens. A load range from 40 N to 70 N was selected for this study, whereas loading rates from $0.133\,\mathrm{N\cdot s^{-1}}$ to $26.6\,\mathrm{N\cdot s^{-1}}$ were tested.

3.4.1.1 Applied load

The influence of the force on the measured hardness is shown in Figure 3.11. A discrepancy between the measured hardness values was found to be of less than 3%. Considering that the size of the residual impression is measured optically by the operator, the discrepancy can additionally be explained by a human error factor. It can be concluded from these experiments that the indentation load has not a significant influence on the measured hardness values in the tested load range.
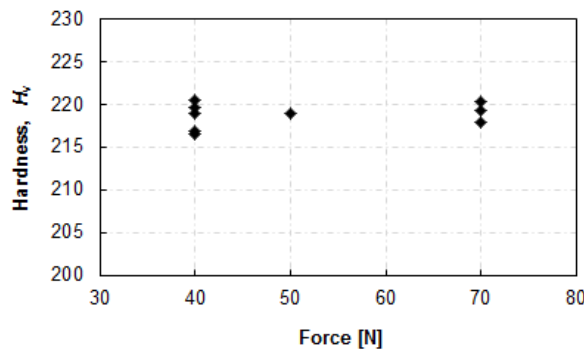
Figure 3.11: Effect of the maximum applied force on the measured hardness (Eurofer97)

3.4.1.2 Applied loading rate

The section examines the influence of the loading rate on the assessment of the hardness. Vickers Indentation were performed at different loading rates from $0.133\,\mathrm{N/s}$ to $26.6\,\mathrm{N/s}$ on Eurofer97. Figure 3.12 indicates that the mean value of the hardness which is found for slow speed is almost identical to the hardness values found at higher loading rates. This observation leads to the conclusion that for the selcted range of loading rates and according to the low deviation observed, there is no significant impact of the loading rate for the hardness measurement. According to the fact that the indentation tests performed in this study are load-controlled and defined by a constant load rate of $0.5\,\mathrm{N}$, the influence of the load rate on the changes of the indentation response for a similar material is not thought to be significant.
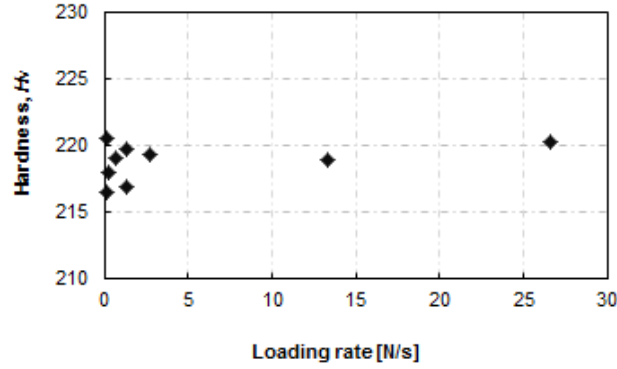
Figure 3.12: Effect of the loading rate on the ratio of maximum indentation depth to maximum force (Eurofer97)

3.4.2   Mechanical State of the Specimen

The specimen mount plays a role on the measured load-displacement curve. In the initial holder configuration, the specimen was simply settled on a free surface. Combined sliding and tilting effects occurring at the beginning of the sample loading could be detected (see Figure 3.13) and were leading to a shift in load response.
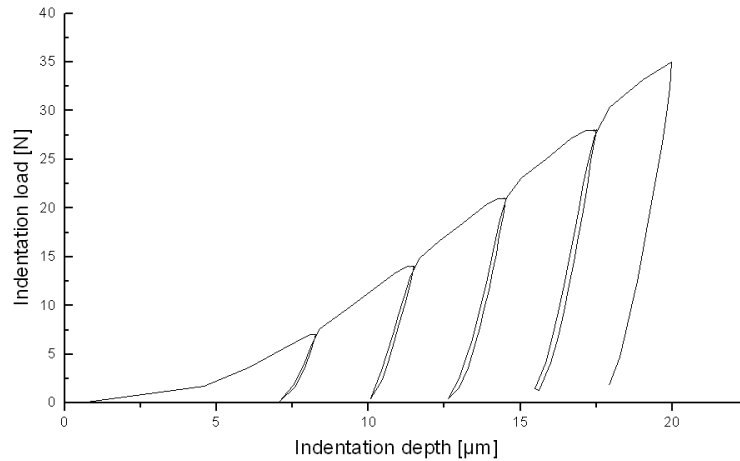
Figure 3.13: Sliding effect observed in indentation curves as kinks in the *P-h* curves at low loads

A reliable way to attach the sample is needed to prevent the sample from moving during the indentation test. The specimen holder in Figure 3.6 based on a clamping system was developed for that purpose. The phenomenon observed in Figure 3.13 did no longer occur with this holder. However, an increasing deviation of the depth with increasing loading was observed along the course of indentation performed on an identical specimen (see Figure 3.14). Variations of the compliance in the range of 0.015 to 0.035 μm.N^{-1} could be evaluated at the sample from the neural-networks tool assuming that the material has a constant Young's modulus of approximately 200 to 210 GPa in the case of Eurofer97.

It has to be mentioned that the average grain size in Eurofer97 Anl remains within the range of 9-16 μm [55; 56] while residual impression resulting from indentation at 20 μm with a diamond ball radius of 200 μm have an average diameter of 175 μm. It
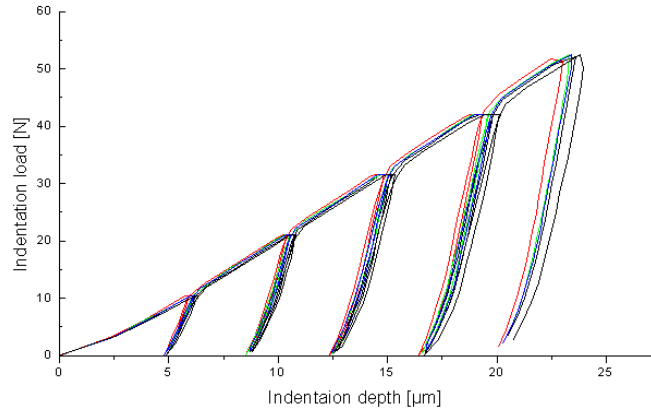
Figure 3.14: Discrepancy observed between indentation curves

is then considered that inhomogeneities in the microstructure should play a minimal role in the course of indentation.

Compressive or tensile states present in the material are known to induce changes in the load-displacement indentation curve as it is shown by Jang in Figure 3.15 [57]. It is of interest to study by finite element simulations if the discrepancies observed in the experimental curves might result from a modification of the stress-state present in the specimen. Besides existing machine effects, two possible causes for such changes are: the plasticity induced by a neighboring indent and the influence of the clamping force of the specimen holder.

a   b
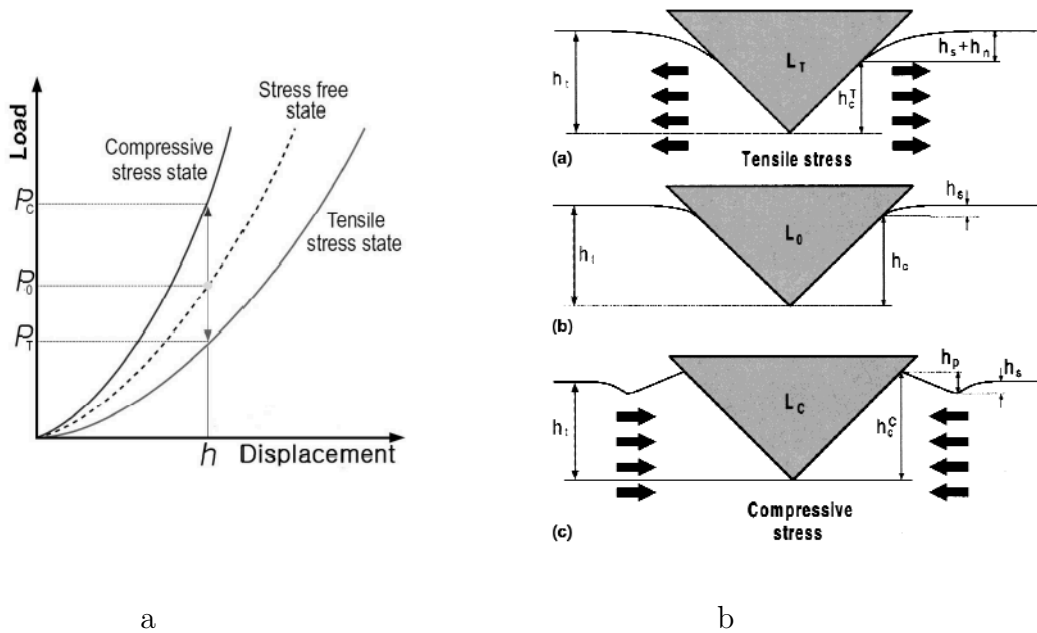
Figure 3.15: (a) Compressive-tensile loading-depth behavior (b) compressive-tensile stress state in the material by Jang [57]

3.4.2.1   Influence of Indentation Position

It has been previously mentioned that an indentation space of 1 mm is needed for the
defined testing conditions. Considering the discrepancies observed between different
experimental curves for same testing conditions, the amount of plasticity induced at
1 mm from the center of an indentation on a Eurofer97-like material is numerically
investigated. A 2D symmetrical model consisting of a spherical indenter and a flat
specimen is built in the finite element software ANSYS for this study (see Appendix B)
[58]. Properties of elasticity and plasticity strains based on experimental data coming
from tensile tests and defined by a multilinear isotropic hardening are implemented
for the material model of Eurofer97. A penetration of 20 µm of the ball indenter with
a radius of 200 µm is first applied to reach the approximate indentation depth of
real experiments; the indenter is then unloaded and put in its original non-contact
position.

A simulation of the elastic behavior at the specimen during indentation is carried
out in a first step. The analysis of maximum shear stress confirmed the stress field
predicted from the Hertzian theory for spherical-flat surface contact [34]. The maxi-
mum shear stress occurs at approximately 33 µm under the surface of the sample for
a half contact area of ca. 84 µm (see Figure 3.16).
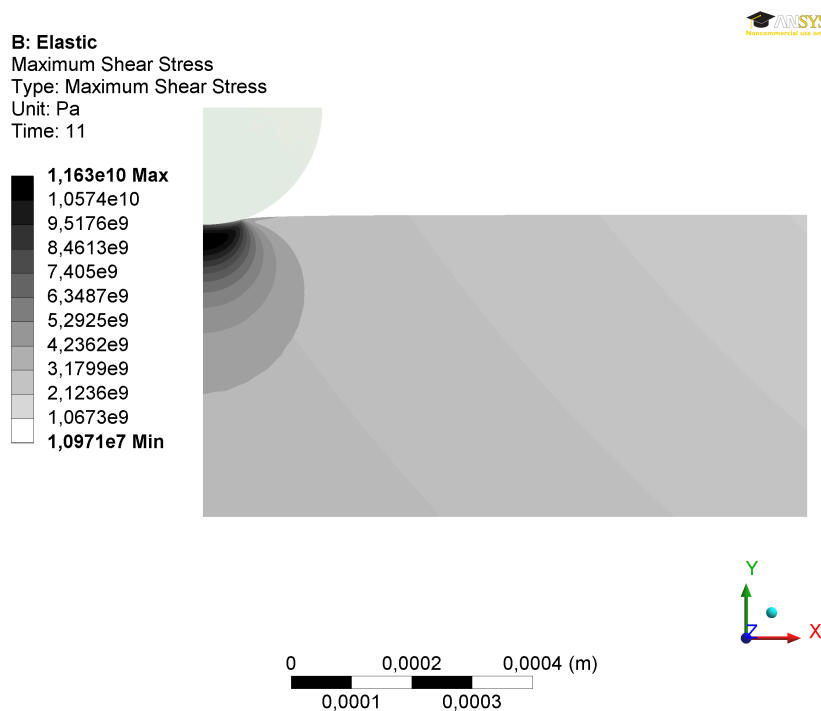
Figure 3.16: Shear stress distribution at maximum indentation depth of 20 µm with a
spherical indenter with a radius of 200 µm (elastic contact)

Additional simulations are carried out to further study the effect of induced plas-
ticity in the material during loading and after unloading. Figure 3.17 and Figure 3.18
display these two states. At peak load, plasticity occurs until a depth of 220 µm under-
neath the surface of the sample and at a distance of more than 150 µm from the center
of the ball indenter at the surface of the sample. After unloading, a residual impres-
sion of 180 µm was predicted from the simulation and was found to be consistent with
real measured indent sizes of ca. 175 µm. The Von-Mises stress analysis indicates that

from a distance of 0.5 mm of the center of indentation, the stresses become lower than 10 MPa. Such residual stresses represent less than 2% of the Eurofer's yield strength. Therefore, it can be concluded that a distance of 1 mm between indents is sufficient. The effect of a compression load induced by the clamping jaws on the specimen is investigated in the next study for a magnitude of 10 MPa.
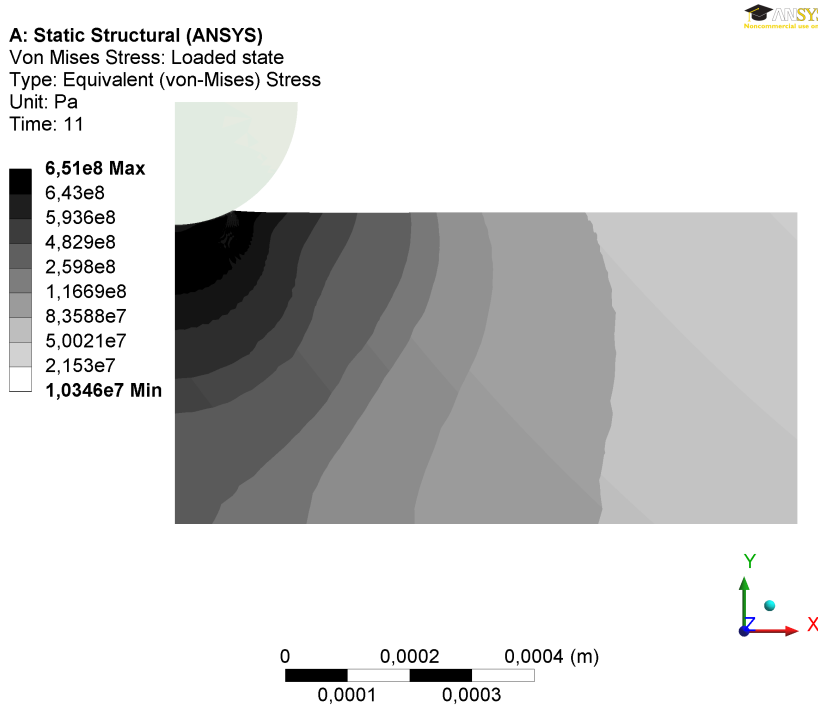
Figure 3.17: Fully plastic loading at maximum indentation depth - von Mises stress distribution

3.4.2.2   Influence of the clamping force of the holder system

A second study is realized to investigate the change in the indentation force reaction according to different stress states in the specimen resulting from the clamping. Normal stresses are applied at the two surfaces of the specimen making the contact with the clamping jaws. An indentation of 20 µm is applied for applied stress conditions. A decrease of about 0.1 N of the indentation reaction force was found to occur for an applied normal stress state of 10 MPa in comparison with a free stress state of the sample. Hence, the similar modification of the stress state issued from indents simulated every 1 mm in a Eurofer97-like material is then expected to be low regarding the changes observed in the course of the *P-h* curves. Finally, the residual stress induced in the specimen from indentation is assumed to have a minor role on the discrepancies in experimental curves. Indentations with a distance of 1 mm are considered to be adapted for the present work.

A model of the whole specimen holder is presented in 3 dimensions in Figure 3.19. A clamping force of 280 N is applied on both sides of the specimens to simulate the force applied from the dynamic torque of the holder in real experiments. The clamping force induces stresses in the range of 2 to 10 MPa in the specimen (see Figure 3.19). Considering the previous study, the clamping force applied to the sample was considered to be too small to induce visible changes in the *P-h* curve.

A: Static Structural (ANSYS)
Von Mises Stress: Unloaded state
Type: Equivalent (von-Mises) Stress
Unit: Pa
Time: 29

6,5097e8 Max
5,715e8
4,9203e8
4,1257e8
3,331e8
2,5363e8
1,7417e8
9,4701e7
1,5235e7
1,8714e6 Min

0   0,0002   0,0004 (m)
    0,0001   0,0003
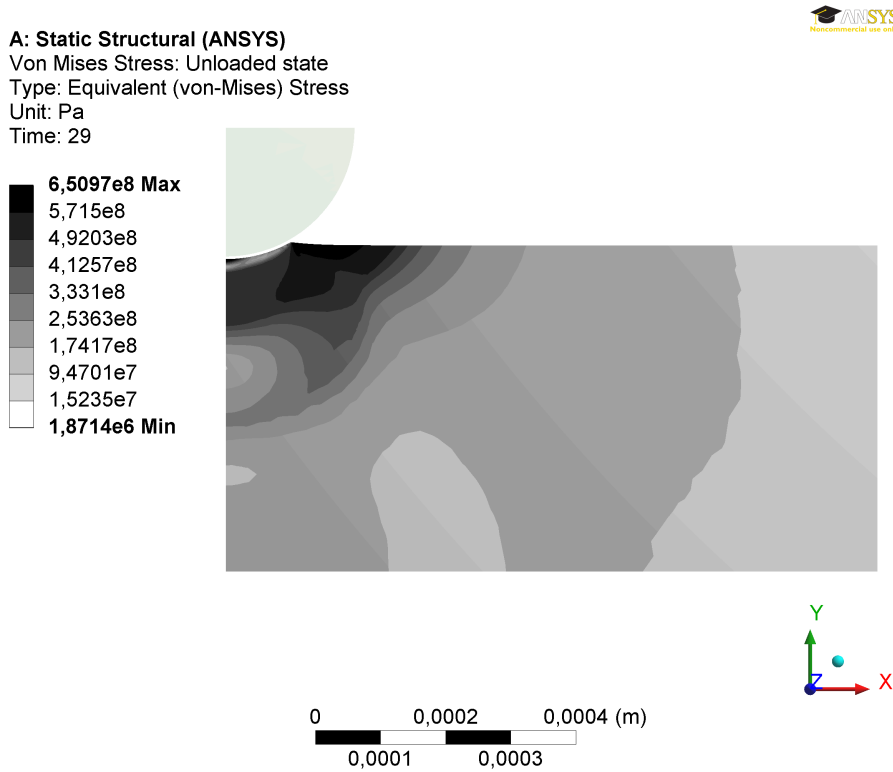
Figure 3.18: Von Mises stress state in the specimen from Figure 3.17 after unloading

An analysis of the compliance at 1 mm indentation distance showed a regular evolution from 0.015 to 0.035 µm/N. Simulating the holder's deflection, it was found that the changes in the calculated compliance could be explained by an elevation of the sample by an order of magnitude of 1 to 8 µm during the clamping process as illustrated in Figure 3.20.

a   b
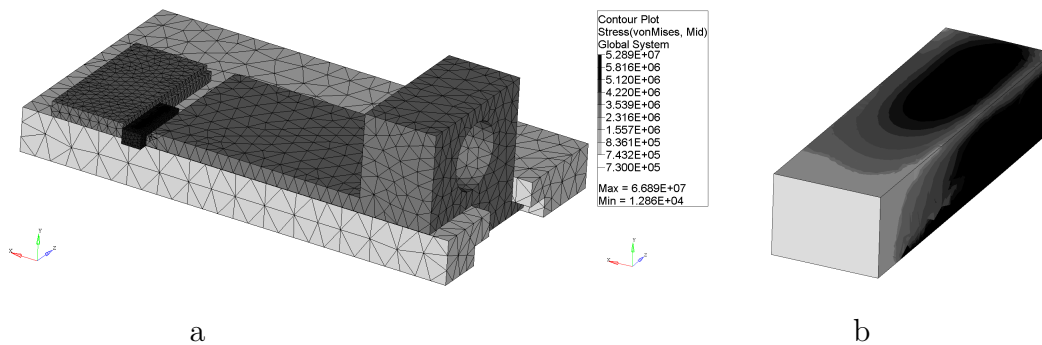
Figure 3.19: (a) Model of the sample holder (b) Von-Mises stress state of the specimen induced by a clamping force of 280 N
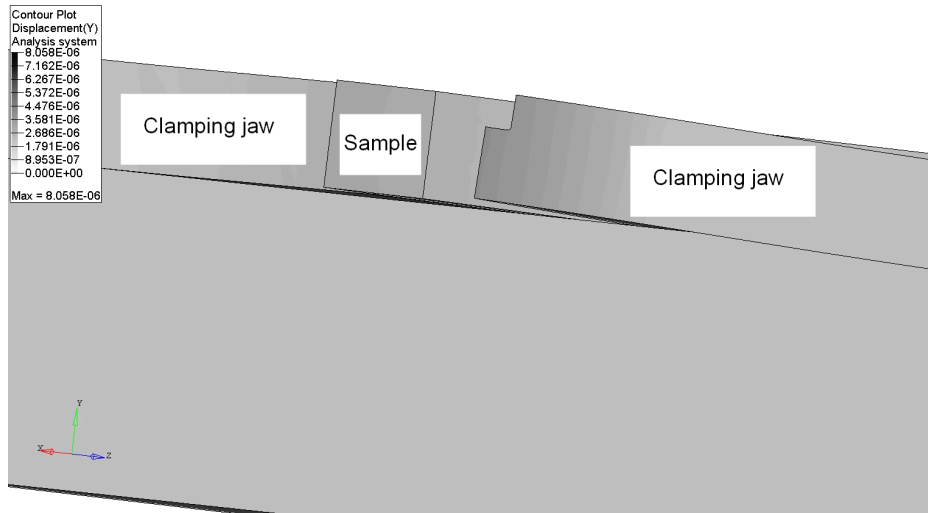
Figure 3.20: Simulation of the position state of the sample during clamping (scale factor:100)

Discussion

The shape of the Rockwell indenter used was additionally verified from the analysis of residual impressions of old indents for which the indenter was supposed to be non-damaged. The impressions were compared to more recent ones. Scanning electron microscope (SEM) micrographs did not reveal any significant difference in the shape of the residual indents.

It is demonstrated by these last analyses that the indentation interval and the stress induced in the specimen by the applied clamping system are thought to play a minor role in the deviations observed in the experimental indentation curves on single tested samples. The position of the sample in its holder should be more decisive for the reproducibility of the experimental curves. Discrepancies have been measured regarding the material parameters identified from experimental indentation curves (see results in Chapter 4), however, the role of the effect observed in Figure 3.14 on the assessment of the mechanical properties is not directly quantifiable notably due to the accuracy of the method used for the post-processing. The impact of the changes in indentation depth in the P-h curve could not have been directly correlated with a systematic change in the assessment of the mechanical properties.

Chapter 4

Indentation on Irradiated Materials

4.1 Irradiation-induced Effects

The irradiation-induced hardening and embrittlement effects are of particular interest in this chapter. Such phenomena were understood from transmission electron microscope analyses [59]. The neutron irradiation damage generates Frenkel pairs in the material's lattice that produce in turn dislocations loops. Such loops are likely to coalesce with the existing dislocations networks. As a result, the dislocation density present in the matter increases, what finally leads to a global hardening and embrittlement of the material. The material's mechanical state resulting from neutron radiation in fission reactors and future fusion reactors highly depends on the irradiation conditions. Both the damage rate induced by neutron irradiation and the irradiation temperature T_{irr} should be considered. The former damage factor is illustrated in Figure 4.1 and shows the influence of the irradiation dose on the changes in the yield strength, $R_{p0.2}$, of Eurofer97 at two irradiation temperatures of 300 °C and 330 °C for which irradiation effects are most pronounced [13]. A saturation in the strength is reached at ca. 15 dpa, which demonstrates that most radiation effects are expected to occur at such a dose for Eurofer97. The latter damage factor, the irradiation temperature, is also responsible for hardening related to a decrease of fracture toughness at low irradiation temperature $T_{irr} < 0.3\ T_m$, whereas irradiation-creep becomes more pronounced at $0.3\ T_m < T_{irr} < 0.5\ T_m$, where T_m is the melting temperature [60]. Figure 4.1 demonstrates that most significant changes in Eurofer97's ductile to brittle transition temperature (DBTT) and upper shelf energy (USE) occur between 250 °C and 350 °C irradiation temperature [12].

A correlation exists between the loss in ductility and the increase in hardness of steels [61]. These two effect could be observed from tensile stress-strain curves when comparing unirradiated and irradiated tested specimens (see Figure 4.2) [62]. A hardening and embrittlement increase is obvious at T_{irr} =250 °C and 300 °C/ 15 dpa.

The purpose of the present study is to analyze the hardening and strengthening behavior of irradiated RAFM steels by indentation. Therefore, this chapter will mainly focus on hardness measurement and yield strength evaluation performed by the post-analysis method for a variety of irradiation temperatures from 250 to 450 °C at a constant irradiation dose of 15 dpa. In this study, the European reference steel Eurofer97 and the Japanese F82H-mod steel are investigated. A distinction is made for Eurofer97 regarding its pre-irradiation heat treatments. Eurofer97 Anl corresponds to the material in as-delivered state, whereas Eurofer97 WB has been additionally
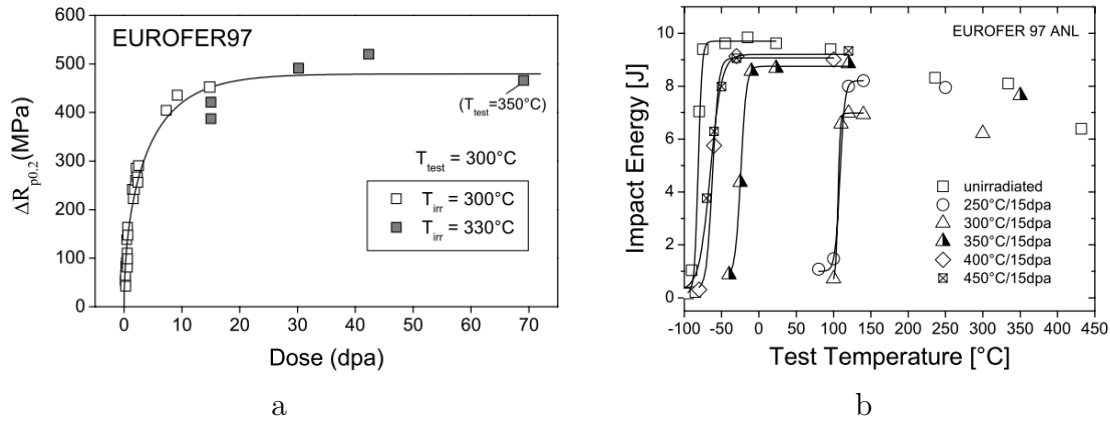
Figure 4.1: Changes of properties in Eurofer97: (a)Evolution of Eurofer97's strength at different irradiation doses [13], (b) Evolution of Charpy impact properties of Eurofer97 at different irradiation temperatures [12]
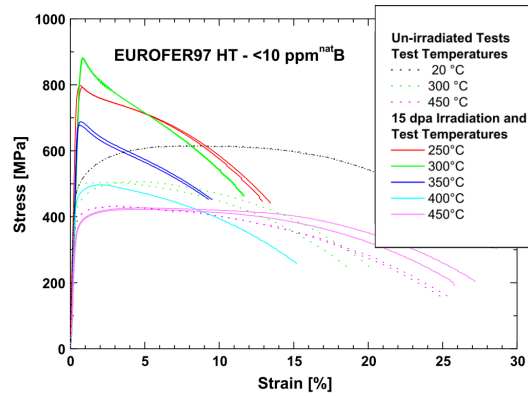
Figure 4.2: Evolution of Eurofer97's tensile behavior at different irradiation temperatures [62]

austenitized at higher temperature and tempered. Materials properties including pre-irradiation heat treatments, chemical composition and irradiation conditions are all listed in Table 4.1, Table 4.2 and Table 4.3 [55]. A more detailed material chemical composition is provided in Appendix B. Except for the unirradiated specimens, one specimen of each irradiation condition was provided for each materials irradiated states.

Table 4.1: Various properties of tested RAFM steels

	Heat	Grain size	Heat treatment
Eurofer97 Anl	83697	16.0 μm	980 °C/0.5 h + 760 °C/1.5 h
Eurofer97 WB	83697	21.4 μm	1040 °C/0.5 h + 760 °C/1.5 h
F82H-mod	9741	55 μm	950 °C/0.5 h + 760 °C/2 h

Table 4.2: Main chemical composition in wt.% of tested RAFM steels

	Cr	W	Mn	C	B	Fe
Eurofer97 Anl Eurofer97 WB	8.91	1.08	0.48	0.12	0.001	balance
F82H-mod	7.7	2.04	0.16	0.09	0.0004	balance

Table 4.3: Irradiation temperatures in °C (dose=15dpa)

Eurofer97 Anl	250	300	350	400	450
Eurofer97 WB	250	-	350	-	450
F82H-mod	-	300	-	400	-

4.2   Hardness Measurement

The evolution of the Vickers hardness of the tested materials according to the irradiation conditions is shown in Figure 4.3. Regarding the unirradiated state of Eurofer97, the hardness is in good agreement with values obtained earlier [63], though these hardness experiments were performed at 30 N. A clear hardening of all tested materials occurs at irradiation temperatures of 250 to 350 °C. For irradiation at higher temperatures, damage seems to be accompanied by a partial recovery. It can be observed that the difference in hardness, induced by the different pre-irradiation heat treatments of Eurofer97, clearly is conserved throughout the irradiation. According to the fact that each sample, which corresponds to one specific irradiation condition, has to be further tested by ball indentation, a maximum number of 3 indentations was applied for the hardness measurement. The scattering of the measured hardness values was found to be lower than 2 % in all tested conditions (see Section A.3).
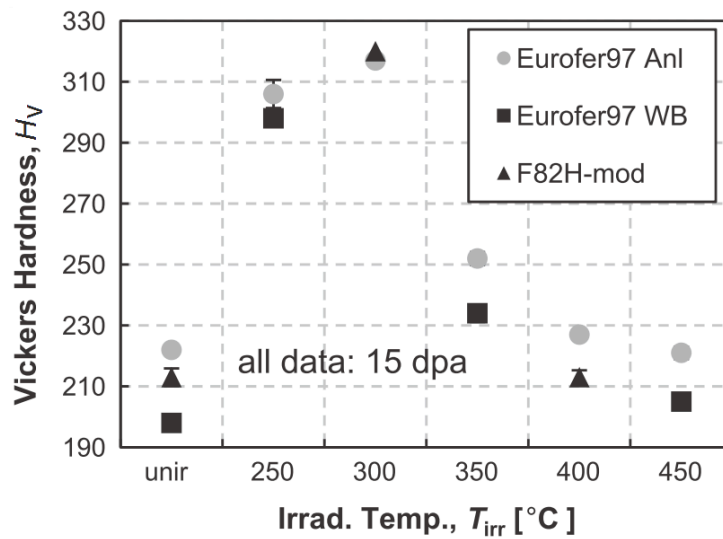
Figure 4.3: Evolution of the hardness for different states of irradiation temperatures [64]

4.3   Strength Assessment

Additional indentation tests based on multi-cycles loading histories have been performed onto the previously tested specimens in order to assess the material strength properties from the post-analysis tool [21]. Ball indentation tests performed on Eurofer97 Anl are displayed in Figure 4.4. A significant hardening of irradiated samples is visible from the multi-cycle indentations up to T_{irr}=300 °C while a declining effect hardening effect is visible from T_{irr}=250 °C up to T_{irr}=450 °C. The irradiation damage at T_{irr}=450 °C is considered to be negligible for the two studied steels if compared to their original mechanical state. Indeed, the applied cyclic load required for the post-processing tool to fulfill the criterion Equation 3.1 evolves from to 10.5 N at the unirradiated state to 18 N at the irradiated state for T_{irr}=300 °C while it decreases to 10 N at T_{irr}=450 °C.
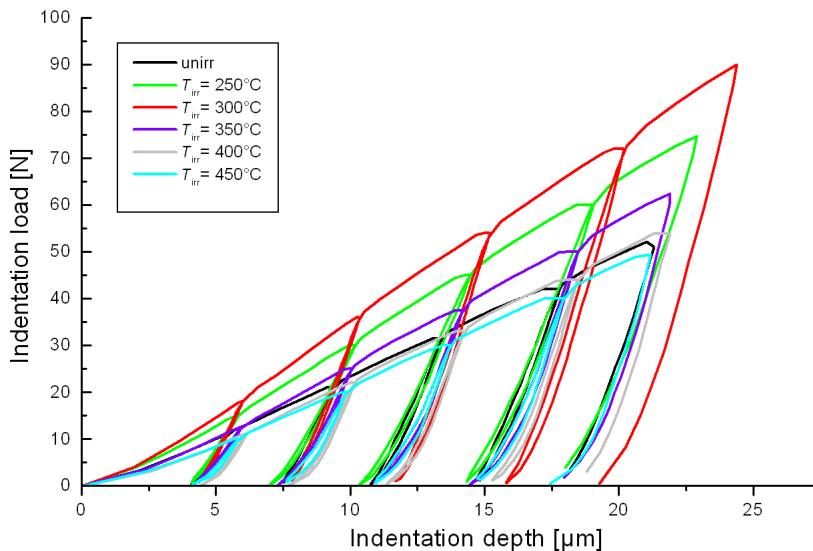
Figure 4.4: Cyclic ball indentation on Eurofer97 Anl for different irradiation temperatures

The yield strength, $R_{p0.2}$, was identified by the neural networks based analysis method from the multi-cycle ball indentations. In Figure 4.5, the full symbols represent the identified values of $R_{p0.2}$ (see Section A.3). For comparison, open symbols, representing instrumented tensile tests are added. The tensile experiments were previously performed at the FML on SPICE tensile specimens with a diameter of 3 mm [62]. These specimens were irradiated in the same conditions as the present tested specimens, but were tested at irradiation temperature and not at room temperature as in the case of indentation, what explains systematic differences for the higher irradiation temperatures. Further explanations about the discrepancies observed are given in section 4.5. The hardening tendency predicted by the post-analysis tool globally was found to be in agreement with the tendency found by the Vickers study. It confirms a significant strengthening effect in the region of 250-300 °C as well as a temperature-induced recovery effect at 350 °C and above, even though the 300 °C-irradiated F82H-mod shows - compared to Eurofer97 - less increase in the identified $R_{p0.2}$ than it might be expected by the increase in the measured hardness. Contrary to

the other tested samples, a higher scattering in the *P-h* curves leading to a scattering of approximately 60 MPa for the calculated yield strength was found for this sample state and could explain the different behavior found in the yield strength. One main reason that might explain the difference in sensitivity between $R_{p0.2}$ and H_v in the irradiated steels is described in more detail in Section 4.4.
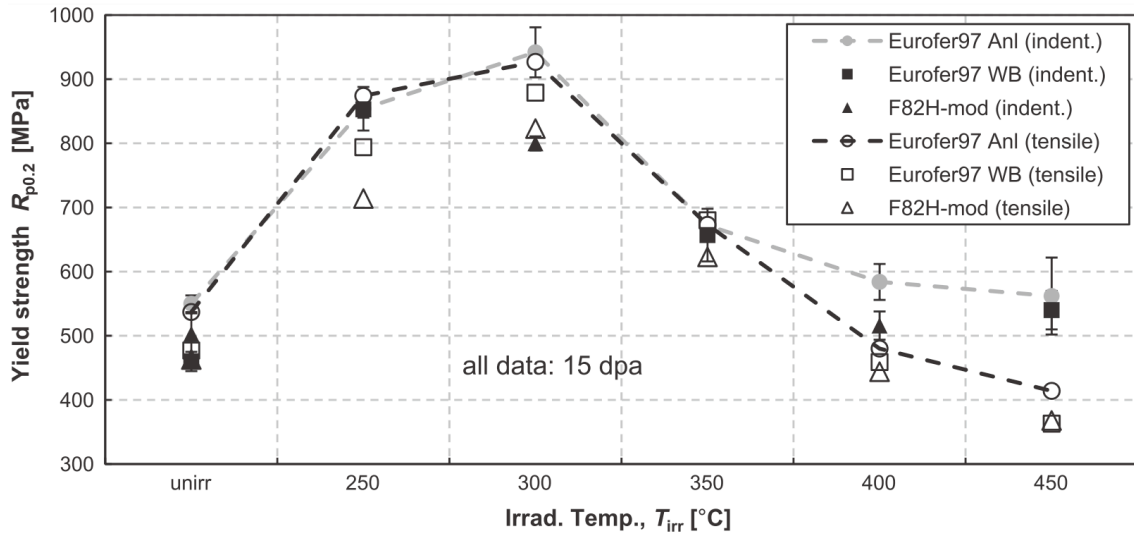
Figure 4.5: Comparison of indentation and tensile yield strength, $R_{p0.2}$, of RAFM steels at different temperatures [64]

It was initially shown by Schneider et al. [65] that, in the case of martensitic materials and especially for F82H-mod irradiated at 2.4 dpa, the DBTT values increase nearly linearly with the dynamic yield strength measured from Charpy impact tests from the lower irradiation temperature of 450 °C gradually to 250 °C. A similar tendency was observed later by Gaganidze for the DBTT and USE values of the SPICE specimens. Here, the most affected samples were irradiated at 300 °C. The strengthening and hardening effects revealed from the indentation experiments follow the same trend, which attests that the embrittlement properties are closely correlated with the material strength.

Furthermore, the effects of the pre-irradiation heat treatments of Eurofer97 are also visible from the strength behavior displayed in Figure 4.5. It can be concluded that Eurofer97 WB exhibits globally a slightly softer behavior than Eurofer97 Anl, even though it remains sligthly more affected by the neutron-irradiation than Eurofer97 Anl. The higher austenitization temperature of Eurofer97 WB that leads to a coarsening of the grain structure (Table 4.1) is supposed to be the cause of the global decrease of the strength in accordance to the Hall-Petch relationship. Additionally, it should be kept in mind that the as-delivered state was heat-treated at industrial conditions, whereas the Eurofer97 WB was treated in more precise laboratory conditions. A lab-scale heat-treatment of 980 / 760 °C showed a softer behavior than Eurofer97 Anl, giving a hint on the heat treatments' different quality [66].

4.4 Correlation between Hardness and Strength

The relationship existing between the hardness and the yield strength was first investigated by Tabor [33] showing that the hardness H is directly proportional to the

flow stress in compression and can be expressed by:

$$H = C \cdot Y \qquad (4.1)$$

In Equation 4.1, C is the constraint factor and depends upon the tested specimen and the indenter geometry and Y is the flow stress in sample compression [34]. Tabor predicted a value of 3 for various metals whereas Francis [67] and Johnson [68] predicted a value close to 2.8. Using this approach with the yield stress (at 0.2 % offset), the constraint factor C was evaluated in the different irradiated states. The corresponding relationship is displayed on Figure 4.6a. For both tested materials a constraint factor was found to vary from 2.3 at the unirradiated state to almost 3 for T_{irr}=300 °C at which most significant damages occur due to irradiation. Despite this variation, the relationship is globally found to be in agreement with the theory, which also attests that the characterization issued from the post-processing of experimental data remains consistent for the tested materials.
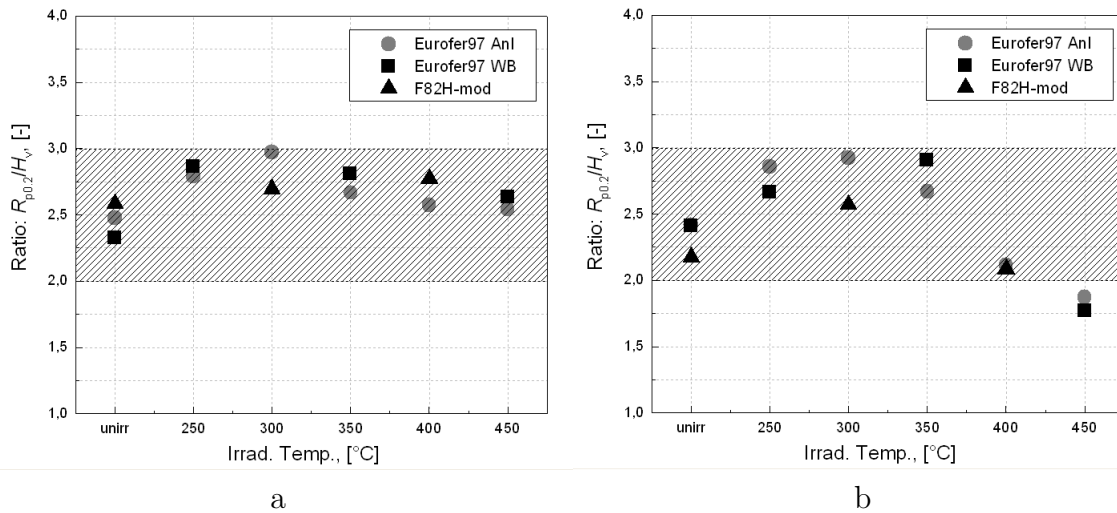
Figure 4.6: Relationship between yield strength from indentation tests and hardness (a), and yield strength from tensile tests and hardness (b) in RAFM steels

A more detailed analysis of the data shows that the hardness is slightly less sensitive to irradiation hardening effects than the yield strength in the region of T_{irr}=250 °C to 350 °C. In accordance with the approach proposed by Busby et al. [69] for austenitic and ferritic steels in the case of the irradiation dose's influence and as it could be identified from tensile experimental curves of irradiated specimens [62], the irradiation temperature is also found to be responsible for a decrease of the strain hardening exponent n in the region where the hardening effect is the highest. Consequently, as the hardness, in contrast to the yield strength, is measured at plastic strains where strain hardening effects have to be considered, changes in hardness ΔH_v in the range of 250-350 °C are expected to be smaller than the corresponding changes in yield strength $\Delta R_{p0.2}$. This can finally explain a lower sensitivity of hardness to the irradiation-induced hardening effect between 250 and 350 °C in comparison with the identified yield strength sensitivity.

Doing the same analysis with the yield strengths obtained from tensile tests, it comes out that the ratio of $R_{p0.2}$ to H_v globally remains in the range of [2,3] except for

T_{irr}=450 °C whose ratio is smaller than 2 (see Figure 4.6b). In this last irradiation condition, as it is the case for T_{irr}=400 °C, the effect of the test temperature of the tensile tests, which is mainly responsible for a lowering of the yield strength, clearly is exhibited by the drop of the ratio.

4.5   Comparison to Tensile Tests

The tensile behavior of the irradiated specimens is of interest in this section. A comparison is made between the stress-strain curves calculated by the post-analysis tool after indentation and those obtained from tensile tests. Figure 4.7 gives an illustration of these comparisons. It should be mentioned that softening effects combined to necking and breaking phenomena are not integrated into the neural-networks-based analysis method. Therefore, and as expected, higher differences in the tensile behavior of the most brittle states can be detected from the ultimate tensile strength. An other reason for the discrepancies observed is the effect of the test temperature in the tensile test which becomes significant from 400 °C.

Despite the discrepancy observed, the neural-networks-based analysis method remains suitable to predict changes in the strength of irradiated samples. The most ductile state of all tested specimens is here corresponding to the unirradiated state. The stress-strain behavior identified from the post-processing tool exhibits a mechanical behavior of RAFM steels which remains close to the one measured by tensile test.
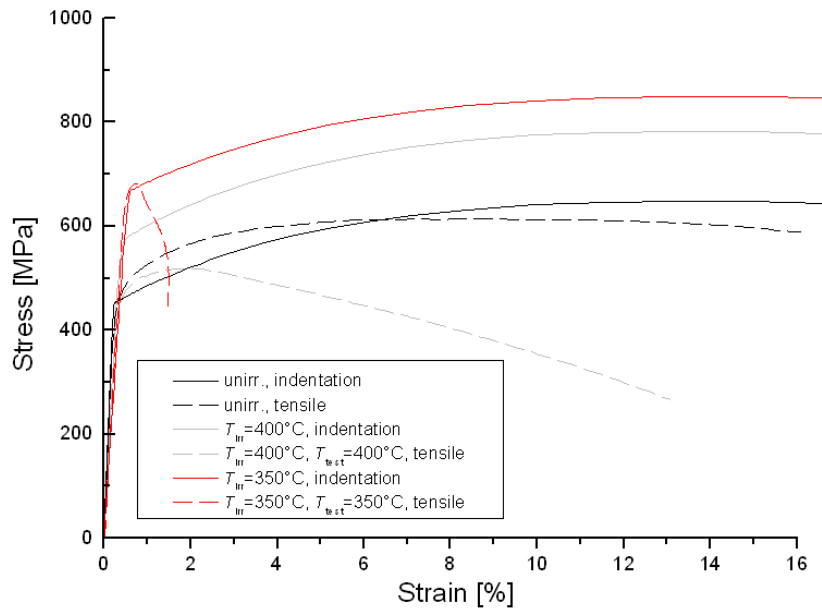
Figure 4.7: Comparison of tensile and indentation stress-strain curves at the unirradiated and two irradiated states of Eurofer97 (for a constant dose of 15 dpa)

The yield strength values obtained from indentation tests are compared to results from tensile experiments (see Figure 4.5). The temperatures of the tensile experiments had been chosen to be identical to the irradiation temperature of the tested specimen, whereas the indentation tests were performed at room temperature. For this reason, the following comparison has to be interpreted rather carefully. Based on the results obtained, assumptions are proposed.

Deviations between yield strengths found by indentation and by tensile test are particularly low up to 350 °C, whereas higher discrepancies are visible from T_{irr}=400 °C. Considering the testing temperature of the performed tensile tests, it is generally expected for all irradiation tested conditions to obtain lower material strengths in tensile tests than in indentation tests realized at room temperature. Based upon this statement, the neural networks analysis tool tends to underestimate the expected strength behaviors of indented materials irradiated in the range of 250-350 °C of approximately 15 %, while both types of results are in good agreement for 400 °C and 450 °C. This tendency is confirmed from a second analysis (see Figure 4.8). In this further analysis, the strength behavior which was identified by indentations is extrapolated by means of data coming from tensile tests performed at different test temperatures. The original data are modified by means of a second degree polynomial which was calculated from the evolution of the material's strength in relationship with the test temperature (see Appendix A). The data used for the assessment of the polynomial come from measurements on tensile samples made of Eurofer97 in its unirradiated state and tested from 20 to 500 °C. This analysis should be seen as an additional means to compare the results of indentation to tensile tests and is not considered to be a systematic method for the prediction of the mechanical behavior at high temperature of specimens indented at room temperature.
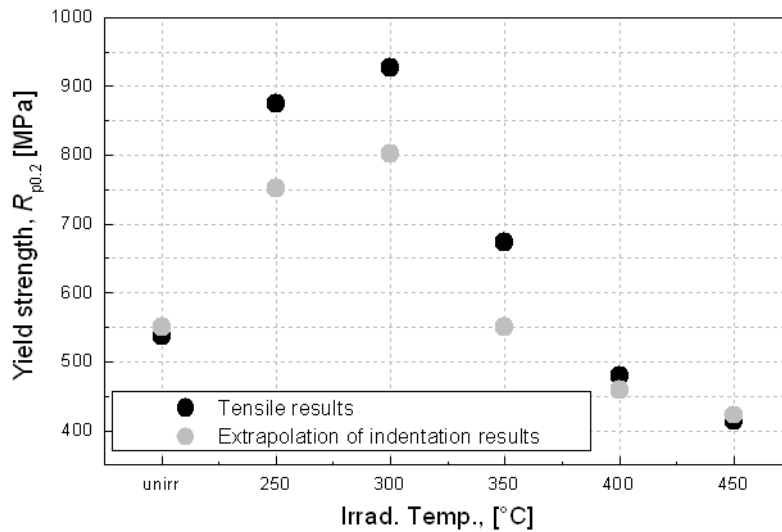
Figure 4.8: Comparison of yield strength from indentation (data extrapolated for high temperatures) and yield strength from tensile test, $R_{p0.2}$, in Eurofer97 Anl irradiated at different temperatures

Additionally, concurrent phenomena can justify the trend observed for the indentations achieved at room temperature. Irradiation-induced hardening is - for the shift in $R_{p0.2}$ - the dominating effect below an irradiation temperature of 350 °C. This explains a more similar behavior between the data coming from tensile tests and the one coming from indentation tests performed at room temperature as shown in Figure 4.5. Moreover, a recovery effect of irradiation-induced hardening occurs from 350 °C to 450 °C and reduces the effects of radiation damage. Hence, the effect of irradiation is subordinate and the absolute influence of the test temperature is much higher in the range of 350 to 450 °C - and, thus, induces a general reduction of the strength during

the tensile tests. This effect cannot be detected in the indentation tests performed at room temperature. Nevertheless, the new instrumented indentation device that is developed in this work will help examine such effects by testing samples up to 650 °C.

4.6 Conclusion

Material properties, such as $R_{p0.2}$ derived from indentation, confirm the strengthening expected by the hardness results in the region of 250 – 350 °C. Hence, the indentation method can be used to identify irradiation-induced hardening in the RAFM steels investigated. Analysis of the pre-irradiation heat treatment of Eurofer97 leads to the conclusion that Eurofer97 WB globally exhibits a slightly softer behavior than Eurofer97 Anl. Even if Eurofer97 WB seems a little more affected by the irradiation, H_v and $R_{p0.2}$ remain below the corresponding values of the as-delivered state Eurofer97 Anl. The relationship found between the measured material´s hardness and calculated yield strength in the different irradiation states is in accordance with the theory of Tabor and Johnson. A similar hardening and strengthening tendency is evident from the indentation and tensile results. Higher discrepancies are visible at higher irradiation temperatures, where the influence of the tensile test temperature is supposed to be more relevant than at lower irradiation temperatures. Indentation tests performed at high temperatures with a new instrument using the neural networks analysis method become meaningful in that context and will thus help provide a more complete analysis of the hardening behavior characterizing irradiated RAFM steels at high temperatures.

Chapter 5

Further Indentation Opportunities on Irradiated Materials

In this chapter, further testing opportunities are provided from the IIT and gives additional information about the irradiation damage resistance of RAFM steels. Indeed, it will be demonstrated in a first part concerning the post-irradiation annealing of Eurofer97 that the indentation method serves not only for an identification and quantification of radiation damage, but also for systematic studies in repairing techniques on a minimum volume of material. In a second part, the fracture toughness of irradiated materials is of interest and will be investigated based upon the use of a cube corner tip which is more appropriate for initiation of cracks.

5.1 Investigation of Post-Irradiation Annealing Effects

Investigations performed on austenitic steels [70] and on early developed RAFM steels [71] showed that one efficient method for healing radiation damage consists in a thermal heat treatment after the irradiation of materials. It came out from these studies that the displacement damage usually anneals out above $0.4\,T_m$, where T_m corresponds to the melting temperature of the material. Hence, post-irradiation annealing can be used as a technique to minimize the effects of irradiation on tensile and impact properties, which can lead in the end to an increase of the lifetime of the fusion reactors. More recent post-irradiation annealings were performed by Petersen et al. on Eurofer97 specimens after a 15 dpa irradiation at T_{irr} in the fast reactor BOR 60 of the State Scientific Center of Russian Federation Research Institute of Atomic Reactors (Program ARBOR 1) [12] [70]. It could be demonstrated that annealing at 550 °C for 3 h leads to a thermal recovery in the irradiated material. As can be seen from Figure 5.1, the DBTT (ductile to brittle transition temperature) and USE (upper shelf energy) properties of strongly irradiated Eurofer97 Charpy specimens approach the original values measured in the case of non-irradiated samples. Additionally, results from tensile tests realized with cylindrical specimens of 7 mm gauge length and 2 mm diameter and irradiated in the same conditions [12] had confirmed that a recovery of the yield strength $R_{p0.2}$ and the uniform elongation A_g occurs at 550 °C annealing, while no effect could be detected for an annealing temperature of 450 °C. It is now of interest to further investigate the possibilities to reduce irradiation damage - detected

by changes in the material's strength - by post-irradiation annealing.
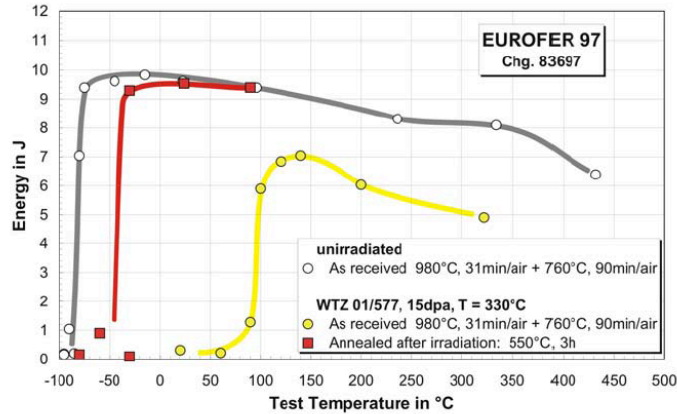
a
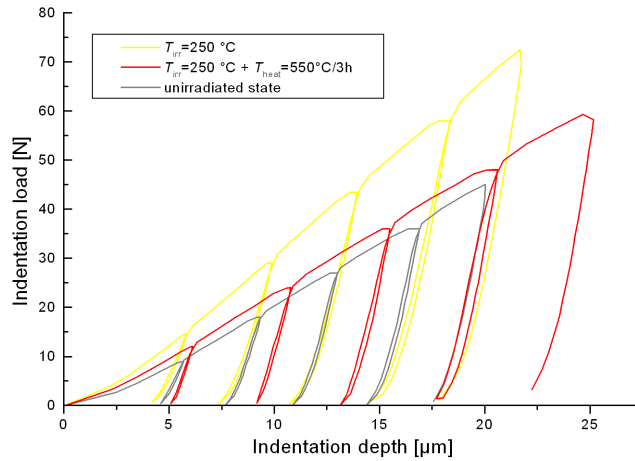
b

Figure 5.1: Comparison of the evolution of Eurofer97's mechanical properties before and after post-irradiation annealing (a) Charpy impact properties [12], (b) Load-depth indentation responses

According to the observations mentioned above, it was decided to investigate the effects of annealing treatments from $500\,°C$ to $550\,°C$ and for different annealing times up to 3 h on the recovery of the material properties. The heat treatments are carried out in vacuum at a heating rate of $20\,°C/min$ on Eurofer97 specimens initially irradiated at $250\,°C$ / 15 dpa. Figure 5.2 and Figure 5.3 show respectively the values of H_v and $R_{p0.2}$, normalized to the values of the unirradiated material as a function of the annealing conditions for the two pre-irradiation heat treatments of Eurofer97 (see Section A.3).

In this study, the annealing temperature of $500\,°C$ was found to be the minimum temperature for starting recovery. Indeed, annealing for one hour already induces a significant decrease of the material's strength. After three hours at this temperature of annealing, the embrittlement further decreases, but Eurofer97 still exhibits a remaining hardening. Generally, the recovery of the strength and hardness for Eurofer97 samples treated at $550\,°C$ during 20 min, 1 h and 3 h is more pronounced than in the
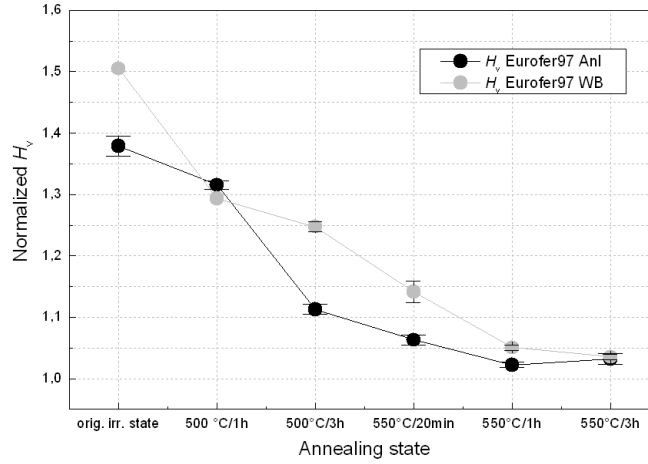
Figure 5.2: Hardness, H_v, of irradiated Eurofer97 Anl and Eurofer97 WB after post-irradiation annealing, normalized to the corresponding unirradiated values [72]
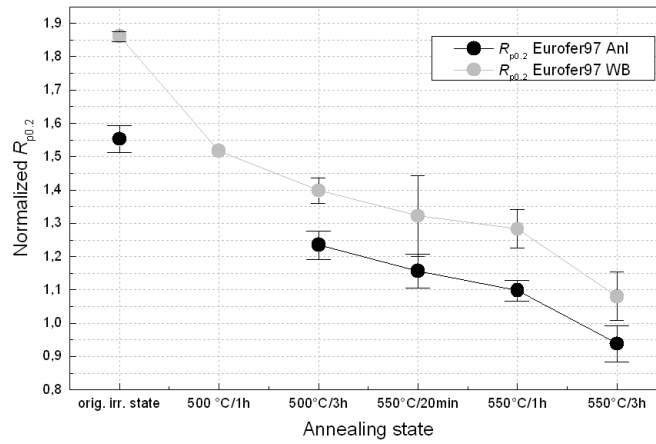
Figure 5.3: Yield strength by IIT, $R_{p0.2}$, of irradiated Eurofer97 Anl and Eurofer97 WB after post-irradiation annealing, normalized to the corresponding unirradiated values [72]

tested temperature of 500 °C for 1h and 3 h. Annealing for 3 h at 550 °C leads to a quasi-complete recovery to the original strength of Eurofer97, considering H_v and $R_{p0.2}$. A residual hardening of 98 MPa and 37 MPa was obtained respectively for H_v and $R_{p0.2}$ in Eurofer97 WB specimens. The observations agree well with those made by Gaganidze and Petersen. Indeed, a significant reduction of the yield stress was measured [13] for Eurofer97 specimens irradiated at T_{irr}=332 °C / 70 dpa and annealed at 550 °C during 1 h and 3 h. This phenomenon was mainly linked to an almost complete recovery of the DBTT at T_{irr}=330 °C / 15 dpa and T_{irr}=330 °C / 70 dpa and following annealing at 550 °C for 3 h [56]. A clear correlation can be established between the measured DBTT for samples irradiated at T_{irr}=330 °C / 15 dpa and annealed at 550 °C / 3h and the mechanical properties calculated by the post-processing tool for samples irradiated at T_{irr}=250 °C / 15 dpa and annealed at 550 °C /3h. The evolution of the load-displacement indentation response before and after the heat treatment is also displayed in Figure 5.1.

The activation energy E_a corresponding to the annealing process has been calculated according to the Arrhenius equation Equation 5.1 and considering the two activation

conditions: $500\,°C$ / 1h and $550\,°C$ / 20 min. In this equation, the term A is the pre-exponential factor, R is the gas constant, and the rate constant k depends on the absolute temperature T in which the reaction takes place. A value of $51\,kJ.mol^{-1}$ has been found for the tested annealing conditions and remains in the range of the activation energy necessary for the release of helium in irradiated austenitic steels [73].

$$k = A \cdot e^{(\frac{E_a}{R \cdot T})} \tag{5.1}$$

Furthermore, it is visible from the analysis of hardness and strength over the tested annealing conditions that Eurofer97 Anl remains globally less affected by the irradiation damage than Eurofer97 WB even in the case of post-irradiation heat treatment. It can be noted that the hardening ratio for the yield strength remains larger than for hardness. This effect was observed and interpreted in the previous chapter section 4.4. especially for samples irradiated at $250\,°C$, and is found here to be persistent over the annealing states as all the annealed samples of this study were originally irradiated at $T_{irr} = 250\,°C$.

In order to investigate the possible evolution of the grain sizes after annealing, etching of irradiated samples was carried out in the metallography Hot Cell. Figure 5.4 shows a comparison of the grain size structure of Eurofer97 Anl in its original irradiated state ($T_{irr} = 250\,°C$), after annealing at $500\,°C$ for 1 h, and after annealing at $550\,°C$ for 3 h. The Röchling etching recipe, which is particularly adapted for steels such as Eurofer97, could not be utilized due to the presence of contents that might lead to blasting in the Hot Cell. Therefore another similar recipe was applied at the surface of the tested materials. Microstructure analyses of the etched surfaces do not indicate a significant visible growth of the grain size that could be at the origin of the general observed decrease of strength over the tested heat-treatments. Hence, the clear decrease of Eurofer97's strength, related to the stabilized grain size at approximately $14\,\mu m$ for the different annealing conditions, suggests that the annealing process is mainly responsible for a recovery of irradiation-induced damages in the material's structure.
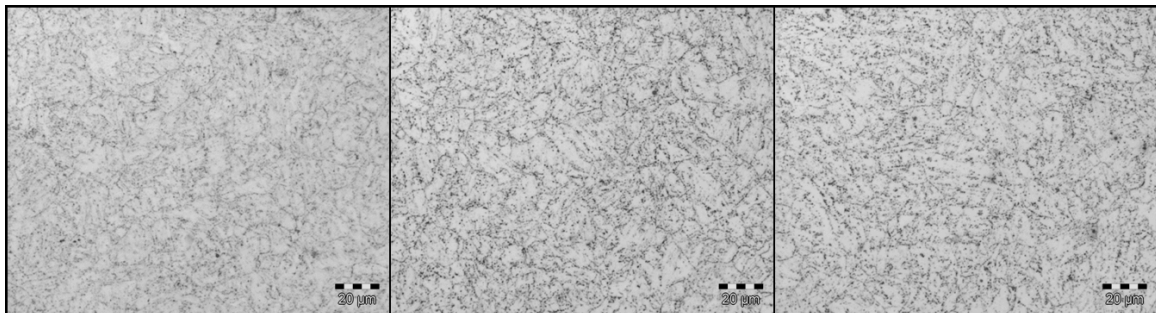
Figure 5.4: Microstructure of Eurofer97 Anl irradiated at $250\,°C$: original irradiated state (left); post-irradiation annealing ($500\,°C$/1h) (middle), post-irradiation annealing ($550\,°C$/3h) (right)

5.2 Investigation of Fracture Toughness

The degradation of fracture toughness observed from impact testing [55; 66; 65; 74] in irradiated tempered ferritic/martensitic steels is a current issue of the developed materials to cope with. It has been previously exposed that such steels become particularly brittle at irradiation temperatures of 250 °C to 300 °C, thus reaching a hardness higher than 3 GPa, a yield strength higher than 800 MPa and a KLST impact energy of less than 1 J at room temperature. Indentations with pyramidal indenter were already successfully employed to generate cracks in glasses or ceramics [75; 76], therefore the instrumented indentation technique is adapted for the study of fracture toughness of brittle materials and will be tested for materials irradiated at 300 °C.

According to the indentation fracture theory, radial (Palmqvist), lateral, median and half-penny cracks are likely to occur [77]. The first type of cracks corresponds to vertical half-penny cracks since they are situated at the corners of the residual impression outside the plastic zone, the second ones are horizontal cracks and are situated beneath the surface, whereas the median cracks are vertical penny cracks and initiate beneath the surface and are directly situated under the residual impression on its axis of symmetry.
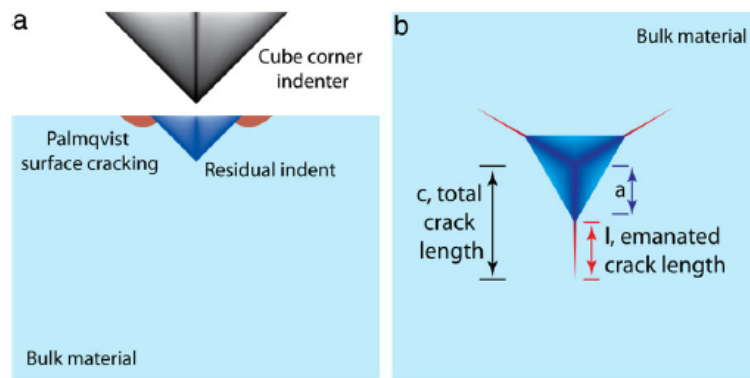
Figure 5.5: Theory of cracking with a cube corner indenter (a) Formation of cracks zone; (b) measure of crack length [78]

The type of indenter tip is decisive for the crack generation. Indeed, as it is mentioned in Section 6.2.2.8, sharp indenters are more suitable than blunt ones for reaching higher plastification rates under the contact area and are thus more appropriate to initiate cracking. A cube-corner indenter was utilized for that purpose because it offers a sharper indentation area than a Vickers one. The fracture toughness K_c resulting from indentation with a cube-corner indenter was proposed by Anstis [78] and can be derived from the following formulation:

$$K_c = \alpha \cdot \left(\frac{E}{H}\right)^{\frac{1}{2}} \cdot \left(\frac{P}{c^{\frac{3}{2}}}\right) \tag{5.2}$$

where α is an empirical constant found to be close to 0.040 for cube-corner geometries, c is the length of the radial crack from the center of the indent, H is the measured hardness and P is he peak load.

Unirradiated Eurofer97 Anl samples were initially indented at 150 N at a load rate of

2 N/s. The same procedure was carried out on F82H-mod irradiated at 300 °C providing a tensile behavior comparable to Eurofer97 Anl at this irradiation temperature. In addition, further indentations up to 190 N and at the loading rates of 2, 5 and 20 N/s were additionally carried out. Figure 5.6 displays the obtained *P-h* curves in the case of 150 N at a loading rate of 2 N/s and shows a comparison of the indentation reached when using a Vickers indenter. A depth increase of factor 2.5 more than in Vickers indentation depth could be achieved at the same load level when using a cube-corner indenter. If comparing the curves obtained both from cube-corner indentations on Eurofer97 (unirradiated state) and F82H-mod (irradiated state), a loss of 15 µm indentation penetration could have been detected and is explained by the increase in strength present in F82H-mod. The analysis of the load indentation curve has not revealed any pop-in or pop-out effect that might indicate occurrence of cracks.
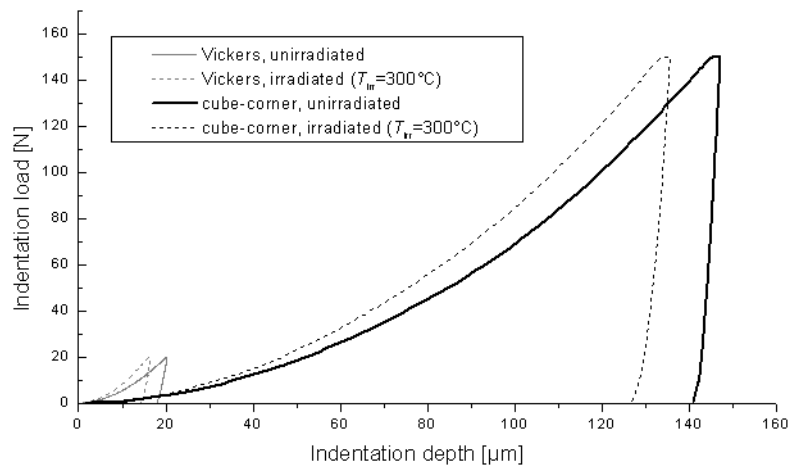
Figure 5.6: Indentation curves of irradiated and unirradiated RAFM steels with Vickers and cube corner indenters

Images acquired both from a light microscope and SEM did not indicate the presence of radial or half-penny cracks, at the corners of a residual impressions of F82H-mod, as it is visible in Figure 5.7. It is evident that a high amount of plastic flow has occurred in comparison with the ball indentation performed up to 25 µm.
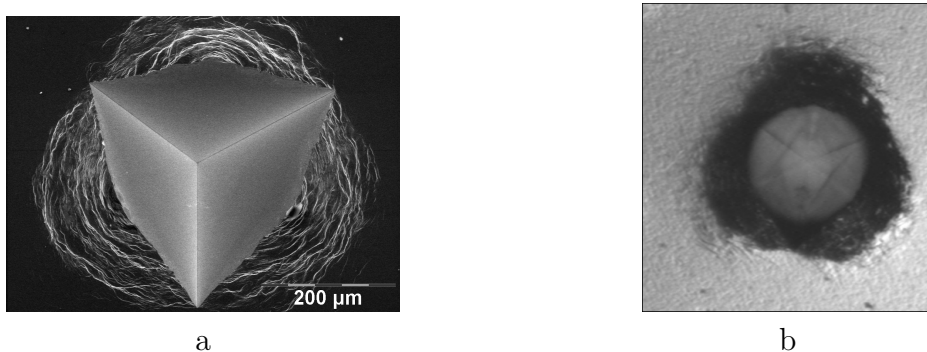
Figure 5.7: cube corner residual indent (maximal applied load:150 N) (a) SEM (b) light microscope

The indentation energy W_{tot} was calculated from the *P-h* curve by Equation 2.4. An energy of less than 0.01 J was induced from the indentation at a maximum loading

a   b
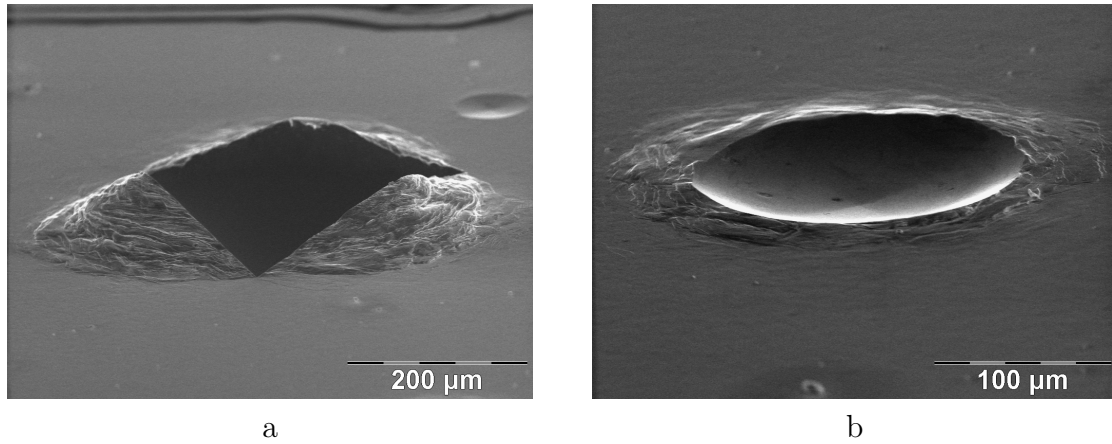
Figure 5.8: Comparison of induced plastic flow from cube-corner (a) and Rockwell (b) indentation on irradiated steels

of $190\,\mathrm{N}$ over an average contact area of $0.06\,\mathrm{mm}^2$. This energy is not sufficient to give rise to radial cracks; therefore a direct measurement of fracture toughness is not possible in this testing condition. According to the indentation cracking theory, the radial crack c is measured from the center of the indent, a minimal length of c is then set to ca. $200\,\mathrm{\mu m}$ until the corner of the indent is reached for the case of indentations performed at $190\,\mathrm{N}$. This condition implies that the irradiated F82H-mod sample is highly expected to have a fracture toughness value higher than $20\,\mathrm{MPa.m}^{1/2}$. Previous studies [79] have shown that, for RAFM steels irradiated at $300\,^\circ\mathrm{C}$ up to a dose of $8.81\,\mathrm{dpa}$, the normalized K_{Jc} lies within $50\,\mathrm{MPa.m}^{1/2}$. Considering this study and the performed indentation tests, it is expected that Eurofer97 and F82H-mod irradiated at $300\,^\circ\mathrm{C}/15\,\mathrm{dpa}$ exhibit a fracture toughness in the range of $20\text{-}50\,\mathrm{MPa.m}^{1/2}$. Further investigations on irradiated samples will be conducted to confirm this expectation. It should be noted that median or lateral cracks may have occurred beneath the indented surface of the irradiated F82H-mod sample, but could not have been checked according to current remote handling limitations existing in Hot Cells, when using the accurate cutting tools required for investigations of the indent´s cross section. Indentations on MANET I samples irradiated at $0.8\,\mathrm{dpa}$ and characterized by a more pronounced decrease of the fracture toughness (K_{ID} direct is lower than $10\,\mathrm{MPa.m}^{1/2}$ at $\mathrm{T}_{irr}=300\,^\circ\mathrm{C}$), and will help verifying the ability of indentation to investigate the fracture toughness of irradiated embrittled steels.

5.3 Insight in Material Characterization by Indentation at High Temperature

The instrumented indentation technique was applied in this chapter to investigate the changes in mechanical properties resulting from post-irradiation heat treatment. Additionally, it was used as a potential tool for the analysis of material's toughness. Another potential of the instrumented indentation technique is to test samples at high temperature, which is particularly relevant for a better understanding of the mechanical behavior of irradiated steels in their operating conditions. Nanoindentations at $500\,^\circ\mathrm{C}$ were performed at the site of ONERA, with the newly developed indentation device [44], on non-irradiated Eurofer97 samples. These experiments already provide

an insight into the changes of indentation mechanical properties at higher temperatures (see Figure 5.9). For comparison, pyramidal nanoindentations were perfomed at room temperature with an MTS device. An increase of the maximum indentation depth by almost 22 %, as well as a resulting hardness decrease by 40 %, could be predicted for high temperature tests. According to Equation 2.5, the reduced modulus, E_r, is additionally falling from 245 GPa to 109 GPa.
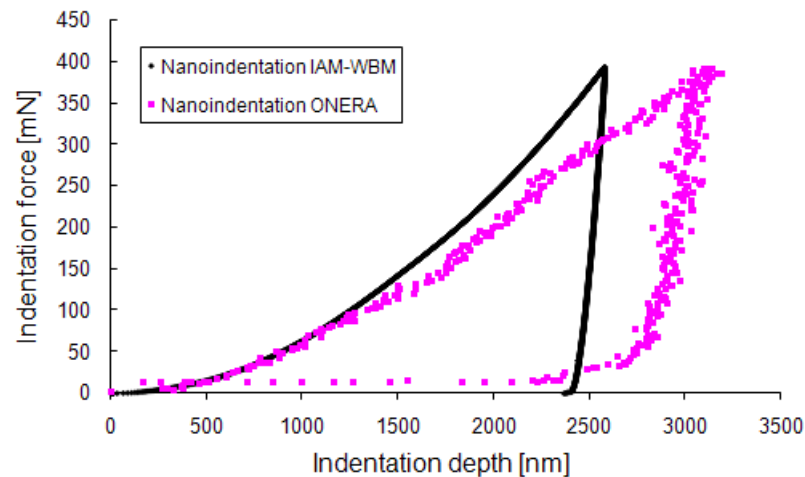
Figure 5.9: Comparison of nanoindentation at room and high temperature (500 °C) on Eurofer97 (unirradiated state)

These characterizations reveal promising possible investigations of such materials, especially at higher testing scales as this is of interest within this project. The coming chapters explore more in detail the different development phases required for the design of a high temperature instrumented macroindentation device.

Chapter 6

Development of a High Temperature Indentation Device

This chapter is dedicated to the development of an instrumented indentation machine for indentation on heated samples. As mentioned before, this testing device is mainly required to achieve further information regarding the high-temperature mechanical behavior of steels relevant for fusion applications. In the following, the generally required specifications are described, and the machine design is presented with a description of its main functionalities.

6.1 Required Testing Specifications

The main specifications of the testing rig are initially selected considering the properties of the current employed Zwick indentation device, with which satisfying results have been delivered at room temperature. Especially, the frame of this machine was considered to be a good basis for the concept of the new indentation device. The required specifications are related to the three most relevant test parameters: temperature, force, and indentation depth. Another aspect considered as a characteristic testing condition, concerns the testing atmosphere defined by the necessary applied vacuum. The main specifications required for the device are further detailed in the coming sections and summarized as follows:

- Loading range: from 2 to 200 N

- Resolution of the depth-sensing system: from 20 to 100 nm

- Temperature range: from 20 to 650 °C

- High vacuum : from 10^{-4} to 10^{-5} mbar

6.1.1 Force Range and Resolution

High forces are appropriate to characterize hard materials. In the present project, metallic materials such as steels and tungsten are to be investigated. Indents performed with the Z2.5 machine and with a Rockwell indenter of 200 μm radius on irradiated Eurofer97 Anl samples require an approximate peak load of 80 N in order to reach the indentation depth range necessary for the data-post-analysis method

depending on the radius chosen for the tip. A maximum load of 180 N is needed for tungsten and tungsten alloys when using a Rockwell tip with a radius of 250 µm [21]. In this respect, selecting a radius smaller than 200 µm radius would enable performing tests at a smaller maximum force. However, the final maximum indentation depth, which is required for the analysis tool, would consequently be reduced while the resolution of force and depth of the system remain identical. This would lead to a loss of information on the experimental curve, which would in turn lead to a general degradation of the measurement quality. For all these reasons a force application and measurement in the range of 2 to 200 N is suitable within the framework of the present application.

The force resolution plays an important role for the assessment of the materials properties by the post-analysis tool. Indeed, in usual cases the accuracy of the measurement is the most relevant characteristic and the resolution plays a minor role in the final accuracy of the measured value. In that particular application the resolution has an indirect influence on the accuracy of final results. In the present application, the force resolution defines the number of measured force values available on the experimental curves. Generally, the more data points are delivered, and the finer the experimental curve will be, better interpolation of the post-analysis tool, and finally exacter materials properties assessment are expected. The effect of a reduced resolution has been particularly investigated in the case of the indentation depth; information referring to this is given in the next part. Tests with the current used device at a force resolution of 0.01 % and with a measurement accuracy of 1 % of the force range lead, among the other specifications characterizing the testing device, to a deviation of a 2.4 % for the calculated yield strength of Eurofer97 Anl in its unirradiated state in comparison with tensile tests results. Considering these measurements, Eurofer97 was defined as reference material for further experiments, and especially for the coming study regarding the influence of the displacement resolution. This deviation calculated for the yield strength of unirradiated Eurofer97 demonstrates that the machine's force resolution is one factor of good quality results. Therefore, it was decided to maintain the current by used system resolution of 0.01 %.

6.1.2 Depth Range and Resolution

Materials studied in the micrometer and macrometer range experience penetrations for a minimum depth of 200 nm as defined by the ISO 14577 [50]. More precisely, the depth range of interest for the present application is mainly imposed by the range of validity of the neural networks based analysis tool. According to the fact that the test is a load-controlled test, the maximal force at the fourth loading cycle has to be selected in order to ensure a penetration in the valid range required for the analysis tool. In the present case, the maximal allowable penetration is given by Equation 3.1 and remains around 20 µm if using a Rockwell indenter radius of 200 µm. This requirement for the displacement range remains identical for the new device since the size of the used indenter remains the same. As a consequence, the depth sensing system used for the machine to be developed should provide a minimal measuring depth range of ca. 30 µm. A maximal indentation depth of 250 µm is allowed in the current used indentation system. Moreover, it should be noted that standard Vickers hardness tests performed at 20 N did not exceed 25 µm in the case of RAFM steels.

In addition to the indentation depth range, the depth sensing resolution plays a sig-

nificant role in the assessment of material properties. The displacement resolution defines the size of the smallest increment of indentation depth which can be detected by the depth sensing system during the penetration of the indenter into the sample. As it is the case for the accuracy of the depth sensing system, the depth resolution is a factor of influence for the quality of the results. Indeed, the more data points are delivered on the experimental curve the more accurate the material properties are assessed.

A second relevant aspect for providing high resolution experimental data is to measure with a good sensitivity the changes in indentation depth induced by thermal deformations occurring at the heated tip. In the present application, the detection of the smallest change in apparent expansion of the indenter is necessary to be measured in order to correlate afterwards the measured depths to the time dependent changes in force. This will enable to reconstruct a correct load-depth experimental curve.

Before making a choice of a depth sensing system, it becomes necessary to define what the displacement resolution required for the present application really is. For this purpose, a study is realized to determine to which extend this system property can influence the quality of the results calculated by the post analysis tool. The aim of that study is to define the acceptable range of resolution that guaranties a satisfying assessment of materials properties. A code is written to simulate the effects resulting from the use of different displacement transducers. These transducers are supposed to have the identical characteristics except for the displacement resolution. It should be noted here that a displacement resolution lower than 200 nm is not adapted for the use of the neural networks based method at indentation depths reaching 20 µm. This is mainly due to the fact that the analysis tool interpolates a total number of 100 data points from the original data points for the loading and creep segments [20]. Hence, providing a lower number of data points than those required by the tool for the interpolation would significantly decrease the quality of interpolated new data points.

The modifications induced by the code for variations of resolutions are shown in Figure 6.1a. This figure illustrates the data points corresponding to a segment of the P-h curve which is obtained artificially for different simulated displacement resolutions. The more the quality of the displacement resolution is decreased, the more load values are associated with the same value of depth. A given experimental curve, coming from a real test performed with the current device with the resolution of 20 nm, is modified afterwards by the code in order to get a curve with a number of data points corresponding to a specified resolution. The time resolution provided by the original displacement measuring system is maintained for the simulations of other displacement resolutions. The study was performed for almost forty experimental curves, with resolutions varying from 20 nm to 100 nm. For each modified experimental curve corresponding to a defined resolution, a calculation of three material properties of materials the Young's modulus E, the yield stress k_0, and the viscosity exponent m was achieved with the neural networks based method.

Additionally, a criterion of satisfaction of 10 % of deviation was defined to be acceptable when considering the discrepancy of calculated parameters to the values calculated with the original data for a resolution of 20 nm.

As can be seen in Figure 6.2, E and k_0 are less sensitive to the displacement resolution than m. This can be explained by the fact that m is a power parameter and is more sensitive than E and k_0 to variations of the plastic strain rate which is more affected

when the depth resolution is modified as it is visible in Figure 6.1b. This graph clearly shows that the amount of data corresponding to the indentation depth is significantly reduced during the creep phase if the displacement resolution is degraded from 20 nm to 100 nm. At a resolution of 40 nm, a discrepancy of m already reaches 10 %, whereas discrepancies of E and k_0 remain under 10 % even at 100 nm of resolution. The parameter m was considered not to be representative of the effects in indentation depths variations according to its too high sensitivity. Also, the analysis of the stress-strain curves on Figure 6.3 calculated for the different displacement resolutions confirms the slight changes of curves compared to the original curve. It was concluded from this study that a displacement resolution up to 100 nm is still acceptable for a proper assessment of materials properties in the elastic and inelastic region.
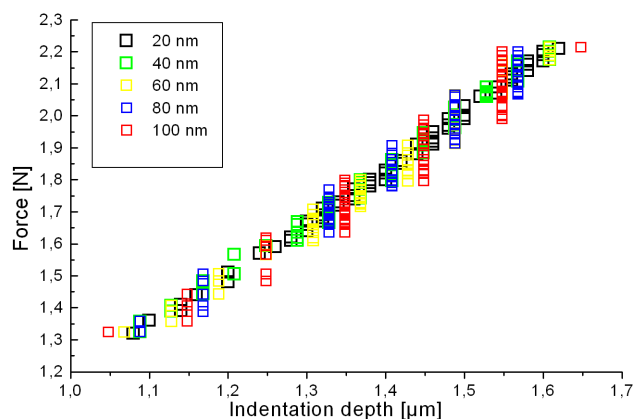
a
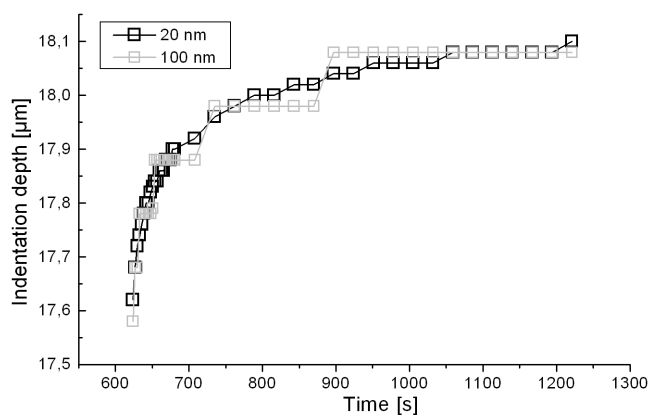
b

Figure 6.1: (a) Modification of the original P-h curve (with a resolution of 20 nm) for different resolution from 40 nm to 100 nm (only the beginning of the loading part P-h curve is displayed for visualization ease) (b) Creep phase with two displacement resolutions (20 nm: real experimental data, 100 nm: simulated data)
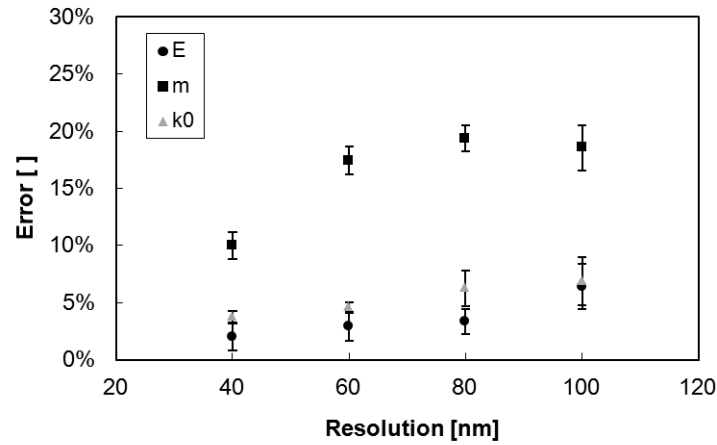
Figure 6.2: Discrepancy of three materials parameters to the original values corresponding to a displacement resolution of 20 nm
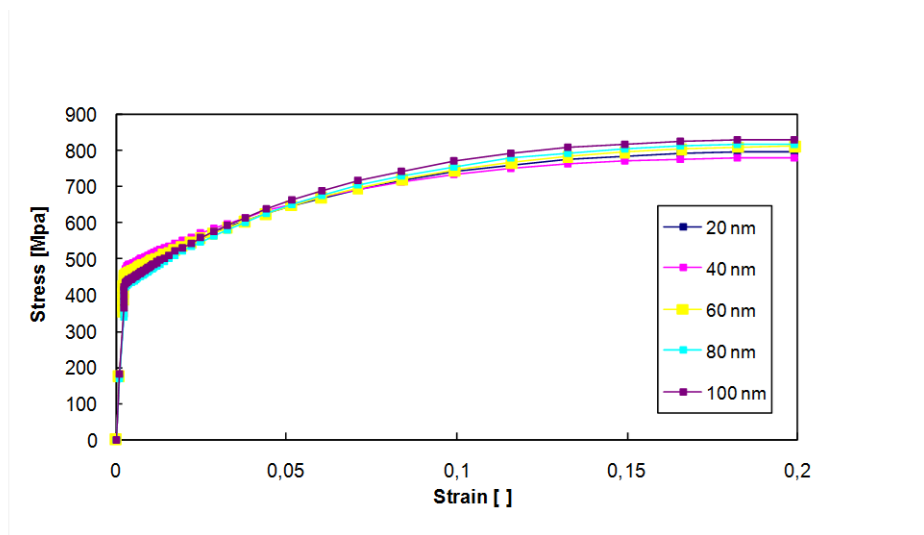
Figure 6.3: Identified stress-strain curves with different displacement resolutions

6.1.3 Heating Specifications

The maximum temperature to be provided by the indentation device is 650 °C. This is chosen to perform experiments up to the maximal operating temperature of RAFM steels and RAFM-ODS steels in fusion reactors being 550 °C and 650 °C, [80; 81] respectively.

In the indentation instrument, both sample and tip will have to be heated to the same temperature in order to avoid substantial heat flow due to a temperature gradient when the contact is realized [36]. Generally, the heat transfer induced at the contact surface leads to a time-depedent variation of the size of the heated bodies. The thermally-induced dilatation takes place at the indenter holder and the sample, and is finally responsible for an incertitude of the measurement.

A temperature regulation at the sample and the tip is needed to ensure a better

stability in temperature of the heated sample area in contact with the tip. Moreover, heating both units allows reaching a thermal equilibrium at the contact more rapidly than without heating the tip, this can finally represent a significant gain of time for the whole testing period.

Heat flow is responsible for a decrease of the initially applied temperature at the specimen. The heating system has the function of reading and regulating the temperature. However, even by heating both elements at a close temperature, the temperatures of the tip and the sample may remain different, and slight fluctuations of temperature of the tip and the sample are occurring during the phase of contact. Many factors of influence are responsible for the variations of temperature at the surface of the sample during the test. Some of them are listed as follows:

- Environmental factors such as radiation and convection occurring in the testing area. Integrated cooling system at the low and upper part induce a thermal gradient.

- Differences in thermal properties of heated parts

- Accuracy of the temperature measurement and correction at the heated bodies. This depends both on the area selected for the temperature measurement and the specifications of the selected heating system.

The change in force signals induced by thermal deformations at the indenter is measured by a load cell and consequently readjusted by the integrated electronic force regulation system. The acquisition rate of the force signal and the time response delay for the force regulation are limiting factors for an instantaneous correction of the force. The depth sensing system has to be able to detect simultaneously with a high temporal resolution the exhibited thermal expansion or contraction of the tip. The temporal synchronization of the time-dependent displacement and force measures becomes particularly relevant in case of thermal drift occurrence, thus allowing a correlation between the change in depth and the time corresponding change in force. The heating unit will mainly be selected according to its ability to generate enough heat at the sample and tip location. In the present context, the need in power mainly depends on the selected heating system and the geometric properties of the unit to be heated. In Chapter 7, an assessment of the power needed for heating the sample and the tip until $650\,°C$ is demonstrated by means of numerical simulations. Additionally, the thermal expansion of the indenter holder is simulated at high temperature in order to provide information about the impact of the heating system accuracy the local dilatation.

6.1.4   Vacuum Specifications

The two main interests of performing the tests in vacuum is to avoid oxidization especially of the tested samples and to minimize the heat propagation into the rest of the machine. At high temperature, the formation of oxide layers is accelerated in ferrite materials [82]. Additionally, it will be demonstrated in Section 6.2.2.8 that high vacuum applications becomes particularly relevant for reducing the oxidation of the diamond tip at high temperatures. This time-dependent phenomenon particularly occurs at the surface of the materials meaning that the hardness measurement of

the bulk material to be tested can be affected. Therefore, a control of oxidation is necessary and will allow a more appropriate characterization of materials.

The use of a vacuum chamber helps minimizing the heat propagation in the whole testing device so that parts of the device are less subjected to thermal loadings. Moreover, a sealed vacuum chamber has the advantage to protect the testing area from convection phenomena induced by the ventilation system of the Hot Cells, and hence ensures a better temperature stability during the test.

Ultra-high vacuum (UHV) is often required for test temperature over $1000\,°C$, whereas high vacuum is usually adapted for applications in the range up to $600\,°C$. RAFM steels and tungsten alloys are the materials of interest for this project. Oxidation of tungsten in air under $600\,°C$ is minimal but still occurs [83], and ferritic-martensitic steels, even if containing a proportion of 7 to 9 wt.% Cr characterizing a relative good resistance against corrosion, are likely to exhibit some oxidation. In the present study, a pressure of $1.5 \cdot 10^{-5}$ mbar was selected, and a reference specimen of Eurofer97 polished as used before (Section 3.1.2.1) was investigated. Investigations of the changes at the surface of the sample is here of interest, the Auger electron spectroscopy (AES) technique was used for that purpose. The tested temperature of $500\,°C$ corresponding to the approximate limit of operation for Eurofer97 was maintained in the vaccum oven for a heating period of $1\,h$. This test duration was chosen because it corresponds approximately to the time necessary for one indentation test.

For comparison, three polished specimens of Eurofer97 exposed to the atmospheric pressure were previously investigated by AES. The analysis shows that an initial oxide layer of ca. $8\,nm$ composed of an upper layer of $2\,nm$ iron oxide and an lower layer of iron oxide and chromium oxide is present at the surface of all specimens as shown in Figure 6.4a.
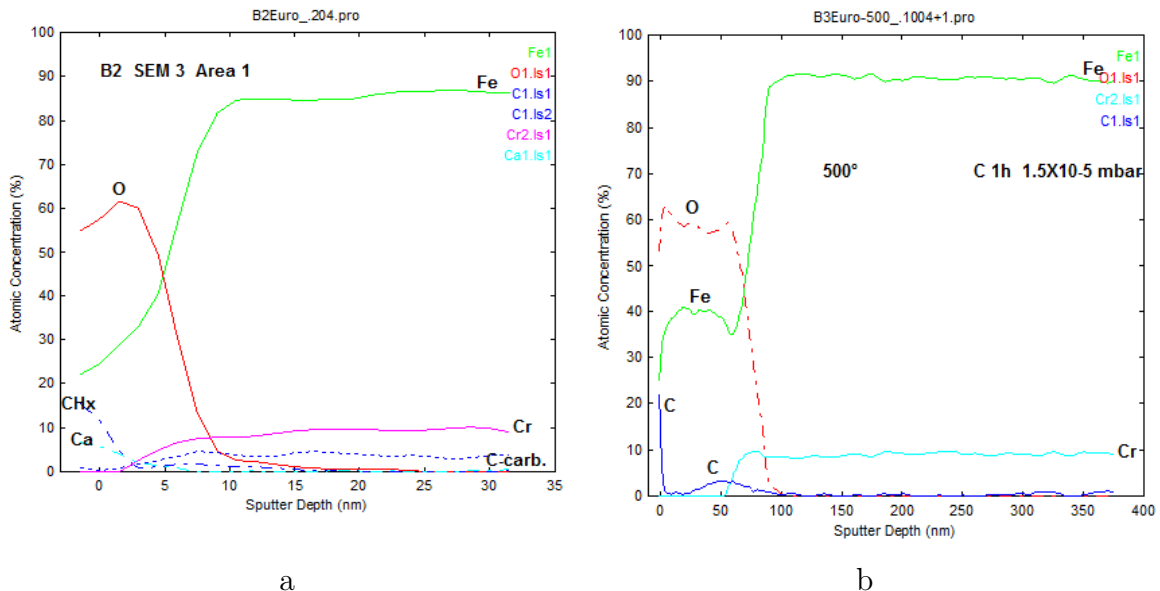
Figure 6.4: Atomic concentration of different elements at the surface of Eurofer97 at $22\,°C$ (a), after heating at $500\,°C$ and $1.5 \cdot 10^{-5}$ mbar (b)

In comparison with these observations, the investigation of the specimen tested at $500\,°C$ and $1.5 \cdot 10^{-5}$ mbar during $1\,h$ showed a slight evolution of the oxide layer thickness, principally made of an upper layer of $50\,nm$ iron oxide (Fe_2O_3) and a

lower one of 30 nm iron oxide and chromium oxide (spinel), growing up to 80 nm as displayed on Figure 6.4b. This result indicates that the oxide layer built in high vacuum at 500 °C is not significant in comparison with the total indentation depth of approximately 20 μm to be performed and leads in the range of the requirement for the depth resolution. Therefore, the thickness of such oxide layers is expected to play a negligible role on the measurement of the original material properties. Even though a high vacuum testing area will help reduce significantly the oxidation of the tested steels, the influence of a thin oxide layer formed at the surface of the sample is not clearly known at the moment and might still have a slight influence on the change of the mechanical properties of the original tested material. Additional studies are planned for the investigation of the impact of oxidation on Eurofer97 at test temperatures from 250 to 550 °C on the assessment of mechanical properties by the technique of indentation.

6.2 Concept of the Indentation Device

6.2.1 General Concept

A concept of the indentation device to be installed in the Hot Cell is proposed below (see Figure 6.5). The indentation testing device is principally composed of the frame structure, the loading unit, the heating unit, the depth-sensing unit and the vacuum unit. The characteristics of the main units required for the testing device are described in the coming section.
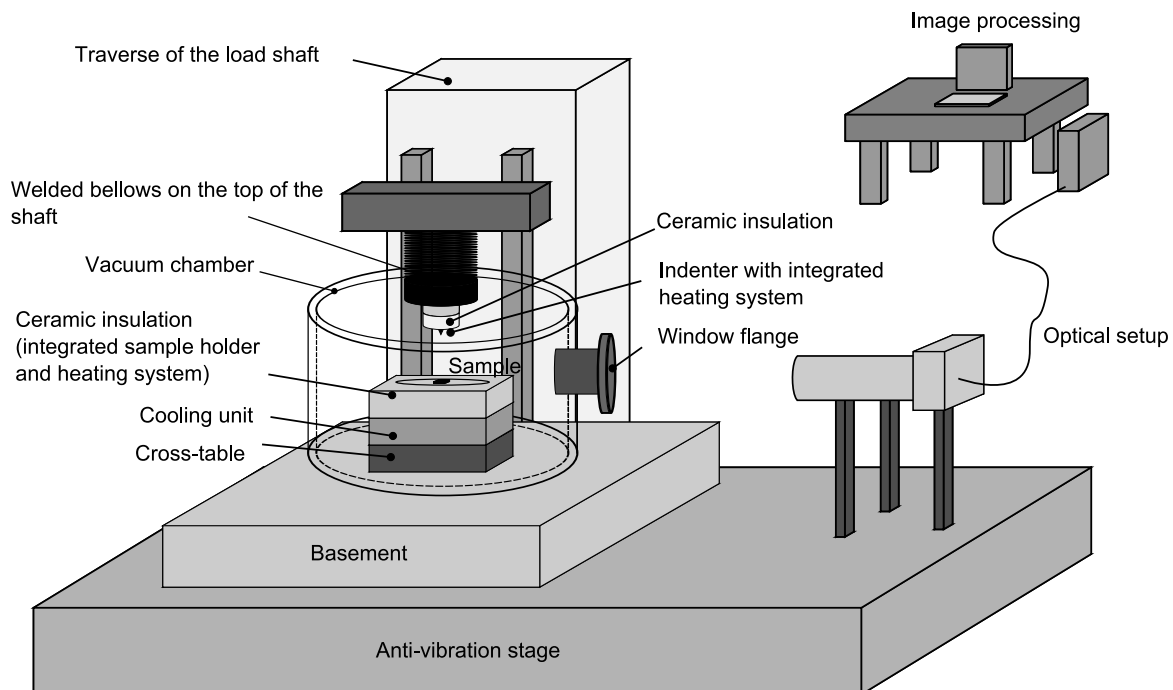
Figure 6.5: General concept of the instrumented indentation device for high temperature tests

6.2.2 Required Main Units and Functionalities

6.2.2.1 Frame Structure

The basic structure is primordial for the stability of the whole device. This part determines the main compliance of the whole system. The same construction principle as used in the Zwick indentation machine can be adapted. A C-shape frame with a compliance of 208 nm/N is featured by the loading frame to which the mobile indenting shaft is attached and by the basement that supports the whole device.

6.2.2.2 Vacuum Chamber

The vacuum chamber acts as a vessel confining the heated components and provides a high vacuum atmosphere to avoid oxidation of the tested specimen. The chamber has to be manufactured for an adjustment of the optical unit used for the measurement of the indentation depth, and provides different flanges for inspection and for externally connected electronic units. The characteristics of the vacuum system used for the final machine design are more detailed in Chapter 9. In this concept, the chamber is fixed at its bottom to the basement. As a consequence, the upper part of the chamber is conceived to permit the displacement of the loading shaft, moving along the load frame, by means of a welded bellow. Loading and unloading of the indenter is achieved when the welded bellow contracts and expands respectively.

6.2.2.3 Heating System

The choice and the characteristics of the heating system are detailed in Chapter 7.

6.2.2.4 Cooling System

Tip and sample are to be heated and are responsible for warming of surrounding components. Two areas require to be especially protected from the heat: the sample XY positioning system and the upper part of the loading shaft where the load cell is attached. For these two critical locations, a water cooling system will be integrated to minimize the effects of the heat.

6.2.2.5 Sample Positioning System

A stage acting as cross-table is required for the positioning in X and Y directions of the sample in order to define places of indentation on the sample surface for different tests. A displacement range of 10 to 50 mm and a resolution close to 10 µm, as it is the case in the Zwick device, are needed for the positioning of the specimen. That system has to be sufficiently protected from the heat for three main reasons. First of all, the table is usually composed of materials, like joinings and electronics, which are not appropriate to operate at temperatures above 100 °C. Second, the table if heated will endure thermal expansion leading to a displacement of the whole system linked to the sample during the test. Therefore, a cooling system is required between the heating plate and the positioning system, this will ensure that the positioning system operates in its defined temperature range.

6.2.2.6   Sensing Units

- Load cell

A load sensor is needed to measure the applied load, up to 200 N, during the force-controlled test. In the present concept, the load cell is attached to the arm moving along the loading frame and fixed to the upper part of the loading shaft so that the contact force between the indenter to the sample is directly measured. The load cell is also essential for the detection of the contact of the indenter at the surface of the sample, thus the beginning of the test can be established. Standard load cells operating at room temperature give better measurement quality than cells manufactured for operation at high temperatures. Therefore, the load cell has to be efficiently protected from the heat coming from the lower part of the heated shaft by using if necessary an additional cooling system located at the upper part of the chamber. Numerical analyses are carried out to determine the temperature of the upper part of the loading shaft according to its length and materials. Results are presented in Chapter 7.

- Electronic unit

The electronic unit of Zwick is selected for the regulation of the force and for the connection to the external monitoring software. It is mainly integrated inside a housing attached to the machine's load frame.

- Depth sensing unit

An optical sensing unit is selected in this work for the measurement of the displacement of the indenter. A system combining a digital camera and macro objective is placed in front of the inspection window of the vacuum chamber and is connected to a computer used for image acquisition and situated outside the Hot Cell. Further details about the principle of the measurement are provided in Chapter 8.

6.2.2.7   Loading Shaft

The loading shaft ensures the displacement of the indenter. It is located inside the welded bellow and fixed on its upper part to the arm driving along the traverse. Its displacement is enabled by the contraction or expansion of the welded bellow. That unit has especially to be resistant to thermal loading caused by the heating of the indenter and to mechanical compression loading. Therefore, the choice of a Al_2O_3 ceramic-like is suitable for that application. Numerical simulations presented in Chapter 7 show that a shaft entirely made of Al_2O_3 and having a length of 200 mm is adapted to ensure a significant reduction of the heat propagation in the shaft, especially at the defined location of the load cell.

6.2.2.8   Indenter

Two parts of the indenter system are distinguished: the tip (with a Rockwell or a Vickers geometry), and the tip holder at which the tip is usually brazed. The indenter is connected to the loading shaft and is removable by means of an adapted screw system. The tip holder is a crucial component of the device and has to be manufactured in a

way that it both can be properly heated and elongates as less as possible in reaction of the temperature variations. This calls for a material having a high thermal conductivity and a low coefficient of thermal expansion. Analyses of thermal properties of materials used for high temperatures applications have led to the choice of a molybdenum alloy as holder material. In addition to its good mechanical resistance in the case of a compressive load up to $200\,\mathrm{N}$, this material is adapted for an operation up to $650\,^{\circ}\mathrm{C}$ and ensures a high thermal conductivity in the range of $145\,\mathrm{W/(m\cdot^{\circ}K)}$ as well as a low thermal expansion in the range of $5.2\cdot10^{-6}\,^{\circ}\mathrm{K}^{-1}$ at room temperature. These properties remain more suitable for the application compared to non-refractory metals and especially standard stainless steels usually selected for manufacturing indenters. The standard technique used for the connection of the tip to its holder is the brazing technique. Up to now this has been successfully applied for testing conditions up to $500\,^{\circ}\mathrm{C}$ and is currently not adapted for higher temperature testing conditions up to $650\,^{\circ}\mathrm{C}$. The alternative connection technique is based on a mechanical grip system and will be further developed for the present project.

As it is the case for many materials, diamond oxidizes more rapidly at elevated temperatures. The oxidation phenomenon is characterized by the formation of both a carbon layer on the surface of the diamond and CO_2 gas. This process differs from the graphitization phenomenon that occurs at temperatures higher than $1200\,^{\circ}\mathrm{C}$ [84; 85]. Consequences of this process are blunting of conical and pyramidal indenter tips, which is characterized by a constant etch rate. Considering the fact that oxidation is a time, oxygen pressure, and temperature-dependent, it is minimized when working in vacuum atmosphere conditions. Figure 6.6 displays the oxidative etch rate of diamond, for different crystallographic orientations, depending on the equivalent atmospheric pressure and the temperature. It is obvious that diamond rapidly oxidizes in air, on the contrary, the diamond etch rate is assumed to be lower than tens of $\mathrm{nm\cdot h}^{-1}$ for temperatures lower than $650\,^{\circ}\mathrm{C}$ and partial pressures situated in the range of $1\cdot10^{-5}\,\mathrm{mbar}$. Such a rate is considered to be negligible for indentations performed at the micro-macro scale. A diamond tip is then convenient for indentation tests up to $700\,^{\circ}\mathrm{C}$ since it is employed in high vacuum atmosphere as it is planned for the present project. Nevertheless, attention should be paid regarding the evolution of properties of the heated diamond tip, and regular inspections of its surface should be performed e.g. by indentation in calibration materials. Another alternative is the use of a tip made of sapphire which remains chemically more stable than diamond in air at high temperatures. However, sapphire is not adapted for indentation of materials with similar or greater hardness as well as for relative high indentation force. It has been numerically verified that an indentation in a tungsten-like material until an indentation depth of $19\,\mu\mathrm{m}$ required for the post-analysis tool generates a maximal Von Mises stress of more than $5\cdot10^9\,\mathrm{Pa}$ thus exceeding the allowed compressive strength of sapphire of $2\cdot10^9\,\mathrm{Pa}$. In addition to that, the post-analysis code has been trained with indentation data based on the properties of a diamond indenter, using another indenter material would lead to deviations in the assessment of materials properties.

6.2.2.9 Sample Holder

A sample holder system is needed to fix the position of the specimen during the test. A mechanical clamping system was selected for the present application. Further details are given in Chapter 7. The sample holder corresponds here to a heating block
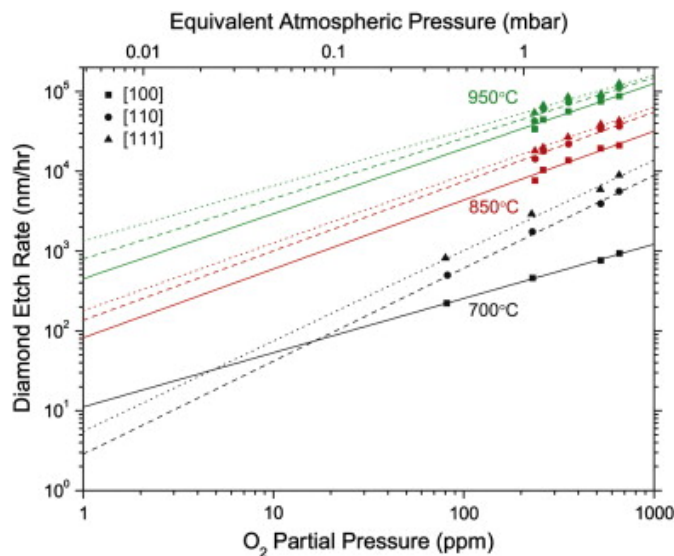
Figure 6.6: Oxidative etch rate of heated diamond [86]

integrating the heating elements.

6.2.2.10   Anti-vibration Stage

Floor vibrations around 10 Hz are caused by outside vibrations coming from operation of other machines, air-conditioning system or directly from the operation of the indentation machine. External vibrations due to remote handling in neighbor boxes can lead to a variation of force up to 2 N. Such vibrations affect the quality of the experimental indentation curve and have to be minimized. It will be demonstrated in the following that the presence of an anti-vibration stage is relevant for a better accuracy of the optical indentation depth measurement. Such a stage ensures a better stability in the testing conditions by isolating the instrumented indentation device from floor vibrations.

Further details about the heating system, the loading shaft, and the indenter are given in Chapter 7. Numerical simulations are carried out after modeling the main principle units of the instrument and help defining the power requirement for the tip and the sample and some of their materials and geometrical properties. Moreover, a study is realized for an adaptation of a displacement measuring system to the high temperature indentation instrument. Results of this study are detailed in Chapter 8.

Chapter 7

Development of a Heating System

The sample and the tip have to be heated up to 650 °C by an appropriate heating system. Three systems, each based on a specific mode of heat energy transfer, were initially selected. Their benefits and limitations of use for the present application are presented in the first section of this chapter. Then a heating system is selected, for which a numerical study is presented to define the requirement in power for the heating of the sample and the tip up to 650 °C.

7.1   Potential Heating Systems

The induction heating process is based on the electromagnetic induction that is generated in the tested material by means of an alternating current passing through an electromagnet. The electromagnet generates a force on the free electrons of the material to be heated and hence, generates an electric current in the body. The energy resulting from this process is finally dissipated in the body by heat. This simple way of heating has limitations in the present application. Usually, only large sizes of coils - too voluminous for the indentation test - are available. This would imply significant adaptations for the design of the whole heating system. One other important constraint is given by the electric field generated in the testing environment by the electromagnetic induction. This is known to cause measurement errors at nearby sensors. For instance, the temperature measurement by thermocouples situated in the heated area may be strongly affected. Such sensors are highly sensitive to small variations of electric current, their voltage potential difference can be modified from the surrounding electromagnetic field and finally lead to an erroneous measurement of the real temperature. For these two reasons mentioned above, the induction has been exluded as heating system for the indentation device.

The radiation heat energy transfer mode used by lasers was also envisaged for the present application. Continuous wave (CW) lasers are often employed in industrial applications such as heat treatment of materials or welding of metals [87; 88]. Depending on the category of lasers, they deliver output powers over 600 W with beam diameters smaller than 5 mm and are capable of heating at temperatures over 1000 °C with high accuracy and rapidity [89]. That type of heating has the advantage that the heat is precisely focused by the laser at the zone of interest so that the heating is localized, which prevents other parts of the machine to be unnecessarily heated. Nevertheless, this method needs the installation of additional optical units that have to be pre-

cisely positioned in the system. The laser unit cannot withstand high temperatures, and thus has to be either fixed far enough from the heated area or sufficiently water cooled. Units such as quartz lenses having the function of focusing the laser beam onto the sample or the tip are also needed. The glass units should have to be positioned in that case very close to the irradiated sample, which means that the influence of the gamma-radiation of the sample becomes more important. This is known to produce changes of the optical properties of the glass, causing a time-dependent darkening of the glass [90]. This would imply a frequent change of optical units, which is not convenient if considering the general difficulties of remote handling in Hot Cells.

Electrical resistance elements are finally discussed. Resistors are often used for heat transfer by conduction. They are usually integrated at the inner wall of a testing chamber which becomes in this case an oven. The disadvantage is that it warms the whole testing volume confined in the oven. As a result, all units situated inside the hot area are thermally loaded. Additionally, the device will require a more efficient cooling system than in the case of a localized heating. Another solution is to position resistors in direct contact with the bodies to be heated. This solution provides a more localized heating of the bodies and thus requires less power than heating homogeneously the whole testing chamber. With this method, relative small heating elements, like plates or cartridges, are integrated into a heating plate situated under the specimen to ensure an efficient thermal conductivity between the resistor and the body (see Figure 7.1) [91]. Small sized heaters of less than 50 mm length and 10 mm diameter used for industrial applications provide output power up to ca. 300 W and withstand temperatures up to approximately 800 °C. These two aspects could be limiting factors for the use of such resistor heaters in the present application. Indeed, resistor plates provide limited power with respect to their size and are limited to an approximate specific charge of 15 W/cm^2, whereas cartridges heaters are approximately limited to 50 W/cm^2. Nevertheless, resistors heaters remain a convenient solution for the present application considering their relative simplicity of use and economical aspects if comparing to other existing heating systems.

Numerical thermal analyses, performed with the finite element analysis code ANSYS [92; 93], will help determine the power requirements in order to reach the maximal temperature of 650 °C at the specimen and the indenter in order to validate the selection of the heating system. The heating of the tip and the sample are analyzed separately according to the fact that each of them has to be heated in a first step at the same temperature without any contact.

7.2   Heating of the Tip

Generally, materials and dimensions of the model parts are selected to fulfill the following main criterion: reaching a maximum temperature of 650 °C at the tip in a range of 30 min. A first configuration of the indenter-loading-shaft system has been initially considered [94] according to the simplicity of the selected heating element geometry as shown in Appendix B. A small-sized flat heating element assimilated to a resistor plate of a 60 mm^2 surface was selected to be positioned at the top of the indenter in order to heat its upper part. More details about the properties of the model are given in the following section, where a similar model is presented. Thermal transient simulations based on the initial defined system configuration have led to the
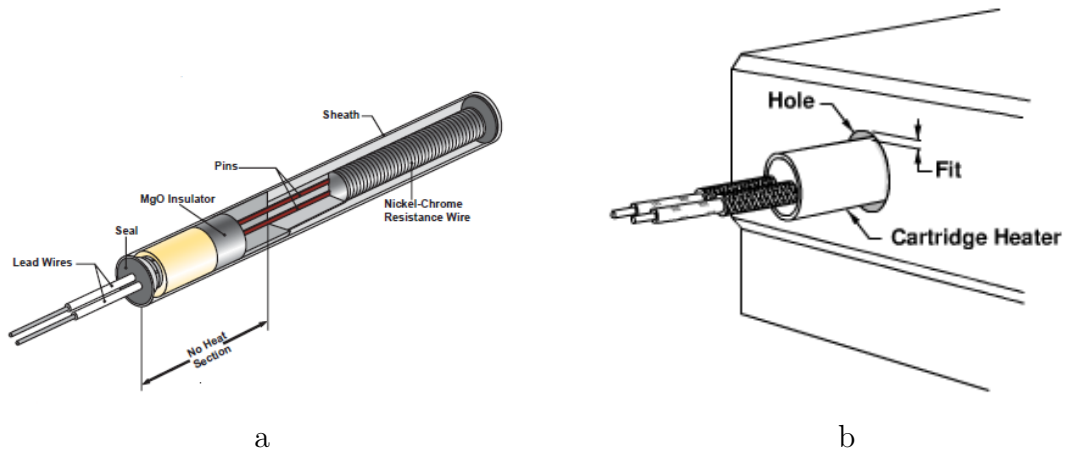
Figure 7.1: (a) Cartridge heater; (b) integration of a cartridge into a fitted hole [91]

conclusion that a power of 47 W is required to heat the tip in almost 14 min. According to specifications delivered from manufacturers of heaters, it is found that this power was not accessible for resistor plates of the modeled sizes of heating element. Therefore, a second model of loading shaft-indenter system is defined with new dimensions of the heating element and characterized by the presence of ceramic insulation for a better heating efficiency. The power demand is investigated for this model.

7.2.1   Selected Model Configuration: Model Description

The final tested model consists a small-sized cylinder, assimilated to a cartridge with a length of 30 mm and 6.5 mm diameter made of stainless steel 1.4876 as provided from the manufacturer, which is inserted into the drill-hole of the indenter as illustrated in Figure 7.2. In this model, the geometry of the tip holder was simplified and built to be assimilated to the currently used indenter geometries.

The dimensions of the Rockwell indenter geometry, used in the present work for indentation at room temperature, was taken as reference for the model, with a tip made of diamond bonded to its end. The material of the indenter was mainly selected according to the criterions detailed in Section 6.2.2.8 . A good compromise is found between a relative low thermal coefficient of expansion lying by $5.2 \cdot 10^{-6}\,\mathrm{m/(m \cdot °K)}$ and a high thermal conductivity of $145\,\mathrm{W/(m \cdot °K)}$. A heat insulation is necessary to surround the heated indenter in order to confine the heat for a more efficient heating. A ceramic insulation with a diameter of 27 mm and 35 mm height with a thermal conduction coefficient of $5\,\mathrm{W/(m \cdot °K)}$ close to Cordierite-like ceramics was modeled. The loading shaft has the thermal properties of a Al_2O_3 ceramic which provides a thermal conduction evolving in the range of 20 to $10\,\mathrm{W/(m \cdot °K)}$ in the range of 20 to 600 °C [95]. This material has been selected according to its good mechanical compressive strength and ability to operate in heated systems. The whole shaft has a diameter of 70 mm with a total length of 200 mm. The boundary conditions corresponding to the thermal *simulation 2* which is of main interest within this study are displayed in Figure 7.2. The complete finite element model involves 12882 nodes and 4812 elements and is presented in Appendix B.

A Convection (all): 0,1 W/m^2.°C
B Radiation (ceramic insulation): 0,5
C Radiation (tip): 0,02
D Radiation(cartridge): 0,3
E Radiation(indenter holder): 0,3
F Radiation (shaft): 0,5
G Heat flow (cartridge): 100 W

a   b
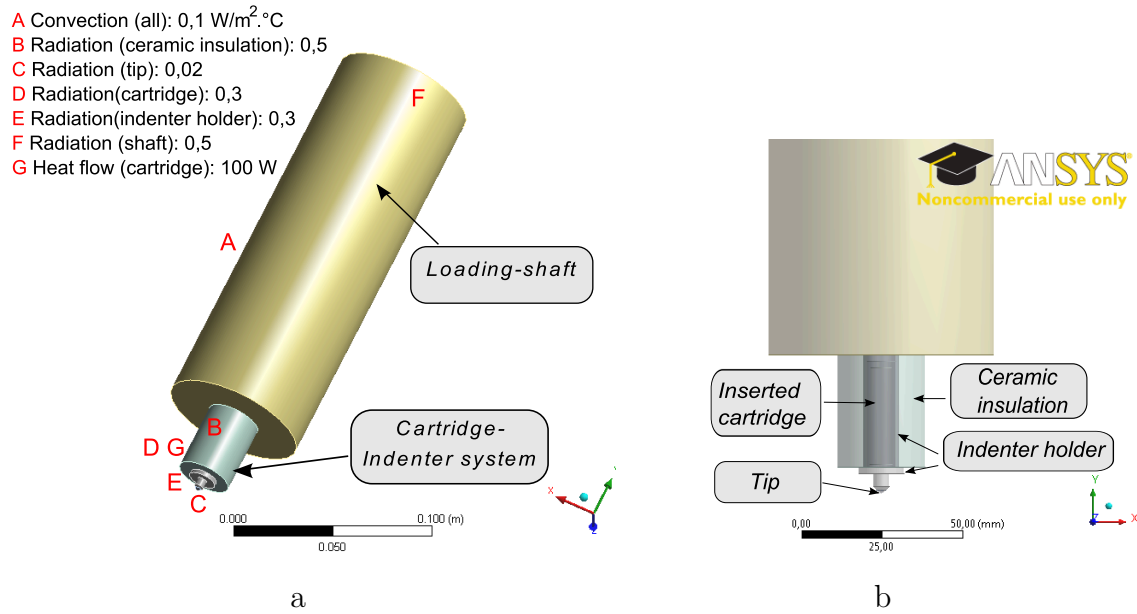
Figure 7.2: (a)Loading-shaft model (whole system) with the boundary conditions of *simulation 2*, (b)Cartridge-Indenter system (lower part of the loading shaft)

7.2.2   Selected Model Configuration: Required Power

In the thermal simulations, a heat flow was applied at the heating element simulating the heat output delivered by the cartridge. Convection in high vacuum atmosphere is assumed to be negligible, therefore a low value of $0.1\,\text{W}/(\text{m}\cdot°\text{K})$ instead of 0 was applied at all surfaces of the modeled bodies. Thermal conduction was assumed to be the dominant heat transfer mode in a first step [96], so that the effects of thermal radiation were not taken into account in that simulation called *simulation 1*. A power of $40\,\text{W}$ coming from the cylindrical heating element was required to heat the diamond tip to $647\,°\text{C}$ in about $14\,\text{min}$ as shown in Figure 7.3.
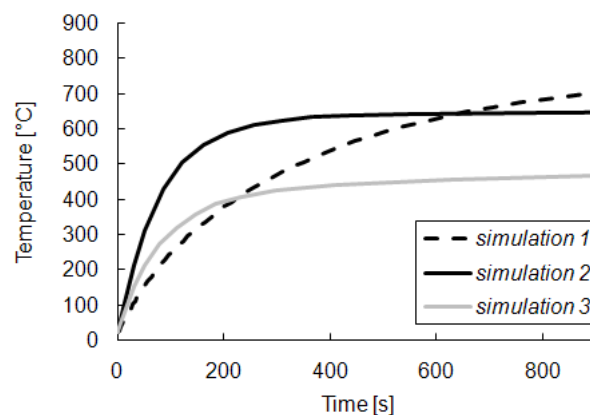
Figure 7.3: Comparison of the temperature evolution at the tip for different modes of heat transfer and for two different heat insulations (*simulation 1*: Corderite-like ceramic/no thermal radiation/ Power of $40\,\text{W}$; *simulation 2*: Corderite-like ceramic/thermal radiation/ Power of $100\,\text{W}$; *simulation 3*: Al_2O_3-like ceramic/thermal radiation/ Power of $100\,\text{W}$)

Thermal radiations of materials were taken into account in a second step of the

analysis corresponding to *simulation 2*. The emissivity of each part of the model was defined in accordance with the corresponding material as detailed in Appendix B [97]. A heat flow of 100 W corresponding to a specific charge of 16.5 W·cm^{-2} at the cartridge was here required to heat the diamond tip up to 650 °C in approximately the same time period as in the thermal analysis with no consideration of radiation effect (see Figure 7.3). A significant amount of heat loss results from the radiations of materials, this can be identified from the asymptotic slope of the curve in *simulation 2* showing that more heating power is needed to increase the temperature whereas this is not necessary in the case of no consideration of thermal radiation as in *simulation 1*. Nevertheless, all the instrument's parts surrounding the heated bodies also have emissivity properties, this is notably the case of the vacuum vessel which should contribute to a better confinement of the heat and especially to a partial reflectivity of the heat to the original heated bodies. Such effects should consequently lead to a decrease in the power need of the cartridge. In order to stay in conservative assumptions, properties of emissivity have to be considered as it is the case for *simulation 2* and the coming analyses.

7.2.3   Selected Model Configuration: System's Constraints

Figure 7.4 shows the inertia of the tip temperature evolution in comparison with the temperature at the cartridge. After 850 s the cartridge reaches a temperature of almost 830 °C whereas the tip has reached 650 °C. The numerical simulation predicts a limit of the heating of the tip to approximately 600 °C according to the constraints of use of cartridges having a maximal operating temperature of 800 °C.
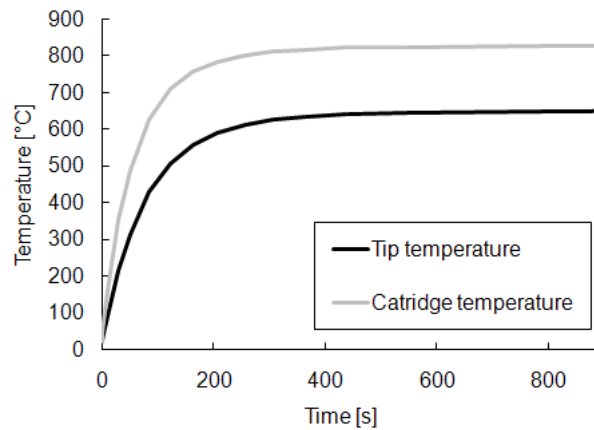
Figure 7.4: Evolution of the tip and cartridge temperature

   Also, it has been determined that a thermal conductivity lower than 5 W/(m·°K) of the ceramic heat insulation is required for the criterions of heating. The insertion of a ceramic assimilated to Al_2O_3 having a higher thermal conductivity allowed a heating of the tip up to 450 °C to 514 °C in respectively 14 min to 1 h in the case of an identical power heat flow of 100 W applied at the cartridge (see *simulation 3* in Figure 7.3). A power of 180 W was needed to reach a tip temperature of 650 °C in the modeled configuration while the temperature of the cartridge would have exceed 990 °C. In order to avoid an overheat of the cartridge, a cartridge heater not exceeding a power of 100 W and a specific charge of 16.5 W·cm^{-2} is convenient for the present application

and is found in *simulation 2* to deliver an average heating rate of $46\,°C \cdot min^{-1}$ until the temperature of $650\,°C$ is reached at the tip (see Figure 7.5).
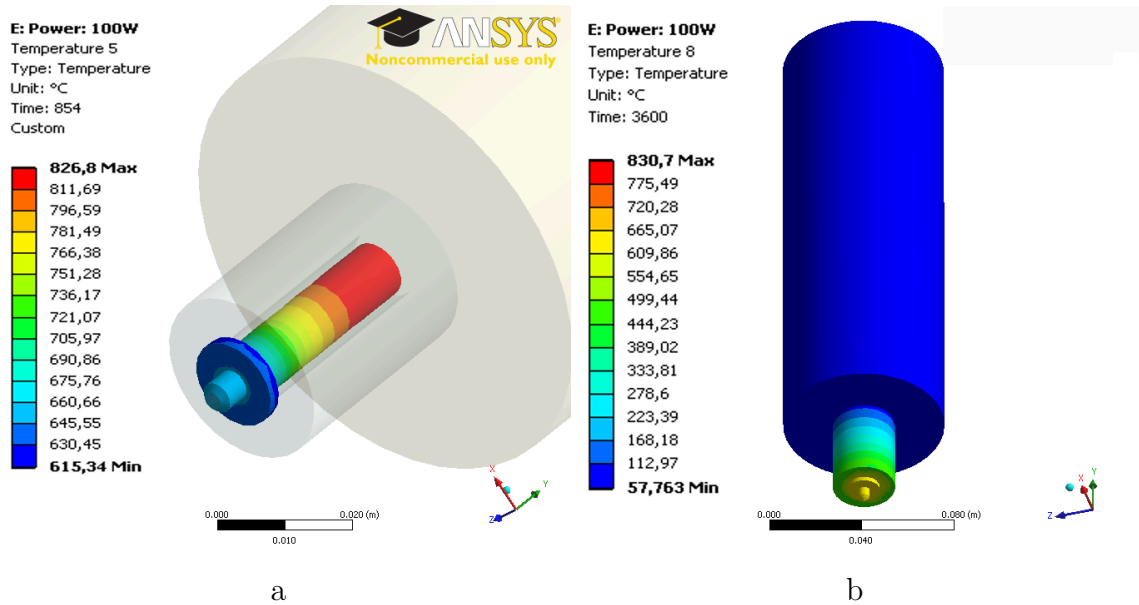
Figure 7.5: Temperature of the indenter tip and the loading shaft for an applied power of 100 W with a Cordierite-like ceramic heat insulation; (a) indender holder and tip; (b)whole loading shaft system

Moreover, the analysis *simulation 2* of the temperature evolution at the loading shaft shows that, for a shaft made of Al_2O_3 and of 200 mm length, the positioning of a force transducer operating at standard maximal temperature of $60\,°C$, at the shaft's top is realistic for a test of approximately 1 h even without any additional cooling system. Indeed, the temperature at the top of the shaft reaches $58\,°C$ after heating during 3600 s which corresponds to the approximate time of one indentation test (see Figure 7.5).

7.2.4   Selected Model Configuration: Accuracy of the heating system

In this section, the indenter holder is submitted to a thermal loading of up to $600\,°C$ at the internal surface of the drill-hole, the initial temperature of the body is of $22\,°C$. The motion of the indenter holder is constrained at the upper surface of the shoulder where the load is transmitted.

After the temperature of $600\,°C$ has been reached at the tip, an expansion of 29µm is predicted from the shoulder surface to the tip as can be seen in Figure 7.6.

Additionally, a dilatation of 98 nm is expected when the temperature is varied from $2\,°C$ at $600\,°C$. Hence, the thermal expansion calculated lies in the range of the displacement resolution to be used, meaning that variations of the indentation depth due to the thermal induced expansion might be measured during the test. In the case of a 100 nm displacement resolution and assuming that the accuracy of the heating system is close to $2\,°C$ as it will be explained in Chapter 9, the thermal expansion induced locally at the indenter by a temperature variation of $2\,°C$ might not have a significant impact on the change of the *P-h* curve.
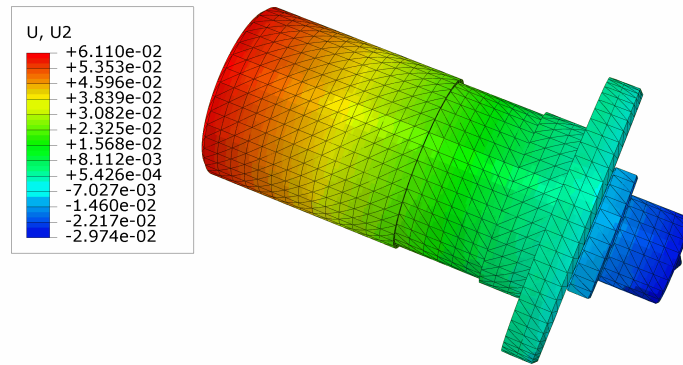
Figure 7.6: Dilatation of the molybdenum indenter at 600 °C

7.3   Heating of the Sample

A first configuration of the heating plate is initially investigated. Figure B.7 illustrates the proposed design. A block made of a low conductive ceramic prevents the sample positioning stage, situated underneath in the machine concept, to be heated. The ceramic also offers a low thermal expansion in order to minimize effects of elevation of the specimen. A clamping system has been selected to fix the position of the sample for the test. The left clamping jaw stays fixed, giving a reference position of the sample for the indentations, whereas the right one is movable screws and allows different sizes of samples to be tested. The proposed heating plate resides on the integration of a cartridge heater in each clamping jaw. In this way, an efficient heating by conduction is provided from the two sides of the sample and a homogenous temperature field is reached at the surface of the sample (see Figure B.7).

A Convection (all): 0,1 W/m^2.°C
B Radiation (ceramic insulation): 0,5
C Radiation (cartridge1): 0,3
D Radiation (cartridge2): 0,3
E Radiation (push-up plate): 0,3
F Radiation (sample): 0,3
G Radiation (heating plate): 0,3
H Temperature (lower surface): 22 °C
I Heat flow (cartridge1): 270 W
J Heat flow (cartridge2): 270 W
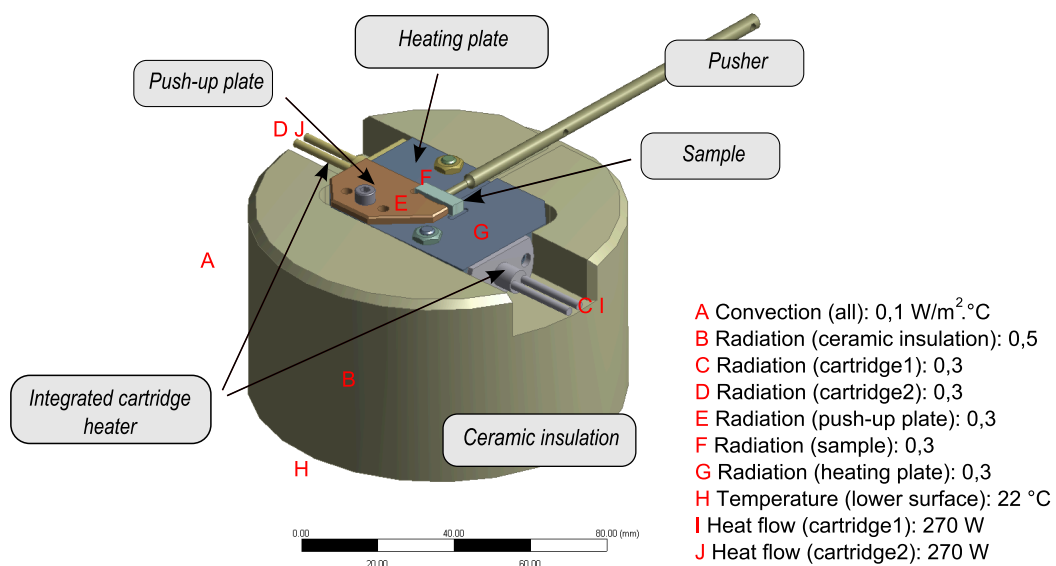
Figure 7.7: Final design of the heating stage-sample holder

Thermal analyses are performed with the corresponding finite elements model. It is demonstrated that the clamping jaw should be composed of two connected parts for an efficient heating of the sample. A first part including the cartridge should be made of relative low conductive material such as an Al_2O_3, a second plate directly connected to the ceramic part and put into contact with the sample should be made of a high conductive material such as molybdenum. The same standard size of the two integrated cartridges were used, as in the case of the tip heating, for an optimized heating of the small specimen. With a power density of $50\,\text{W}\cdot\text{m}^{-2}$, the cartridge heats the specimen up to $650\,^\circ\text{C}$ in about $26\,\text{min}$. If considering manufacturing aspects, this system presents one main difficulty concerning the integration of the cartridge into the ceramic jaw; the ceramic needs to be drilled over a length of at least $30\,\text{mm}$, which requires high performance and costly machining involving hard drill such as sapphire drill. Therefore, a second design of the sample heating system was defined in collaboration with the manufacturer HKE (see Figure 7.7).
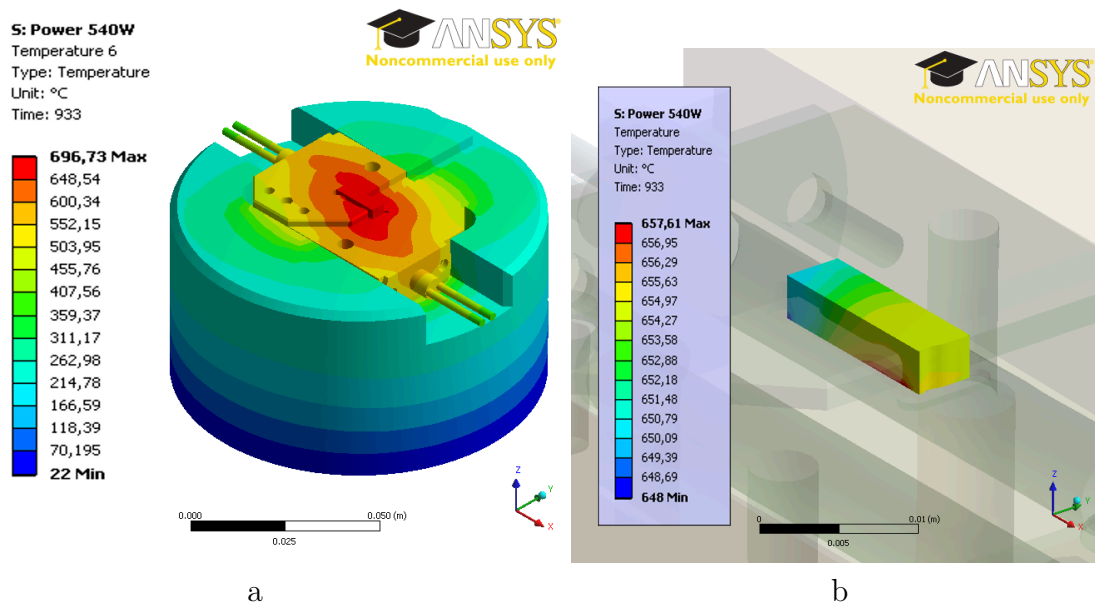
Figure 7.8: (a) Temperature distribution in the whole sample holder system; (b) Temperature distribution in the sample

The heating stage is composed of a heating plate and a heat insulation. The insulation is made of Zerodur-like ceramic which is especially convenient for low thermal conductivity and low thermal expansion. This insulation is $100\,\text{mm}$ thick. The heating plate is made of stainless steel (1.4841) that integrates two small sized cartridge heaters of $6.5\,\text{mm}$ diameter and $40\,\text{mm}$ length. A system composed of a pusher and push-up plate position, also made of stainless steel, enable the reference positioning of the specimen.

In this study, the finite element model involves 21639 nodes and 20162 elements (see Appendix B). Radiation as well as convection effects are taken into account as in the previous analysis concerning the heating of the tip. The boundary conditions used for the thermal simulation are displayed in Figure 7.7. A cooling system situated under the ceramic insulation is foreseen to be integrated in order to cool the underneath sample positioning system, for that reason a condition of $22\,^\circ\text{C}$ has been imposed in the model at the lower face of the ceramic insulation. All the conditions are displayed

in Appendix B.

Considering these system properties, a total power of 540 W (see Figure 7.8) [72], corresponding to a specific charge 32 W·cm^{-2} for each cartridge, is required to heat the sample at 650 °C in ca. 16 min thus providing an expected heating rate of 41 °C·min^{-1} (see Figure 7.9).
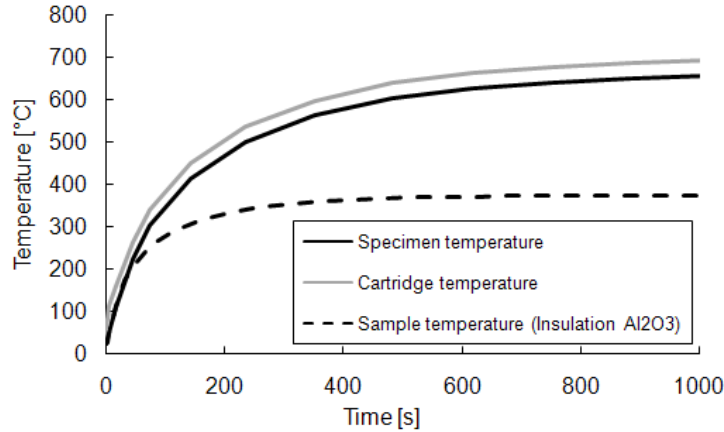
Figure 7.9: Temperature of the cartridge and the sample in the sample holder

System's Constraints

It has been identified that the use of a low conductive ceramic is decisive for the heating of the specimen until the maximal temperature of 650 °C. Indeed, with the thermal conduction of standard Al_2O_3 ceramics, a temperature of 370 °C is reached at the sample after 15 min for a cartridge specific charge of 32 W·cm^{-2} (see Figure 7.9, whereas in the case of the maximum allowable specific heat charge of 50 W·cm^{-2} a maximal temperature of 570 °C is reached after 15 min heating (see Appendix B). Contrary to the case of the tip heating, the maximum operating temperature of the cartridge is not attained for both cases of simulated ceramics, meaning that a cartridge with a specific charge of 50 W·cm^{-2} can be either adapted to a ceramic heat insulation made of Zerodur or Al_2O_3.

Additionally, it should be notified that the presence of the pusher and the stop position is likely to be responsible for inhomogeneities in the temperature distribution in the sample. Temperature variations of up to 4 °C are predicted at the surface of the sample without the presence of the pusher as illustrated in Figure 7.8. The additional presence of the pusher implies larger variations of the temperature at the sample. The contact surface existing between the sample and the pusher induces a heat flow from the heated sample to the stainless steel pusher, this can finally lead to differences of up to 16 °C at the surface of the sample (Appendix B). A modification of the geometry of the pusher consisting of a larger contact surface with the sample will be more adapted to reduce the temperature discrepancies and induce a more homogenized temperature distribution in the sample.

Chapter 8

Adaptation of a Depth Sensing System

The experimental load-displacement curve is needed for the post-evaluation of the materials properties. Therefore, a reliable displacement measuring system providing a displacement resolution in the range of 20 nm to 100 nm is required to measure the indentation depth during the test at high temperature.

The currently-used Zwick depth-sensing system is limited to a use at room temperature, the reasons are explained in the first part of this chapter. A research of linear displacement measuring techniques used for measurements at the micron and nanometre scale in mechanical testing devices is realized in a second part. The four main categories of displacement transducers: resistive, capacitive, inductive and optical are initially selected and further analyzed in the framework of a feasibility study. The last part of this chapter gives an insight into the selected measuring method and the corresponding setup developed for further displacement analyses.

8.1 Limitations of the Zwick used Depth-Measuring System

The operating temperature of the incremental encoder used in the Zwick device as depth sensing unit is limited to 50 °C. The proximity of the depth-sensing system to the heated indenter and sample shows the main limitation in using the system of Heidenhain in a high temperature testing device [51].

In addition to the depth-sensing unit, the displacement measuring principle patented by Zwick [25] is limited for a use at low temperatures. At high temperature, thermal expansion will occur at the transducer foot location. This phenomenon is expected to lead to a an elongation of more than 20 µm of the metallic transducer foot when heated up to 600 °C as shown in Figure 8.1. According to the fact that the depth-sensing transducer is directly related to the motion of the transducer foot, the position of the transducer scanning reticle would be modified due to thermal expansion/contraction occurring at the transducer foot. Consequently, the reference positioning of the tip to the sample, required to calculate the initial distance existing between both bodies, as well as the measure of indentation depth, would be directly affected by the unstable behavior of the transducer foot.

Although a temperature calibration of the elongation of the transducer foot could
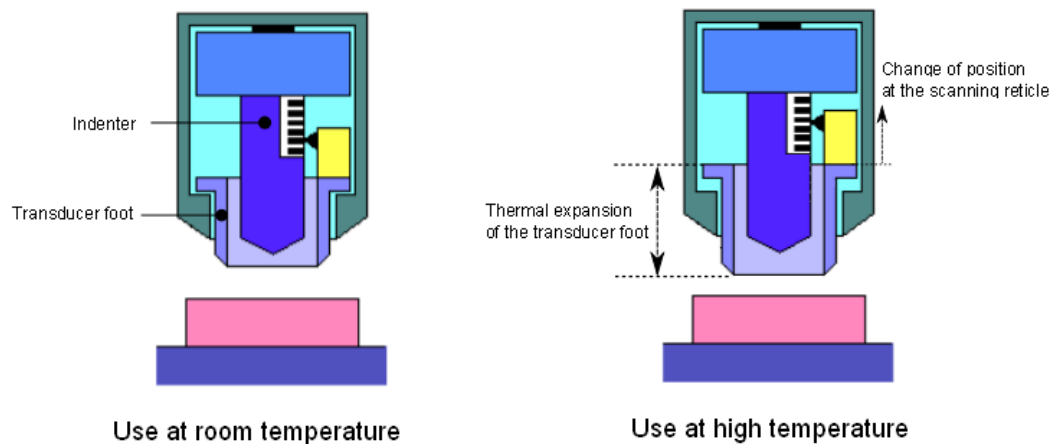
Figure 8.1: Limitation of the Zwick measurement head for a use at at high temperature

have been considered, the incremental encoder remains a barrier for using the whole Zwick depth-sensing system in the new testing device.

8.2 Potential Systems

Another transducer should be adapted to the testing device. A research of the most adapted systems used for linear displacement measurement was carried out for that purpose. Table 8.1 recapitulates the main characteristics and limitations of use of linear position transducers or displacement measuring techniques. This listing results from information provided in the literature and by different manufacturers [98; 99; 100**?** ; 101; 102; 103; 104].

Table 8.1: Specifications of linear displacement transducers

	Capacitive	Inductive		Resistive		Optical setups (laser based systems)		
		Eddy	LVDT	Potentiometer	Strain gauge	Interferometry	Triangulation	FBG (Fiber-Bragg Grating)
Transducer family	non-contacting	non-contacting	"quasi"-contacting	contacting	contacting	non-contacting	non-contacting	contacting
Measuring range (m.r.)	2 mm / 1 mm	0.5-15 mm	1 mm	20-250 mm	mm range	60 mm (m.r. strongly depends on selected optical systems)	40 mm	Several mm
Achievable accuracy (based on nonlinearity)	0.05 % to 0.2 % m.r.	0.25 %	0.15 %	0.25 %	µm range	-	0.05 % r.m.	-
Achievable resolution	0.0003 % 30 nm / 100 nm	0.005 % m.r. 25-750 nm	0.07 % m.r. (~ 1 m)	0.01 mm	µm range	1 nm	500 nm	300 nm
Maximal operating temperature	Standard: 80 °C, Special 250/1000 °C	50 °C	Standard: 80 °C Special: 120 °C	100 °C	300 °C	Optical units are restricted to room temperature operations	50 °C	> 650 °C
Frequency response	2 kHz	up to 25 kHz	5 kHz	1 kHz	-	1 Hz	1 kHz	-
Particular interest	good robustness, small size	small size	good robustness, small size	-	-	high resolution and accuracy	only one instrument of measure required	small size, high strength
Main limitations	Measuring range limited for high resolution, Cooling system required, adaptation of the indenter shaft to the sensor	Efficient cooling system required, adaptation of the indenter shaft to the sensor, restricted to measure of ferromagnetic object	Resolution limited, Efficient cooling system required, adaptation of the indenter shaft to the sensor, sensitive to surrounding electromagnetic field	Actuating force is usually limited to max. 1 N, Long-term wear (required periodic replacement), Voluminous unit (not adapted for use in a mechanical testing device)	Limited in resolution, fixation system not reliable at high temperature	Highly sensitive to vibrations, requirement of several measuring units	The necessary working of the triangulation system for a sufficient resolution is a limitation according to the required size of the vacuum chamber	High resolution limited to low force range < 1 N, high cost

Capacitive transducers belong to the family of contactless sensors. These sensors are convenient for displacement ranges smaller than a millimeter, and are especially adapted for measurements at nano-scale resolution. Additionally, they are robust to harsh conditions in comparison with the other transducers families, and provide the highest operating temperatures.

Due to these abilities, the capacitive sensor is an interesting option and has been retained as second displacement measurement system for the project. Two models from the manufacturers *μ-Epsilon* and *Capacitec* were initially considered. The former operates at 200 °C and provides a maximal measuring range of 5 mm at a resolution of 50 nm, whereas the latter is suitable for applications up to 1000 °C and provides measurement up to 1 mm displacement at a displacement resolution of 100 nm. Nevertheless, such sensors remain limited to small displacement ranges and may require heat insulations.

Resistive sensors correspond to strain gages. This kind of sensor is often utilized in tensile measurement setups because of its simple use based on a contact principle. The gage is usually placed on the surface of samples to study their deformation. The deformation of the sample's surface induces continuous changes of the resistance. One of the main limitations of such sensors is the operating temperature range, indeed, they can be used up to 300 °C, but for higher temperatures their reliability becomes critical. Such gages use glue as fixing system, but these kinds of glues lose their adhesion properties at high temperatures. Furthermore, the highest resolution of such sensors is generally situated at the micro-scale especially for high temperatures conditions. For the previous reasons the strain gage sensor is not considered for the present application.

Inductive sensors and especially the Linear Variable Differential Transformers (LVDT) are also contactless sensors. The displacement of one coil attached to one end in motion generates a change of voltage face to the second coil, which gives the information of displacement changes after conversion of the electrical signal. This kind of sensor can be used at temperatures up to 200 °C and is mostly limited by a resolution of 100 nm. Also, they are more sensitive than capacitive sensors to electromagnetic fields during operation of the machine. This transducer's family is not considered to be the most adapted solution.

Optical measuring systems offer the main advantage to be installed outside hot testing zones, and hence need no particular complex cooling system. Even though the speed of data acquisition is usually limited, optical measurement techniques are generally known to provide measured data with high accuracy and resolution in comparison to other displacement measuring techniques. Moreover, they belong to the category of contactless displacement measuring systems, which means that they are not subjected to mechanical or electrical fatigue induced by the object in motion to be measured and have therefore a higher lifetime than other existing contact transducers. One general limitation of optical measuring setups remains the high sensitivity to vibrations. Therefore, stabilization or damping systems are often additionally mounted for measurement with higher accuracy.

Different optical techniques, such as the interferometry [105], Moiré [106] or speckle correlation techniques [107], are used in the domain of micromechanical testing for measurement of displacement and strain. One representative example of such optical measuring methods is the interferometry. The laser-interferometry offers resolution down to the nanometer regime. However, the optical setup of such systems is composed

of a relative large number of units (mirrors, beam splitter, shutter interference pattern, ...) that should be adapted for a high temperature environment and requiring a high stability for the measurement. According to the complexity of use in the context of an indentation device operating at high temperatures, another optical measuring technique was preferred to the laser-interferometry method and is explained in the following paragraph.

Recent advances in visualization techniques have put forward the interest of digital image processing method. Optimized algorithms associated with high performance optical measuring setups can provide accurate measurement of object's displacement or surface deformations. The optical technique of digital-image correlation (DIC), actively developed in the early 80's [108], requires less apparatus than interferometrical setups. It has already provided conclusive results at the nanometer scale at room temperature [109] and at the micron scale at high temperatures [110].

The image processing method suits better the present application for three main reasons, and the objective is to adapt it and make it work at high temperatures with a nanometric resolution. At first, the optical device can be used outside the hot area of the chamber and thus can be protected from warming, which significantly reduces demands in heat insulations. Then, it uses a non-contacting measurement technique and is thus less affected by any mechanical disturbances. Eventually, and this is the main reason, it can be used with an image-processing tool which provides at the end a displacement resolution better than conventional optical resolutions. In the following sections, the two similar techniques of image processing are presented and tested.

8.3 Optical Measuring System

The optical technique requires an objective with a defined magnification combined with a digital camera capturing images of the object in motion. The camera is connected to a central processing unit for images acquisition and analyses. Two different algorithms were developed by Thompson, Eberl and Gianola and are used as post-processing tool for image processing [110; 111; 112; 113]. The two codes are based upon the digital image correlation method (DIC) and the differential digital image tracking (DDIT) method respectively. The linear displacement of moving targets can be determined by each of both methods. The DIC and the DDIT methods have already provided accurate results at the nanometre scale at room temperature [109], whereas only the DIC is utilized up to now for micron strain measurements of tensile specimens at high temperatures up to 650 °C [110; 114].
The principle of the optical measuring system is schematically shown in Figure 8.2. The optical setup makes use of the following units: a camera, an objective or lens-system, an illumination system, a sample with defined markers, and a software for data processing providing the displacement calculation.

8.3.1 Selected Analysis Methods

The detection of displacement is enabled by the comparison of two pictures acquired from the camera. Distinctive features or markers should be provided for that purpose. The digital image processing method is based on the comparison analysis of two consecutive captured images. The light intensity of predefined specular markers or
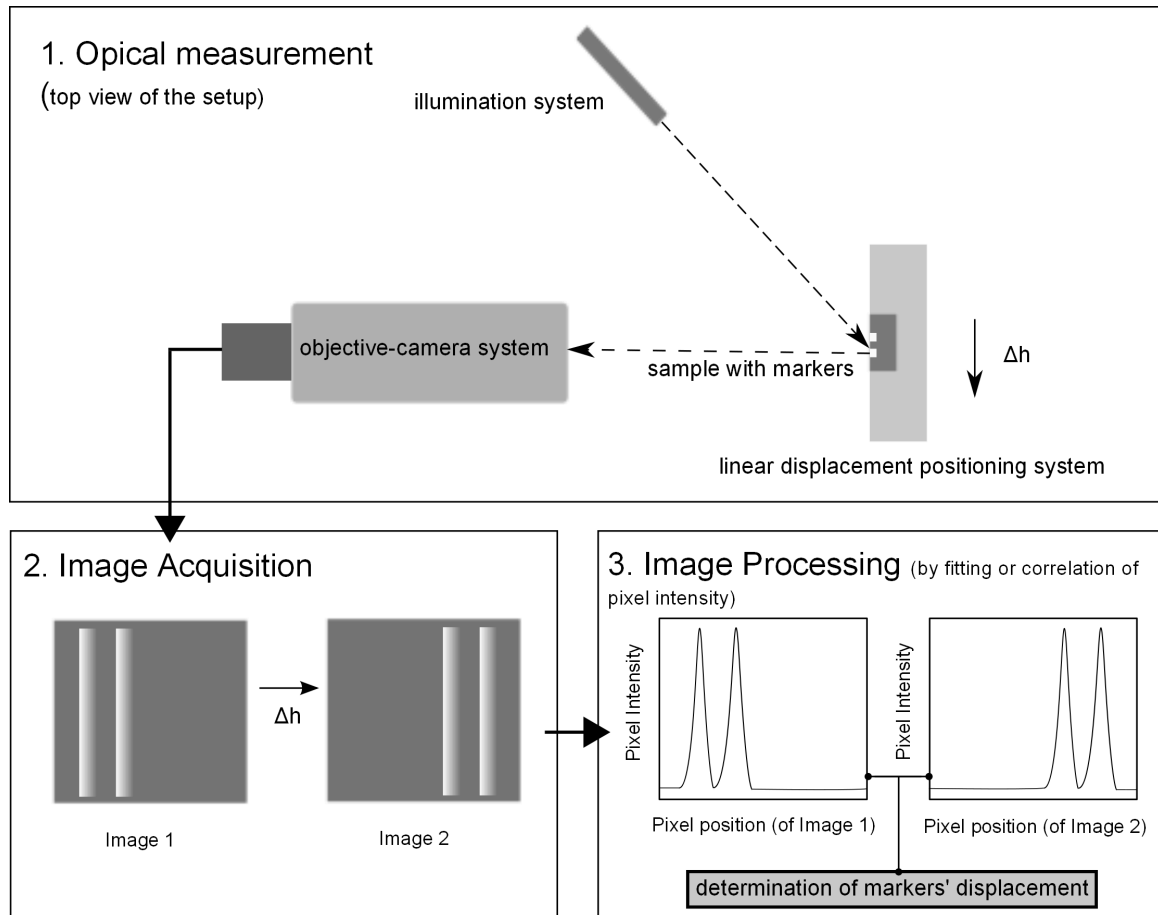
Figure 8.2: Principle of the optical measurement coupled with the selected technique of digital image processing

patterned lines belonging to the object in motion is analysed from the pixels of each captured image, and the positions of the corresponding intensity peaks is determined by means of a cross correlation coefficient in the case of DIC or by a mathematical function fit; a Gauss function is usually selected for the DDIT method because it suits well the distribution shape of light intensity. In the case of the DIC, the pixel gray level values of a subset of pixels corresponding to the area of interest are correlated between two consecutive images. The changes in positions of the brightened pixels is detected by the maximization of a correlation coefficient that allows calculating changes in translations in X and Y directions. In the case of DDIT, the pixel intensity levels of illuminated markers are fitted by a gauss fit function (see Figure 8.2), and the position of the resulting fitted peak can be calculated over the images. At the end, such analysis methods provide a better displacement resolution than the original optical information and are thus particularly appropriate for sub-pixel analyses.

In the present application, the measurement will directly be focused on the area of the moving indenter. In this way the smallest change in indentation depth, also due to thermal expansion occurring in the region of the heated tip, can be detected.

8.3.2   Design of an Optical Setup

The optical setup is designed according to the following four main requirements, relevant for the measurement:

- determination of the working distance (WD)

- determination of the field of view (FOV)

- definition of the required spatial resolution

- definition of the temporal resolution

After determining those requirements, the design setup can be defined by the selection of five different units [115]:

- camera

- lens system

- illumination

- sample (or target in motion)

- software

Other parallel criterions such as the installation space and other characteristics of the environment are to be considered for the setup's design.

8.3.2.1 Determination of the WD

The WD is the first main criterion to fulfil in case of measurement with a high temperature indentation device. Indeed, a gap between the hot testing area and the optical setup is needed to prevent the optical instruments from warming. This gap highly depends here on the radius of the vacuum chamber separating the heated indenter tip to the objective. The radius of the chamber required for such applications is in the range of 150 to 250 mm. Therefore, an average working distance of 220 mm is selected to be convenient for further optical measurements through the window of the vacuum chamber.

8.3.2.2 Determination of the FOV

The FOV is both defined by the maximum size of the target to be studied, and by its maximal variation in displacement. The target here is the diamond tip, or more practically an area close to the tip, directly related to its motion.
In the case of ball indentation, the maximum indentation depth should not exceed the required 25 µm when using a Rockwell tip of 200 µm radius. Nevertheless, Vickers hardness tests performed at loads higher than 50 N can lead to indentation depths larger than 50 µm in the most ductile state of Eurofer97.
Therefore, a minimum displacement variation up to 60 µm is required to be measured from the optical system. Moreover, the procedure concerning the contact detection of the tip on the sample requires the measurement of a previous drive of the tip defined by the initial distance existing between the tip and the sample. A minimum gap of 1 to 2 mm is needed for the observation by the operator situated at ca. 1 m away from the tip outside the Hot Cell. This minimum gap avoids any accidental contact of the tip on the sample before the test has been started. As a result of these considerations, a minimum total FOV of 1.5 mm is needed for the position measurement of the tip.

8.3.2.3   Determination of the Spatial Resolution

The optical spatial resolution is given by:

$$\Delta x = \frac{L_P}{M} \tag{8.1}$$

where L_p is the pixel´s length of the selected camera and M the magnification of the selected objective. The resolution achievable from the optics is mainly limited by these two characteristics. It was previously mentioned that a final displacement resolution between 100 nm and 20 nm is needed. The final displacement resolution required for the measurement differs here from the optical achieved resolution. According to the fact that the programm used for the digital image processing is expected to provide a 1/100 sub-pixel resolution, an optical resolution Δx of 2 µm is adapted for the measurement at the highest resolution of 20 nm. The camera and the objective used for the measurement of the indentation depth have to be selected in order to fulfill the criterion of Δx.

8.3.2.4   Determination of the Temporal Resolution

The displacement-force data rate provided by the Zwick Z2.5 device is of 50 Hz. This temporal resolution helps delivering a well-defined P-h curve. Considering the P-h curve obtained in the case of Eurofer97 for a constant loading rate of 0.5 N/s, an indentation depth rate of ca. 250 nm/s is reached meaning that a displacement data rate from 80 ms to 400 ms is acceptable to get displacement information at resolutions of 20 nm to 100 nm. In the context of the selected optical measurement, the temporal resolution includes:

- the image acquisition time needed by the camera depending on the frame rate per second (fps)

- the data transfer defined by the type of connection between the camera and the processing unit

- the processing time required by the software for the calculation of displacement which is both limited by the analysis program and the CPU.

8.3.3   General Remarks about the Measuring Principle

This measurement technique is sensitive to the testing conditions. Different factors are limiting the quality of the measurement. They result both from the abilities of the measuring units used but also from the environmental testing conditions. The main factors affecting the quality of the measurement have been sorted out as follows.

8.3.3.1   Abilities of the Optical Units

Both properties of the digital camera and the objective are here considered. Cameras' chips are characterized by their resolution giving the number and the size of pixels. The smallest recognisable detail of the picture is defined by the association of the size of the pixel to the magnification of the objective as presented in Equation 8.1 which defines the final resolution of the optical setup. Indeed, a higher quality fitting is

delivered for a larger distribution of illuminated pixels. If an increase of magnification is necessary, this usually implies operating at shorter WD. As a consequence, the FOV is reduced. For that reason, a compromise has to be found between the adequate WD and the FOV according to the requirements of the application. In addition, the size of the moving target has to be chosen considering the properties of the camera and the objective.

The time consumption for the production of displacement data highly depends on the speed characteristics of the camera. In the case of in-situ tests, the loss of information of displacement data results both from the speed characteristic of image acquisition and the speed of image processing, and has a direct impact on the ability to reach a high spatial resolution treatment of data. Cameras based on CMOS technologies are more adapted for the present application due to their ability to acquire images at higher rates than with CCD cameras.

8.3.3.2 Ability of the Image Processing Code

The DIC and DDIT analysis methods were initially developed for post-analyses of tensile specimens' deformations; and the speed of calculation was not a relevant parameter for the test. As it will be shown in the coming displacement analyses, an average speed of $2\,\text{s/image}$ at full resolution (2208×3000 pixels) is required by the post-processing tool and CPU system. The present application needs information of indentation depth during the test for a control of the course of the indenter. Nevertheless, the temporal resolution estimated before in section 8.3.2 between 80 and $400\,\text{ms}$ is not absolutely required to check if the test is running properly but is required for a good quality assessment of material parameters. Therefore, displacement data will be treated with a temporal resolution limited by the image processing for the in-situ indentation test while images will be continuously acquired at a higher speed limited by the characteristics of the camera. In a second step, a most precise post-processing of images should be carried out with the whole quantity of images captured during the test for a better definition of the P-h curve required for the identification of material's parameters.

8.3.3.3 Heating Phenomena

Infrared radiations emanate from the heated indenter and sample. As a consequence, the refractive index of heated air will vary. It is important to minimize such a phenomenon because it can lead to changes in the light intensity received by the sensor of the camera. Additionally, blurred images due to induced charges are generated from the penetration of infrared light in the silicon substrate of the camera's sensor [115]. An effective solution would be to add thermal filters to the objective. Such filters stop the non-expected wavelengths coming from thermal emissions, and permit to separate them from the expected wavelengths reflected at the surface of the tracked object. Furthermore, when exposed for a long period to heat, "hot pixels" can appear on the CCD or CMOS sensor. The rate of charge leakage of such pixels become higher with thermal exposure, the consequence is the change of expected dark points of the picture into bright hot starlike points. Finally, the radiation induced by heating the specimen and indenter generates convective currents near the glass of the chamber. Due to heat loss through the furnace window the temperature outside the chamber

can significantly vary along a quite large distance. This factor finally may lead to distortion of the image, for that reason a fan should be positioned in front of the window outside the chamber to make the temperature more homogenous along the optical path [108].

8.3.3.4   Window of the Vacuum Chamber

The quality of the chosen window for the furnace has to be taken into account for the accuracy of the optical measurement. By using standard glasses, the variation of thickness, surface curvature, and index of refraction of the window can vary relatively to the location on the window's surface. These variations generate image distortion and can be interpreted as real displacements of the object. Earlier investigations [108] concerning the window quality have shown that it has a significant influence on quality of strain measurement and also depends on the test temperature as shown on Figure 8.3.
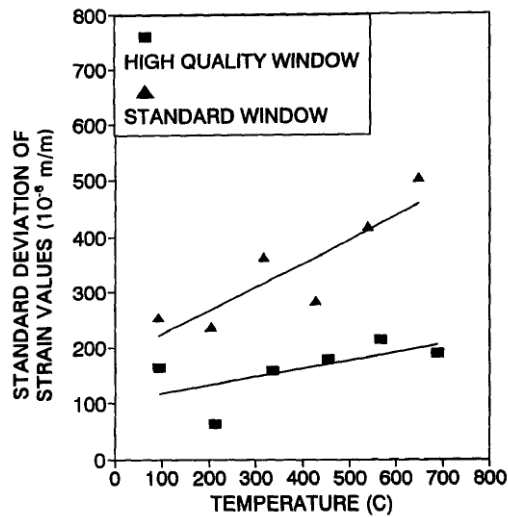
Figure 8.3: Effect of the window quality on the measurement of strain with the digital image processing technique [108]

To minimize such effects, sapphire or quartz windows with high optical quality should be utilised. An adequate choice is proposed in Chapter 9 for the final design of the testing machine. These kinds of glasses have also the advantage to be stable at high temperatures. Another important aspect is the gamma-radiation coming from the irradiated sample, which can alter over time the quality of the glass and darken it as mentioned previously in Chapter 3. Therefore, regular inspections of the glass should be carried out, and direct exposure of irradiated samples should be minimized.

8.3.3.5   Illumination System

The illumination unit plays a relevant role in the interpretation of the image. The intensity must be sufficient enough to distinguish the reflected displacement of markers. Several requirements must be fulfilled in order to measure properly the displacement of markers. The illumination frequency must be higher than the image acquisition rate in order to avoid high changes in illumination of the markers which could lead to errors of measurement. Moreover, the orientation of the illumination system must not

changed during the test, otherwise the selected points will not easily be found for the correlation or tracking calculation. The type of the light source and its orientation in the setup are both important for the best contrast in the image, which can significantly improve the accuracy of the displacement calculation. It makes more sense for the present application to use a monochromatic light with a small wavelength (green or blue), because it delivers a high frequency to get a constant light intensity. Besides that, using a small wavelength for the illumination as well as a corresponding colour filter can significantly minimize the incoming of infrared wavelengths induced by the heated elements, on the chip of the camera. A laser diode illumination is a good compromise between intensity, robustness, lifetime and maintenance, and is particularly adapted for applications with monochromatic light [115].

8.3.3.6 Quality of Markers

The quality of machining and the type of the selected marker influence the accuracy of the measured displacement. In the present case, two types of markers were envisaged:

- a granular speckle surface defining points

- line markers disposed or cut on a surface

- upper edge of the sample

8.4 Displacement Analysis

8.4.1 First Setup

First experiments are carried out at room temperature using the DIC analysis method. this subsection aims at showing how the DIC method can be used for the measurement of a linear displacement of defined markers, it also aims at verifying the influence of some of the test conditions mentioned in the previous section. It will be shown in a first step that the proposed setup does not fit all the requirements of the previous section. According to the identified limitations of the setup, a second setup will be proposed in the following section.

The used markers are corresponding to visible speckles of the surface of a plate made of steel. First experiments are carried out with the DIC analysis method in standard testing conditions: room temperature area, and without any anti-vibration stage. The displacement of speckles belonging to the surface of a steel plate fixed to a positioning system is investigated. The plate was illuminated with a white light source unit. Figure 8.4 exhibits the testing setup.

The setup includes:

- a Pixelink area camera based on a CMOS technology with a pixel size of 3.5 μm and resolution of 2208×3000 pixels

- line markers disposed or cut on a surface

- an objective with a magnification corresponding to 1:1 and delivering an optical resolution of 3.5 μm
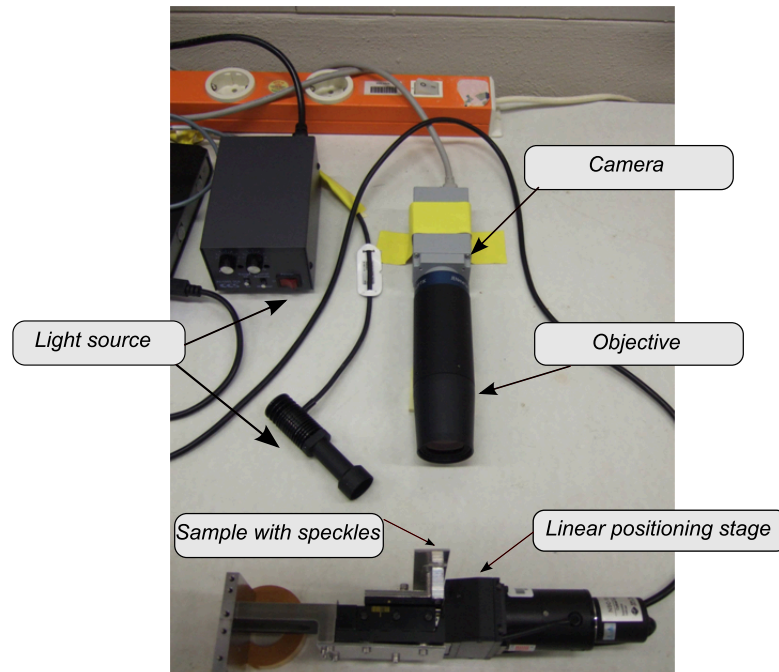
Figure 8.4: First optical setup

- an optical encoder NTS used as positioning system with a travel range of 25 mm, and accuracy at full travel range of 0.03 %

- a sample corresponding to a steel plate characterized by a certain roughness and attached to the positioning system

- an illumination system providing a diffuse white light

- a computer used for the image acquisition and processing.

Series of 18 pictures were taken one after one in a specified illumination condition. A linear motion of 2 µm is applied with the NTS stage, a picture is captured after each displacement. To analyse the importance of the light conditions, a set of photos has been taken by varying the intensity of the light. Two examples are provided in Figure 8.5.

a   b
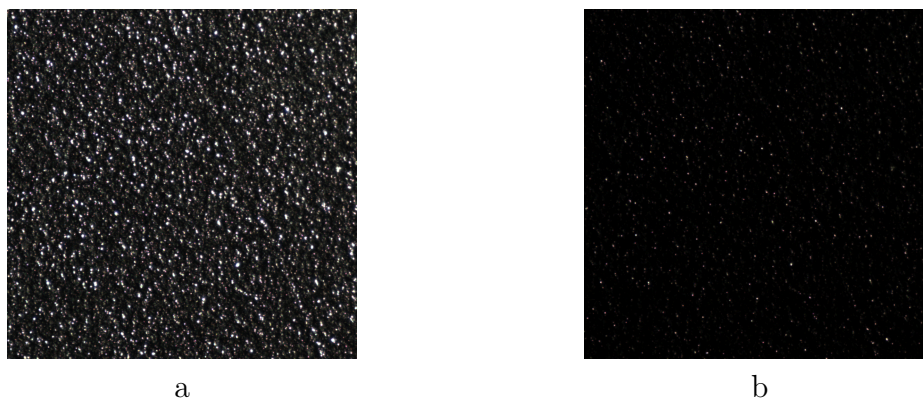
Figure 8.5: Appearance of speckles in different illumination testing conditions, (a) brightened area; (b) non-illuminated area

In the case of granular surface, the influence of the light intensity was found to play a role in the accuracy of the calculated displacement considering that the DIC method requires a high contrast. The results of the most appropriated illumination condition (bright illumination) are presented.

The image processing is carried out in Figure 8.6 showing the linear displacement evolution of specific speckles. An area with a set of X-Y coordinates corresponding to different pixel positions is initially defined as it is visible on the left of the figure. During the image processing, the light intensity of the defined pixels is analyzed over the acquired pictures. After the 18th image, a theoretical displacement of 34 µm has been achieved by the linear stage. According to the fact that the size of the pixel is of 3.5 µm, the theoretical achieved displacement corresponds to a displacement of 9.7 pixels. Figure 8.6 shows that this displacement could be identified for the main defined area which is visible in green, whereas larger and lower displacements have been interpolated for the rest of the area and are identified in red and blue respectively.

a   b
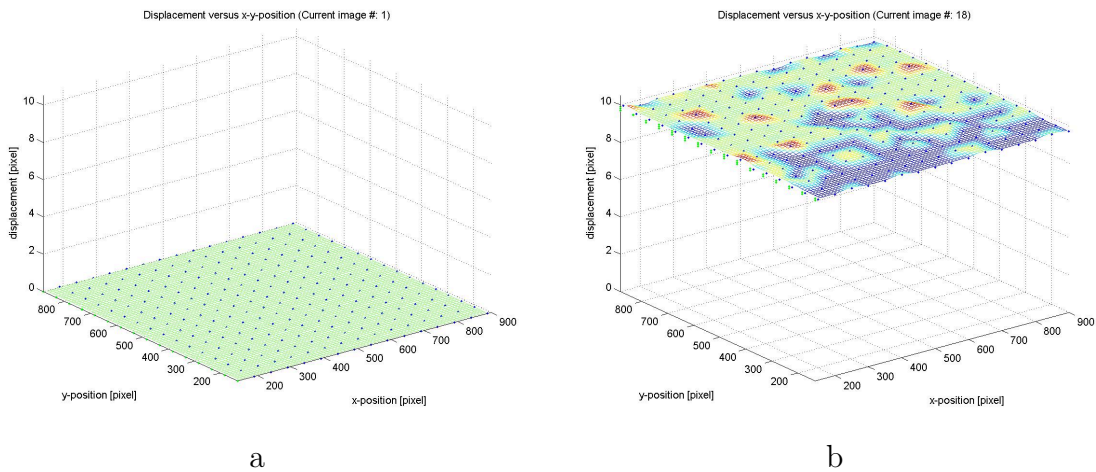
Figure 8.6: Displacement analysis obtained from the DIC method (the displacement corresponds to the x-displacement on the pictures): (a) image nr.1 (displacement=0) (b) image nr.18 (total imposed displacement of 34 µm corresponding to a pixel displacement of 9.7 pixels)

Remarks about the results

A processing time of 2.8 s is required for the analysis of each image acquired at full resolution. The DIC analysis method is able to detect the applied motion of 2 µm displacement resolution. A mean displacement error of 360 nm was found over all processed images and specified speckles leading for these particular testing conditions to an accuracy of the measurement of 18 %. The measured inaccuracy results from diverse factors coming from the testing conditions. For that reason, the accuracy of the DIC analysis method cannot be separated from other external factors influencing the accuracy of the measurement. Factors limiting the accuracy of the measurement are listed as follows:

- Stability: All setup's apparatuses were simply settled on a standard table so that any external vibration was directly transmitted by the table to them. Consequently, the stability in the testing condition was affected. This is thought to be the main reason for explaining the discrepancies found in the measurement.

- Ability of the optical apparatus: The optical resolution with the selected camera-objective system was of 3.5 µm. The criterion regarding Δx and defined in Equation 8.1 is not fulfilled in this study. A way to improve the resolution will be to reduce the real pixel's size, L_p or to increase the magnification M, this should enable to obtain more illuminated pixels at the region of interest and thus improve the quality of the correlation between images.

- Illumination effect: The orientation of the light can be optimised to give a better reflection coming from the object´s surface. Also, a standard diffuse white light was used for this experiment, a better contrast should be obtained when using a illumination system with a single wavelength.

8.4.2   Second Setup
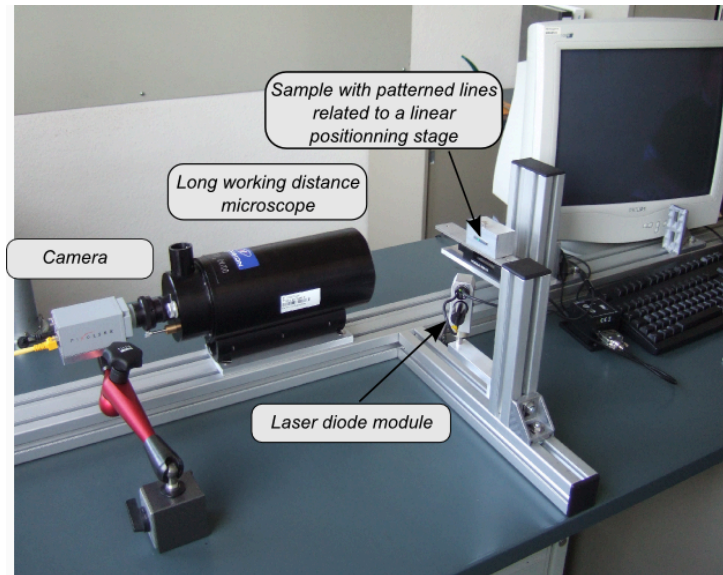
Figure 8.7: Second optical setup

The optical setup is improved according to the requirements relevant for a future adaptation to the high temperature instrument, and considering the measurement limitations encountered with the first setup. The principle motivation of this new setup is to demonstrate that the the selected measuring units as their configuration in the setup are suitable for displacement measurement with the new indentation device. The corresponding setup is illustrated in Figure 8.7 and defined by the following apparatuses:

- a Pixelink PL-B782 area camera based on a CMOS technology with a pixel size L_p of 3.5 µm and resolution of 2208×3000 pixels is selected

- a Questar QM100 long working distance microscope (Maksutov-Cassegrain Cata-dioptric based on the principle of a primary and secondary light reflection mirrors) was selected and can operate at WD situated in the range of 150 to 350 mm. It provides magnifications M from 7.2 to 3.8, and corresponding FOV from

1.9 mm to 2.7 mm combined with the Pixelink camera. Additional magnifications with $\times 3$ magnification Barlow lenses are provided. The ability of magnification of the objective combined with the pixel's length of the selected camera helps fulfill the criterion of Δx.

- a Thorlabs MTS50-Z8 motorized translation stage providing a maximal travel of 50 mm with an accuracy of 0.7 % is initially employed as positioning system of the sample containing the markers. This stage will also be required at the objective for the automation of the focussing functionality. An additional linear positioning PI piezoelectric system is employed in a second step for more accurate displacement analyses.

- a green laser diode (532 nm$\pm$1 nm) from Edmund Optics is selected as monochromatic illumination system. It works at a maximum power of 1 mW with a non-gaussian illumination.

- a Thorlabs optical table is used for displacement analysis with minimized floor vibrations

- a Quad Core CPU computer is selected for higher rate of image processing

- the DDIT analysis method is selected considering its ability to achieve displacement analysis at a higher spatial resolution and higher speed of data processing than in the case of the DIC method

- a ceramic sample (Si_4N_3) is utilized to define line markers, further details about the manufacturing are given in this section.

All optical units are screwed to aluminium guide rails themselves attached to the stage. New types of markers were considered for the second setup. The main idea is to manufacture markers with a most well-defined shape providing a high contrast to the background surface.

Displacements of illuminated patterned lines were considered to be easier and faster to follow from the tracking code, the choice of this shape was also motivated by the fact that such types of markers can be easily controlled by different existing manufacturing processes. Figure 8.8 displays the main adapted manufacturing processes.
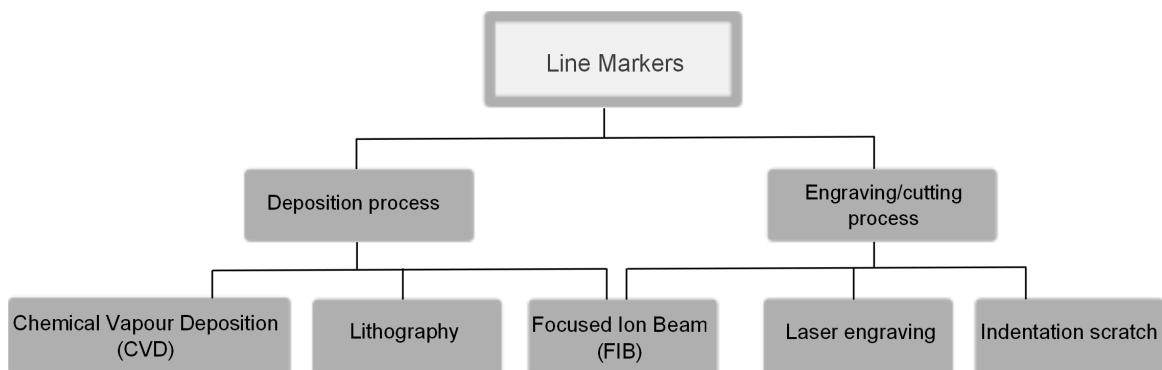
Figure 8.8: Manufacturing processes adapted for patterned line markers

Among the different existing manufacturing processes, the focused ion beam (FIB) technique was tested both for the cases of deposited and engraved markers. The other manufacturing processes could not be tested within the framework of this thesis but are of interest with a view to define more accurate shapes of markers. A platinum marker and cut line with defined dimensions were manufactured on a polished surface of a sample made of Si_4N_3. Such a dark ceramic was selected according to its property of low light's reflectance which finally provides a high contrast of illuminated metallic marker to the background. Additionally, the good thermal properties such as a high melting point at 1900 °C and a low coefficient of thermal expansion of $4 \cdot 10^{-6} \, \mathrm{m/(m \cdot °K}$ at room temperature makes this material particularly adapted for a more accurate measurement at high temperature and for a connection to the indenter holder made of molybdenum, having a similar coefficient of thermal expansion. The polishing of the ceramic was necessary to achieve a good finishing quality of the markers. Pt line markers and engraving marker were manufactured in order to get a length of 100 µm, and width and height or depth of ca. 5 µm. Both types of markers are thought to ensure a contrast in comparison to the substrate. The principle of illumination for both types of markers is illustrated in Figure 8.9. The contrast is expected to be of a different quality when considering the shaded and illuminated areas of the two kinds of markers. The corresponding markers were observed with the long working distance objective with a diffuse white light, a comparison with the selected laser diode illumination is also provided (see Figure 8.10).
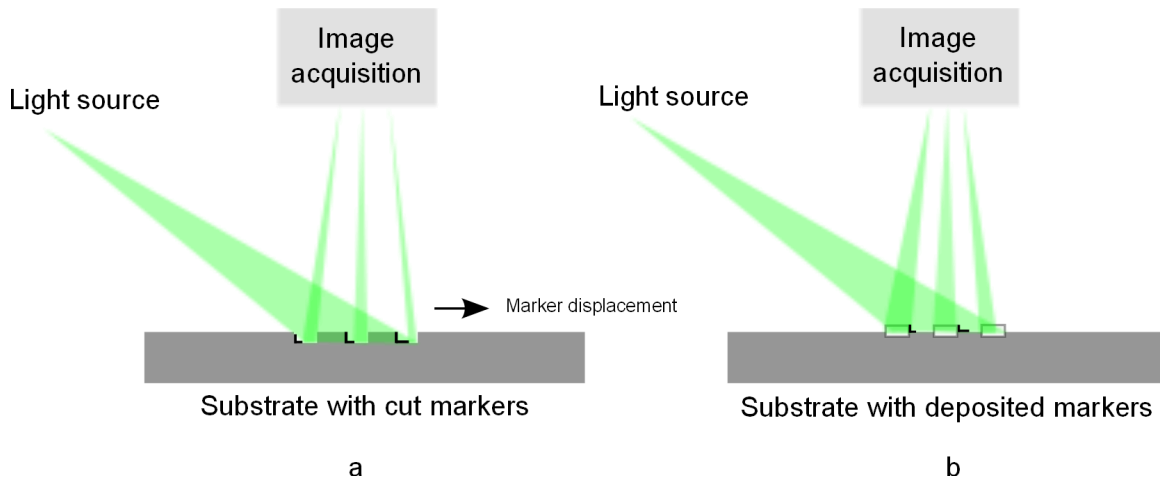
Figure 8.9: Light reflection of cut (a) and deposited markers (b)(dark corners are associated with shaded areas)

8.4.2.1   Analysis of Marker Displacement

The displacement of the markers described above is tested at a WD of 220 mm corresponding to a pixel resolution 0.648 µm for a magnification of 5.4 according to Equation 8.1. The maximal FOV achieved in this testing condition was of 1.94 mm. An orientation of the laser beam varying in the range of 45 to 60 ° was adapted in these testing conditions to achieve an appropriate illumination of the markers.

The extraction of light intensity of the marker to the background is performed by the DDIT method and is visible in Figure 8.11 in the case of two magnifications. The illumination achieved by the laser enhances the reflectivity of markers so that their

<center>a   b</center>
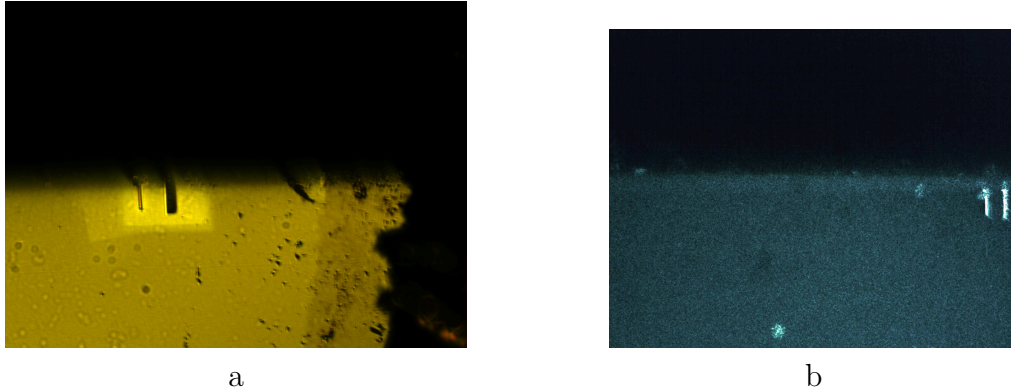
Figure 8.10: Illumination of markers (cut marker on the left and deposited marker on the right) in different illumination conditions: (a) diffuse light; (b) laser green light

corresponding light intensity can be fitted by a Gauss function. The Gauss fittings are represented in Figure 8.11 by red curves for both tested magnifications; this analysis demonstrates that the light intensity of the background is more homogenous and better defined for a higher magnification. Usually, a large uniformly illuminated area is more subjected to slight variations in light intensity than a smaller selected illuminated area. This effect is observed here when comparing two pictures with two levels of magnifications and two resulting fields of view. Generally, a higher magnification will help define a Gauss fit more accurately, when subtracting the background intensity. Discrepancies between the Gauss fitting and the peak resulting from the intensity of all pixels are observed. Different factors might explain the difference observed. The quality of marker's finishing and the presence of interference patterns, visible on the acquired image (b) of Figure 8.11, surrounding the marker and responsible for changes of light intensity at the pixels of interest. A better fitting of the markers could be achieved by changing the the fit function with a function having a shape which adapts more to the shape of the measured peak; and also using techniques of image blurring in order to obtain more brightened pixels surrounding the illuminated marker and thus homogenize the light intensity distribution over the width of the marker.

The displacement of markers was performed with the positioning stage for different step sizes associated here with the displacement resolution: 1 µm, 200 nm, 100 nm (see Figure 8.12) while the optical resolution was maintained to a constant value of 0.648 µm. The error percentage is calculated and averaged over all the applied displacement steps. It lies within 16 %, 38 % and 46 % for the three tested resolutions respectively. It is evident from the analysis that the error becomes more significant with increasing resolution. Floor vibrations are assumed to be at the origin of the increase of inaccuracies. Other series of pictures are additionally performed at less finer resolutions, 2 and 5 µm, in order to investigate if the effect of vibrations plays a less significant role for larger displacement step sizes. Deviations of 16 % and 9 % could be identified when increasing the step size from 2 to 5 µm. According to the fact the accuracy of the linear displacement stage is not thought to change in these test conditions and should remain at a constant value, this last observation seems to lead to the conclusion that the main influencing factor for a decrease of the deviation observed in the displacement measurement is the floor vibration effect. This is confirmed by the analysis of displacement of patterned lines when no displacement is applied to

a   b

c   d
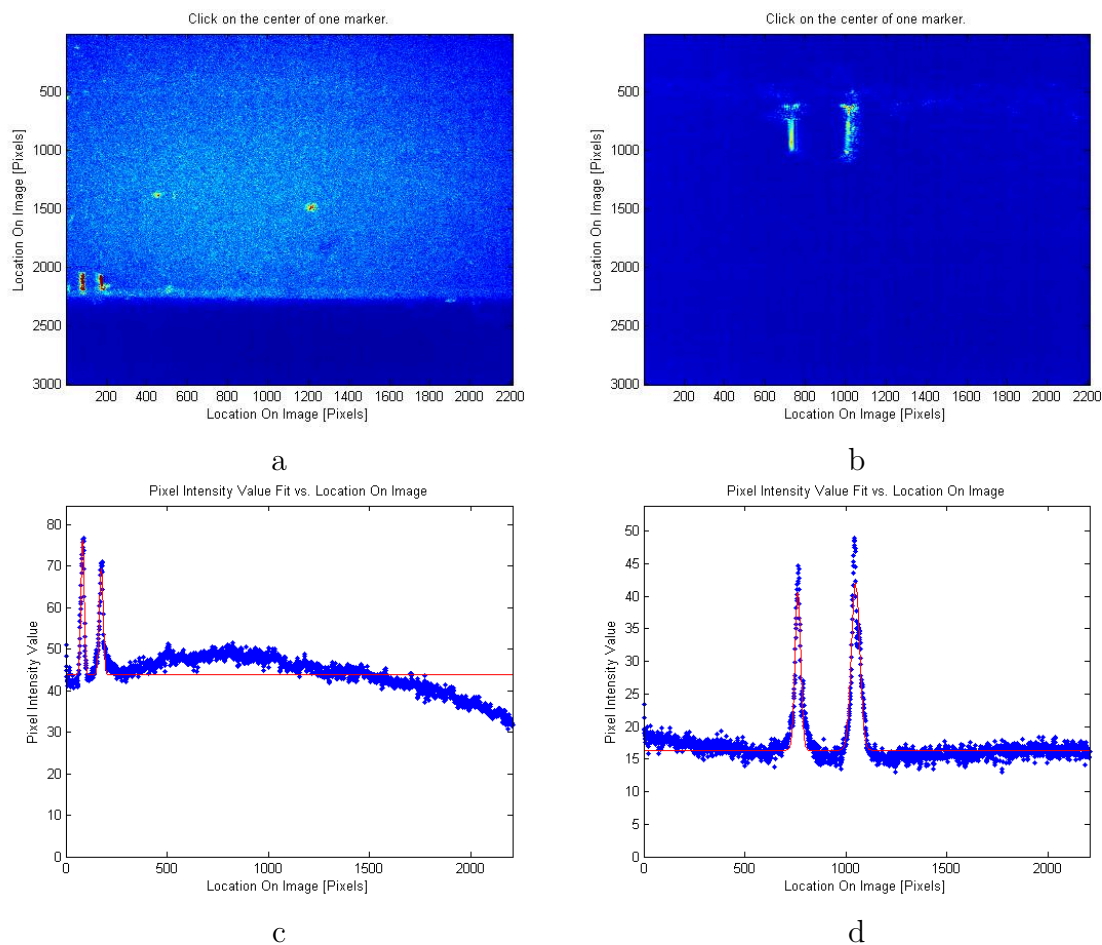
Figure 8.11: Analysis pixel intensity by the DDIT method: (a) Acquired image at ×5.4 magnification (full resolution); (b) Acquired image at ×16.2 magnification (full resolution); (c) Gauss fitting of markers' pixel intensity of image corresponding to image (a); (d) Gauss fitting of markers' pixel intensity of image corresponding to image (b)

the sample by the linear stage. Indeed, it came out that the DDIT method could still identify motions of the patterned lines in the range of 200 nm. Moreover, a difference of accuracy could be distinguished from the two types of markers. The platinum marker was found to give more accurate results according to its better finishing in comparison with the cut line.

8.4.2.2   Speed Study

The ability to detect a linear motion during the course of a target is investigated. The minimal available speed of the linear stage was $3\,\mu\mathrm{m}\cdot\mathrm{s}^{-1}$. The sample containing the markers was driven at that speed, and during the course, pictures were captured at a temporal resolution of 53 ms for a picture resolution of 864×216 adapted to the area of displacement of the markers. According to the temporal resolution of the picture acquisition, a displacement of 159 nm was expected to be detected from the analysis tool. Even at a relatively high displacement rate, the tracking code was already able to identify an average displacement of 175±6 nm per captured image over the total range of acquired images (see Figure 8.13). It can be concluded from this
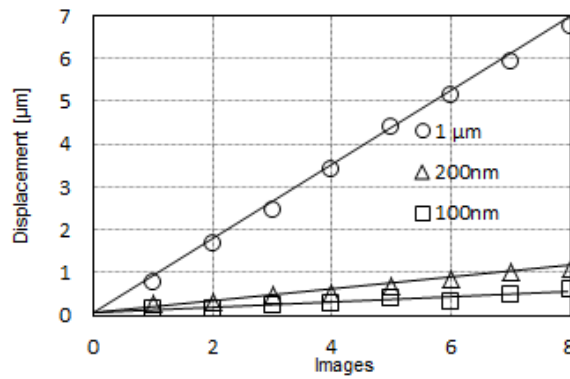
Figure 8.12: Assessment with the DDIT method of displacement for different applied displacement resolutions

study that for lower displacement rates, as it is the case for indentation on RAFM steels (indentation displacement rate of ca.250 nm·s^{-1}, the analysis method is more likely to detect displacement steps with a better accuracy and will be able to capture images corresponding to a motion of less than 20 nm. Moreover, an average image processing time of 5 ms was achieved for the selected picture resolution, meaning that a theoretical total temporal resolution of 58 ms could be achieved in such testing conditions.
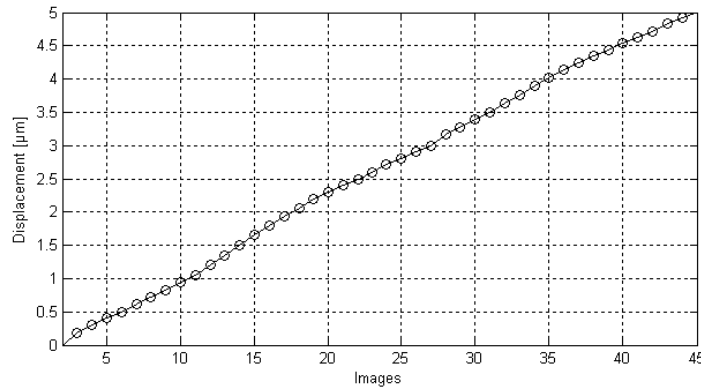
Figure 8.13: Continuous assessment of the markers displacement (displacement rate: 3 μm·s^{-1}, image acquisition rate: 53 ms)

8.4.2.3 Displacement Analysis with an Anti-vibration Stage

A second set of pictures analysis are performed with an anti-vibration stage suitable for isolation from 1 Hz. In this test, a WD of 210 mm is tested instead of 220 mm for reasons of installation, the magnification was therefore 5.8. The DDIT method is applied on the captured images. A better contrast of the markers to the background is obtained as exhibited in Figure 8.14.

Displacement steps of 2 μm, 200 nm, 100 nm and 20 nm, are imposed by a piezoelectric unit, after each displacement applied a waiting period of 1 to 2 s is maintained. The standard deviation is calculated by comparing the theoretical displacement expected, or step size, after each imposed increase of the markers's motion to the displacement calculated by the DDIT method. Image processing was performed by the tracking

code. The assessment of displacement from the tracking code and visible in Figure 8.15 demonstrates that the analysis method is able to identify all the tested resolutions corresponding to sub-pixel resolutions.
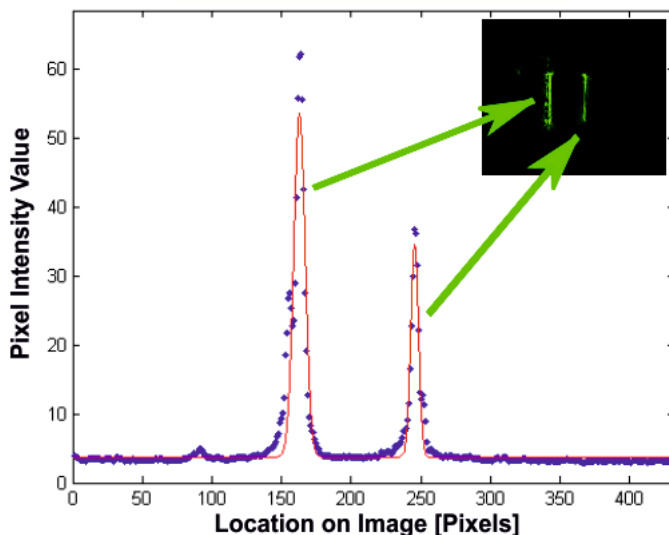
Figure 8.14: Gauss fitting of markers position with the DDIT method use of an anti-vibration stage: Acquired image (on the right corner)

a

b

c

d
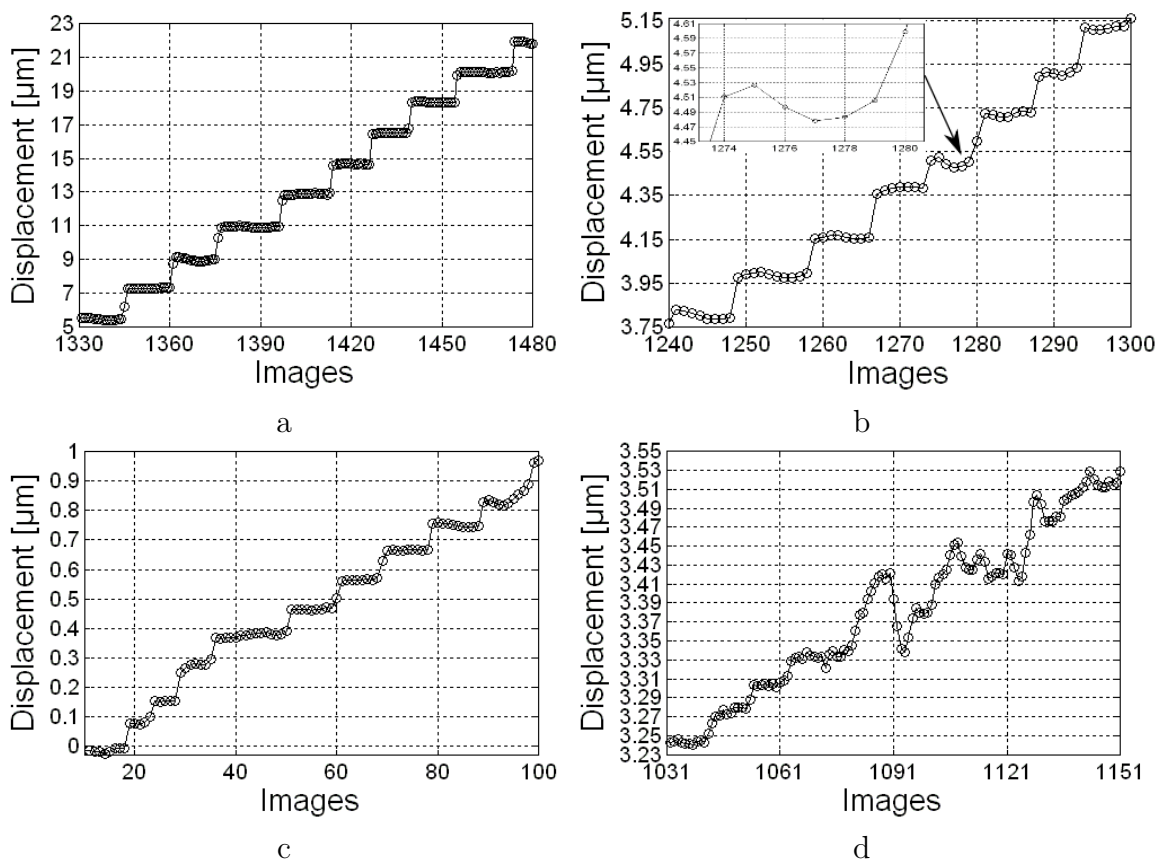
Figure 8.15: Analysis of displacement for different imposed displacement resolutions (use of an anti-vibration stage):(a) 2 µm resolution; (b) 200 nm resolution; (c) 100 nm resolution; (d) 20 nm resolution

The final measurement accuracy over the total imposed travel ranges of the three studied resolutions 2 µm, 200 nm, and 100 nm, lies within a standard deviation of 0.8 and 2.2 %, which has to be considered as a high quality performance with regard to the real total working distance. Indeed, the total optical path run by the light from the sample through the two reflection mirrors of the objective until the chip of the camera corresponds to a distance of ca. 1m.

Nevertheless, oscillations phenomena still are noticeable during expected stable states of the markers. The highest tested resolutions of 20 nm exhibits this phenomenon more pronounced. Oscillations in the range of 20 nm can be identified in all tested conditions. The nanometric accuracy does not explain this observation. It is figured out that the fixation of the laser diode unit to the optical table is unsteady. This is responsible for slight changes in pixels illumination and can therefore explain the observed oscillations at small range.

8.5   Discussion and Further Improvements

It was demonstrated in this chapter that the selected digital image processing method is adapted for displacement measurements at the nanometric scale within the designed setup and testing conditions planned for the high temperature indentation device.

First studies show that vibrations phenomena are most responsible for measurement inaccuracy and could limit the spatial resolution at about 100 nm. Therefore, the use of an anti-vibration stage in the Hot Cell is primordial for accurate measurement at nanometric resolutions down to 20 nm. Additionally, reliable attachments of optical units are essential for high quality measurements in order to minimize the occurrence of any external motions. The image time processing required by the DDIT method could be reduced from 2 s to 50 ms when only selecting the region of interest for the displacement of markers. This finally allows for a higher displacement rate for an in-situ indentation test.

a   b
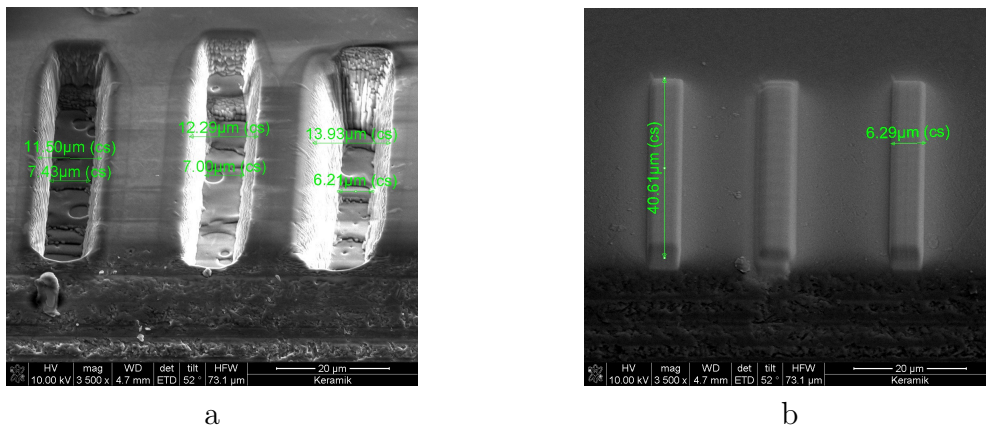
Figure 8.16: Patterned lines from the Focused Ion Beam (FIB) process: (a) engraving; (b) deposited Pt lines

A larger number of patterned lines such as those manufactured by the FIB process and displayed in Figure 8.16 will help to provide more accurate measurements. Markers of width up to 30 µm should also be investigated with a view to perform higher quality fitting. An improvement of such markers is relevant for a use at high temperature. Tungsten is planned to be deposited instead of Platinum regarding its

more interesting thermal properties such as its low thermal coefficient of expansion of $4.5 \cdot 10^{-6}$ m/(m·°C) and its good property of light reflectance as metal. The techniques previously mentioned, lithography, CVD, laser engraving, and indentation scratching are appropriated for finishing of 20 to 30 µm width line markers. It is then of interest to investigate the measurement's quality with such deposited tungsten and cut lines.

Chapter 9

Final Design

This chapter describes the final design of the indentation instrument which is based on the requirements and the concept detailed previously in Chapter 6 to 8. The mechanical layout and manufacturing of the whole device is the result of cooperation between KIT and the two companies Zwick/Roell (Ulm, Germany) [116] and HKE (Walzbachtal, Germany) [117]. The device is featured by two main parts. The load frame, the electromechanical system, the electronic unit and the base plate are delivered by Zwick. The device structures related to the vacuum chamber, the heating/cooling system and the positioning system are delivered by HKE. Remaining components as the indenter are supplied by specialized manufacturers.

9.1   Basic Structure of the Indentation Device

The machine structure used for the high temperature testing device is based on the standard Zwick Z2.5 model which has been utilized for the indentation experiments in this project. The corresponding basic structure is displayed in Figure 9.1. It is mainly composed of the load frame, the base plate, the electromechanical actuator, and the related electronic unit. The whole unit does not exceed a weight of 40 kg.

- The loading frame

The maximal travel of the loading shaft delivered by the Zwick Z2.5 system will not exceed 850 mm. This height ensures the integration of the vacuum chamber as well as the elevation and descend of the loading shaft required for the indentation test (see Figure 9.1). This height is also suitable for an installation in the Hot Cell. Considering that the height of the loading frame was selected to be higher than the currently used Zwick instrument, the whole device´s compliance is thought to exceed the value of 208 nm·N^{-1} corresponding to the frame's compliance of the Zwick Z2.5 model.

- Electromechanical system

The load is applied by means of an electromechanical system. This makes use of a 140 W DC servo-motor itself related to a ball screw spindle that is settled inside the driving traverse. The mobile frame arm is attached to the ball screw spindle and is in charge of carrying the loading shaft to apply the displacement at the indenter. The
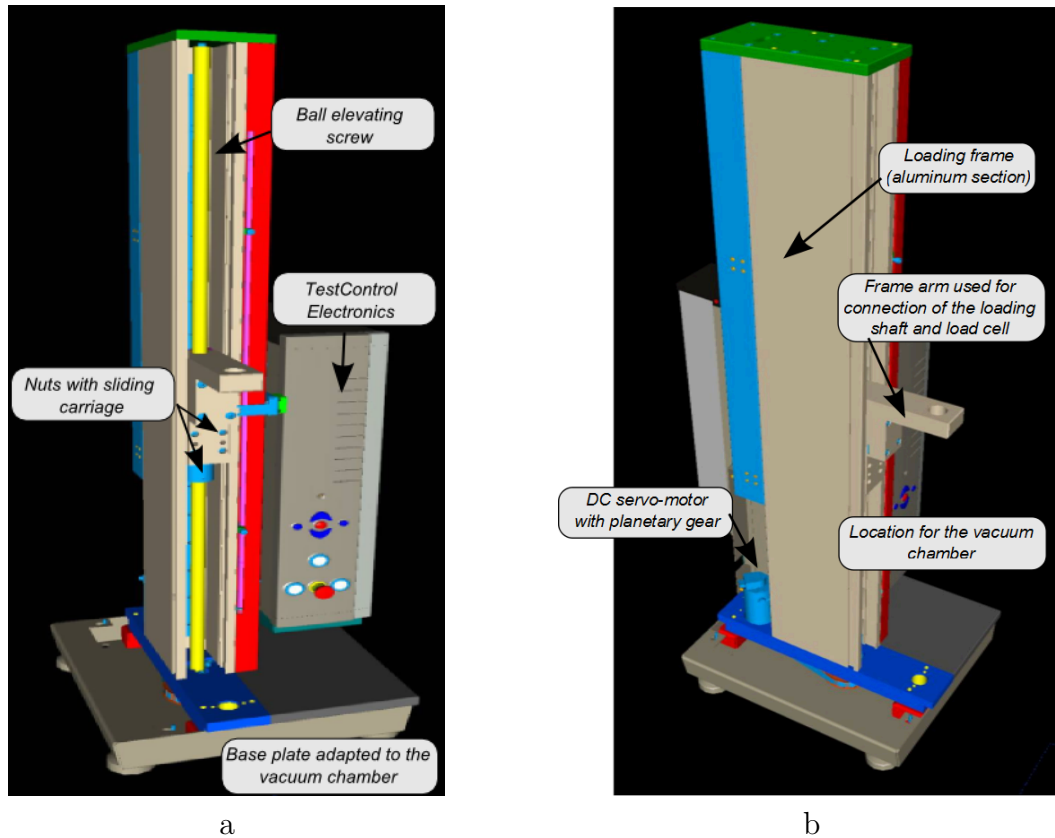
Figure 9.1: Part 1 of the indentation device: two views (a) and (b) of the Zwick Z2.5 basic structure

TestControl Electronic unit of Zwick is integrated in the instrument for measurement and regulation of the force. It also provides the remote control connection with the computer situated outside the Hot Cell.

- Base plate

The base plate is the second part in addition to the frame heigth that has to be adapted in order to serve as basement of the vacuum chamber as it is suggested in Figure 9.1.

9.2   Indentation Part of the Indentation Device

- Rigid Structure

The testing environment of the device, denoted as Part 2 is illustrated in Figure 9.2. It has been designed in order to be adjusted to the basic structure of Part 1. The maximal height from the upper part identified in Figure 9.2 as "connection to the Part 1" does not exceed 800 mm in order to fit the maximal height of the Zwick load frame.

A high quality optical glass of type UV fused Silica (see Appendix C)is fixed to a flange with a view to measure the displacement of the indenter by means of the camera-objective unit. A second flange will be integrated to the vacuum vessel for the connection of the laser diode module (see Appendix C). The dimensioning of the
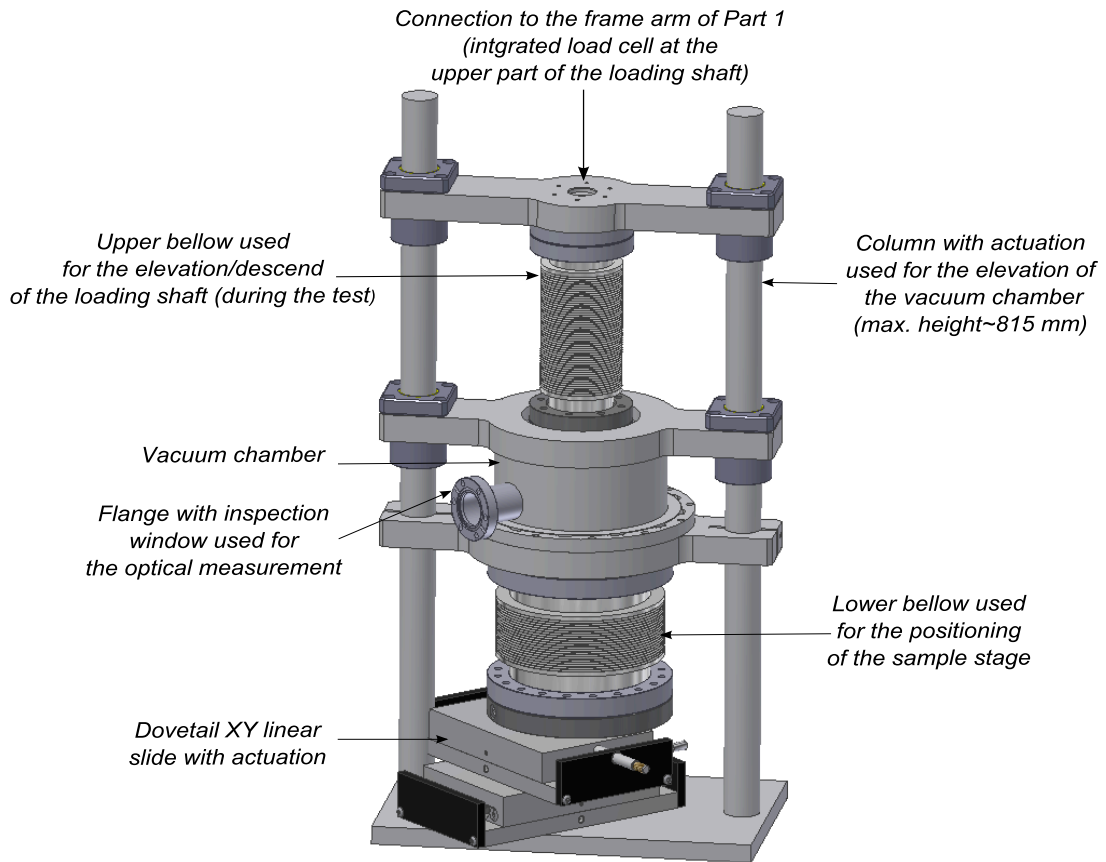
Figure 9.2: Part 2 of the indentation device (testing position): HKE Structure

vacuum chamber is motivated by the two criteria of accessibility with manipulators and maximum working distance required for the optical measuring units. A total distance of 190 mm is defined as maximum distance from the center of the chamber to the inspection window flange (see Figure 9.7). In this concept, the vacuum chamber can be set into two principle positions: the open position or pre-test position for which the internal space of the chamber is totally accessible by the manipulators, and the closed position or testing position for which the chamber is in a gas-tight closed state. In the open state of the chamber, the sample can be positioned with the manipulators on the heating plate and the indenter can be changed if necessary. The two-columns system integrates an actuation that helps the chamber to be translated in a higher position, which is additionally enabled by the compression ability of the upper bellow. Considering the relative high weight of the chamber to be carried, this actuation system has been decoupled from the Zwick load actuation system that is restricted to a load range of 2.5 kN. The closed position of the chamber corresponds to the test position. The upper part of the vacuum chamber is closed by means of bayonet connector and sealed by an O-ring which is integrated on the lower connection part of the chamber. After the chamber has been closed, vacuum and temperature have been applied, the loading shaft is driven by the Zwick loading system. The motion of the

shaft required for the detection of the contact with the sample, as well as loading and unloading during the test, is both enabled by its connection to the frame arm of Part 1 and the ability of compression and extension of the upper bellow. The total volume of the device remaining in a partial vacuum does not exceed 10 l and contains the zone of the chamber as well as the internal space of the upper and lower bellows. According to the volume defined and the needs in high vacuum, a system combining a roots pump to a turbo molecular pump will be connected to the chamber (see Appendix C for characteristics). In addition, the nitrogen filling system existing in the Hot Cell will be used in order to provide an inert gas atmosphere for the remaining gas volume.

- Positioning System

The motorized XY positioning system is based on the connection of two dovetail linear slides [118]. This system has been selected according to its ability to carry relativly high weight structure as it is the case here, in contrast to standard cross-tables which are limited to tens of kilogrammes. The expected final positioning accuracy of the dovetail slides is of 10 µm. This system is situated outside the vacuum chamber for different reasons. Otherwise, the size of the vacuum chamber would have been much larger. As a consequence, the weight of the chamber would have been increased so that elevation becomes critical. Opening from the side of the chamber as an alternative is not possible due to the constraints of remote handling with manipulators.

The sample stage is connected by the cooling block to the cross-table as it is shown in Figure 9.3. Hence, the use of a bellow fixed to the slides by means of a flange is needed both to ensure the sealing of vacuum as well as the motion of the sample by the tension-compression ability of the bellow. CF-flanges use copper gaskets which are particularly adapted for the achievement of high and ultrahigh vacuum seals. According to the specifications of such bellows, the displacement in X and Y directions is limited to 10 mm, which still remains suitable for testing of the standard miniaturized identation samples. Thanks to this configuration, several indentations can be performed by the positioning system after the chamber has been sealed, which gives the opportunity to realize annealing experiments and reduce the total time required for the experiments.

A previous calibration of the sample positioning is particularly relevant and has to be realized in order to define the required translation of the sample for the defined locations of indentation. Such a calibration should be executed at different defined testing temperatures so that the thermal expansion occurring at the heating plate that might influence the position of the sample is considered more accurately. With the aid of an external camera, the inspection after indentation of a reference sample providing a well-defined grid on its surface will help localizing the indents and possibly make calibration positioning corrections to obtain the expected locations of indentation.

- Heating System

The heating system adapted to the indentation instrument is composed of the heating elements corresponding to the cartridge heat resistors, the temperature sensors corresponding to the thermocouples, and a PID type temperature controller. The principle used for heating the tip and the specimen is described in Chapter 7. Three cartridge resistors each of a maximal heating charge of $50\,\mathrm{W\cdot cm^{-2}}$ will be used. One of them is integrated at the indenter holder by a fitted drill, and the two others are

inserted into the sample heating plate (see Figure 7.1 and Figure 7.7). The cables of the cartridges are guided inside the lower machine's bellow, and the connection to the outside is enabled through a lower flange. In order to monitor the temperature applied at the tip and specimen, cartridges with integrated thermocouples are employed. Thermocouples of type K, R and S can measure temperatures up to $1200\,°C$ and $1600\,°C$ for the two last ones, and therefore are suitable for the present application. A measurement accuracy of $1\,°C$ at $650\,°C$ is expected to be achieve by using Pt thermocouples of type R or S [119]. According to the fact that the thermocouples are not set in direct contact to the bodies to be heated, a calibration for different testing temperatures will be carried out to define accurately the regulation of power required to reach the expected temperature both at the sample and the tip. The regulation of the temperature is realized from a PID (proportional-integrative-differential) controller unit (see Appendix C). This is mainly characterized by an accuracy of temperature regulation lying within $\pm\,1\,°C$. Considering that the application of temperature depends on the measured temperature, the total accuracy of the heating system is expected to be of $\pm\,2\,°C$.

- Cooling System
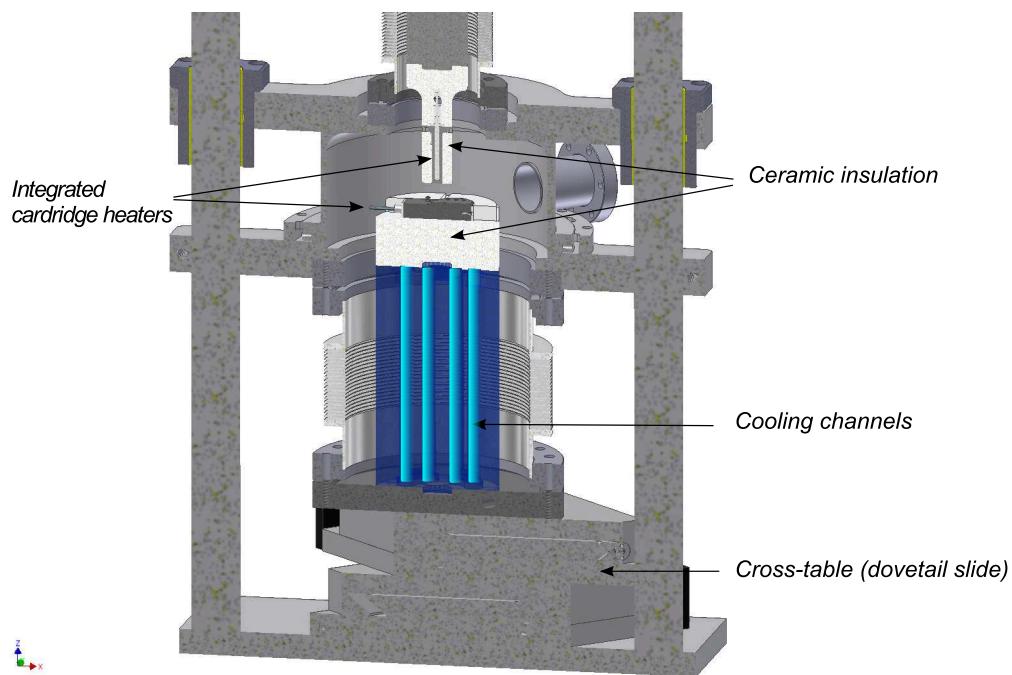
Figure 9.3: Section view of the indentation testing device (Part2)

A water cooling system is used for both cooling of the electronics belonging to the XY positioning and the load cell attached at the top end of the loading shaft. The principle of the selected cooling system used for the positioning unit is illustrated in Figure 9.3. A stainless steel block with integrated cooling-channels is positioned inside the lower machine's bellow, under the ceramic insulation block so that the optimal temperature is reached at the electronics of the cross-table. This block is welded to a CF-flange through which a water connection is available.

- Indenter

The indenter will be manufactured following the design from Synton-Mdp (see Figure 9.4) [120]. Considering that the brazing technique used for the connection between the tip to its holder is unreliable for tests at high temperatures, a mechanical grip mechanism is employed to attach the tip. The cartridge necessary to heat the tip is thus integrated into a drill machined at the holder part. The line markers necessary for the optical measurement are planned to be machined on the lower part of the tip holder made of Si_3N_4. The use of specific glues for applications at high temperatures or adapted brazing is planned to be tested for bonding the markers plate to the indenter holder. Additionally, the attachment of the indenter to the loading shaft is planned to be realized by means of a screw.
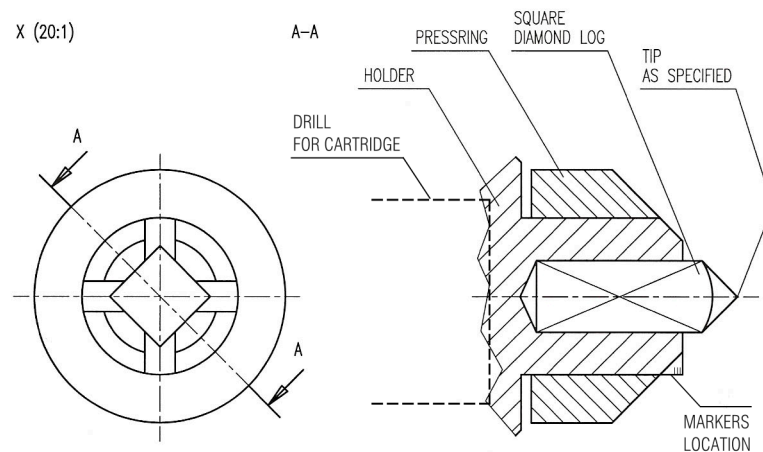
Figure 9.4: Indenter for high temperature testing from Synton-Mdp

• Connection of the two machine's parts

The indenting part (Part 2) manufactured by HKE is connected to the Zwick loading frame (Part 1) as shown in Figure 9.5. This last figure shows schematically the position of the testing device which is conceived for an integration in a Hot Cell having a minimum volume of $1\,m^3$.

9.3   Adaptation of the Depth-Sensing System

An active optical table of type *Halcyonics* or a *HWL* (see Appendix C) is planned to be mounted underneath the whole device in order to isolate the optical measurement from vibrations occurring in the Hot Cell. Such a table has the advantage to be compact enough, only 130 mm height; it remains adapted for carrying the whole indentation machine of ca. 200 kg up to a maximum weight of 600 kg, and isolate the device from 1 Hz (25 dB) vibration frequency. The optical measuring units such as the digital camera, the long-working distance objective and the laser-illumination selected for the device are the same as described in Chapter 8. The optical measurement is enabled through the main flange of the vacuum chamber (see Figure 9.6). A parallel window with high quality optical properties has been selected in order to ensure a high-accuracy optical measurement; characteristics are provided in Appendix C. The size of such glasses is usually limited to a maximal diameter of 63 mm. In such conditions,
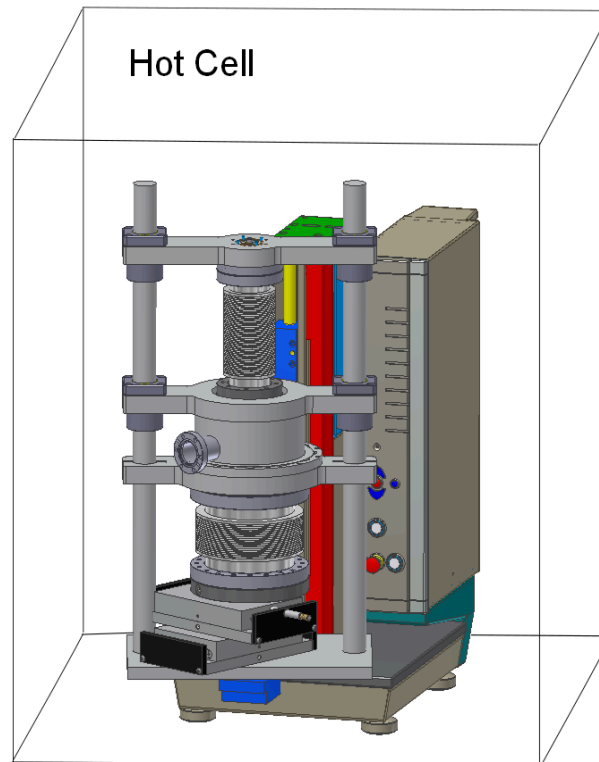
Figure 9.5: Integration of the indentation device in the volume of a Hot Cell

the objective will have to be settled at a maximum working distance of 190 mm from the window flange in order to maintain a measurement field of view of 2 mm available at a total working distance of 230 mm (see Figure 9.7). In this way, a ventilator can be settled in between the inspection window and the objective in order to minimize effects of distortion induced by the heat.

Moreover, the objective will be vertically positioned by means of an integrated lifting table in order to test samples with slight differences in height. Hence, the location of the markers will remain in the field of view of the objective.

9.4   Principle of Operation

The operating principle of the test is schematically summarized in Figure 9.8.

The test is devided into three main phases named: pre-test phase, test-phase and post-test phase. In the pre-test phase, the sample is positioned at first in its holder. Then, the vacuum generation and inert gas filling as well as the heating of the tip and the cartridge are achieved in three different steps. The vacuum chamber should be previously driven in its closed state. The test parameterizing is completed before starting with the actual test-phase. This requires defining the number of cycles, C_t, the corresponding force, F_{cy}, and the initial working distance, LE, to maintain between
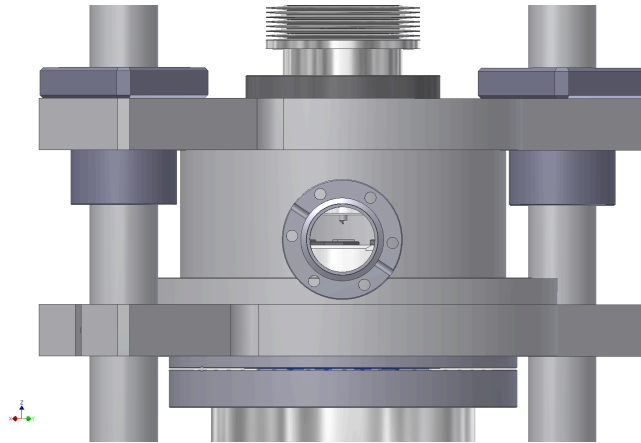
Figure 9.6: View through the chamber for the optical sensing unit
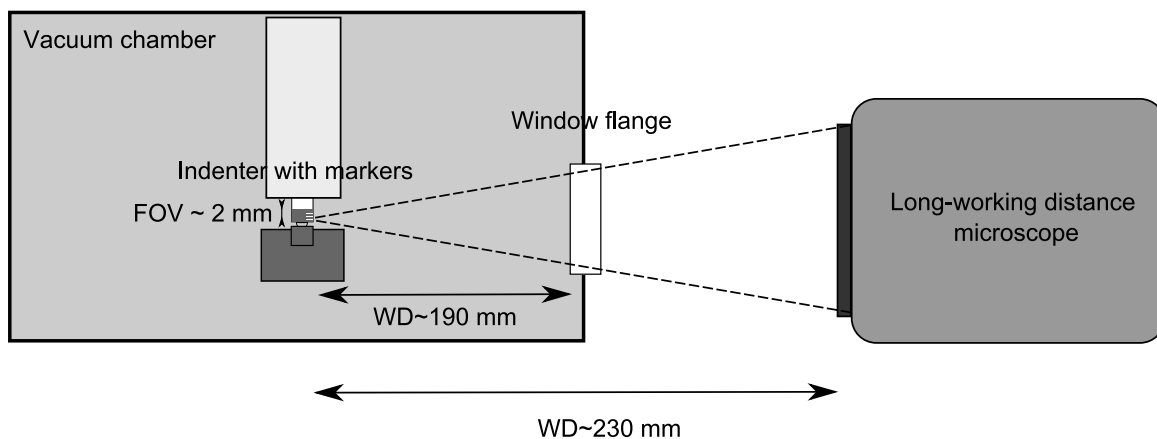
Figure 9.7: Positioning of the long working distance microscope for a measurement of the indenter displacement through the vacuum chamber with a glass diameter of 63 mm

the indenter tip and the sample before the indentation test really starts.

In the test-phase, a slow defined speed is automatically applied at the loading shaft after the indenter has reached the minimum gap LE. The displacement measurement is then achieved by means of the optical units. The contact between the indenter tip and the sample is detected by the load cell when the force reaches a predefined force value, F_c. The real indentation test starts at this moment and follows the defined loading history. When the test is finished, the loading shaft is driven to its original position LE. In this test configuration, the standard software *testXpert* and the electronics *TestControl* of the company Zwick are not adapted to simultaneously monitor the force and the displacement, notably because of constraints existing in the conversion of the electronic signal generated by the camera. An additional module will have to be programmed in order to synchronize the data of force and displacement which are required for the reconstruction of the *P-h* indentation curve. The indentation load remains the signal required to control the course of the test. Hence, the displacement data which will be measured in a separate way during the test can be recombined to the force data afterwards.

The final phase of the test consists of five main steps. After the measurement of force and displacement is ended, the heating is stopped so that the cooling system

can be activated. The vacuum generation is stopped and the filling with inert gas is deactivated in a final step.
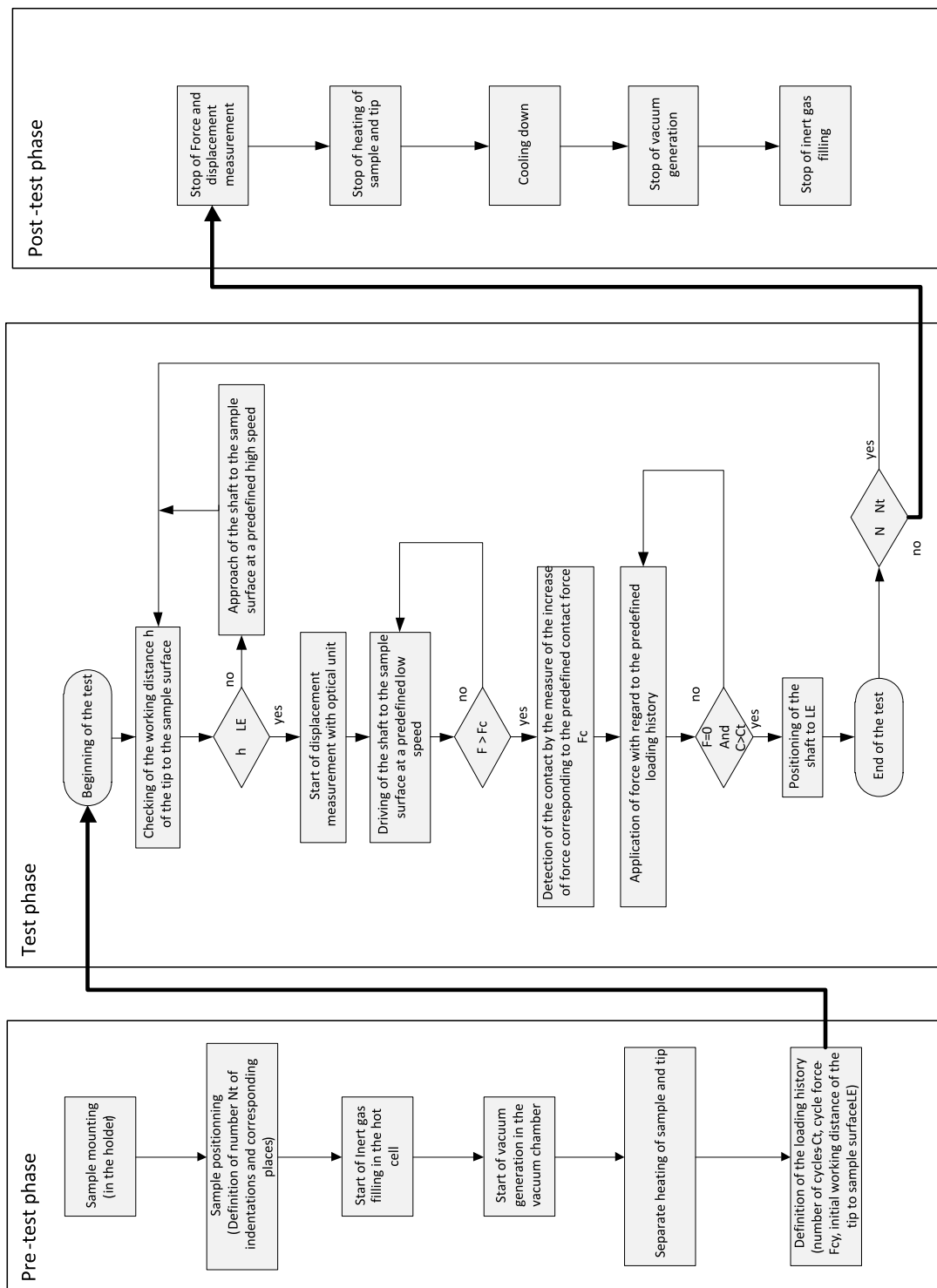
Figure 9.8: Indentation testing procedure

Chapter 10

Conclusion and Outlook

The indentation technique was applied at room temperature to investigate the mechanical behavior of the two irradiated 7-10%-Cr-W steels Eurofer97 and F82H-mod. The main advantage of the applied indentation method resides in its combination with a neural networks-based post-analysis program to identify the mechanical parameters of metallic materials from the experimental P-h indentation curve. As a result, this method provides a more complete characterization of materials than standard hardness tests. In addition, only small irradiated volumes are needed. Halves of broken irradiated miniaturized Charpy specimens were used and tested inside a Hot Cell. The applied indentation method was found to be suited for the characterization of irradiation-induced hardening and strengthening in the studied RAFM steels.

Different sources of uncertainties that are supposed to be responsible for scattering of the experimental indentation curves were additionally examined. It was demonstrated by a finite element analysis that the residual stress remaining after indentation is below 10 MPa at a distance of 1 mm where further indentation shall be made. Such stresses are considered to have an insignificant influence on the slope of the experimental P-h curve. The specimen holder was assumed to play a more significant role for the mechanical behavior measured, since the clamping jaws fix the specimen inhomogeneously and induce a slight elevation, which directly affects the whole system compliance. Therefore, improvements of the holder are suggested for the coming experiments. The residual deformations induced by the Charpy impact on the sample beyond a 3 mm distance from the fracture surface might also have a slight influence on the measured P-h curve. Further investigations will be performed in this direction. Moreover, discrepancies of tensile test and identified indentation strength were observed. Since tensile and indentation experiments make use of two different methods for the material parameters identification, it is generally predictable to encounter some deviations. In addition, the discrepancies observed are mainly considered to be associated with the influence of the test temperature dominating at high irradiation temperatures.

It was demonstrated by additional indentation investigations that an almost complete recovery of the behavior of irradiated material is achieved by annealing in the range of 500 to 550 °C. Such promising repair effects resulting from a post-irradiation heat treatment of the materials and may be applied to components in a future fusion reactor. Thus, the indentation method has been suitable not only for an identification and quantification of radiation damage, but proven to be also for systematic studies of repair techniques on a minimum volume of material.

Since the indentation technique is suited to induce cracks in glass, the brittleness of irradiated steels was investigated. First experiments on highly irradiated material, such as F82H-mod (T_{irr} =300 °C/15 dpa), did not show cracking due to the shape of tip and the maximum machine force.

In a second part, this work focuses on the development of an existing indentation device for characterization of irradiated RAFM steels at temperatures corresponding to their operation temperatures in future fusion reactors. Different phases of the development of a high-temperature indentation device are presented. The requirements in terms of test parameters were studied initially. Based on the criteria specified, the concept of the indentation device was defined. A vacuum chamber is integrated to the indentation system in order to avoid significant oxidation of the sample and the diamond tip, and a heating/cooling system is provided for both the sample and the tip. A new type of sample positioning system, being able to carry the relatively heavy device, is installed. Finally, a contactless measuring technique is applied for monitoring the indenter displacement at high temperatures.

Further studies helped defining functional units for the instrument. Thermal analyses demonstrated that a system based on the power supplied by cartridge heaters is suited to the configurations proposed for the tip and sample. An optical sensing system based on laser illumination of FIB-manufactured line markers was conceived for a long working distance measurement of indentation depth at high temperature. The optical setup is based on the use of image processing by differential digital image tracking technique (DDIT). It was demonstrated that the designed setup is suitable for measuring displacement with sub-micrometer resolution. Accuracy of the measurements will be enhanced by using an anti-vibration stage in order to eliminate significant floor vibrations. The optical measuring setup has the main advantage of being located outside of the testing area and better protected from the heat than transducers positioned near the heated bodies. The final design of the indentation device is a result of a collaboration of the IAM with the two manufacturers of Zwick and HKE. It considers both testing requirements and spatial constraints linked to the dimensions of the Hot Cell.

Further experiments as well as enhancement of the experimental procedure are demanded. Design improvements of the sample holder, taking the results of the numerical simulation into account, are planned for the coming experiments. Fractography analyses are needed to further examine the fracture toughness of irradiated specimens. The surface underneath the indent, where median cracks might also have occurred, is of particular interest. It is expected that indentations on the previous reference steel MANET-II produce more visible cracks, since this material is characterized by a more pronounced embrittlement under the same irradiation conditions.

The mechanical testing device operating at high temperatures will be further developed for the final integration inside the Hot Cell. Before using the instrument in the laboratory, a calibration is required under standard laboratory conditions in order to ensure proper operation. The temperature of the selected heating system needs to be calibrated for different test temperatures defined. According to thermal studies, the choice of the ceramic insulation of the sample heating system limits the temperature reached at the sample. Hence, further modifications of the materials near the sample are envisaged. Instead of Al_2O_3, Zerodur-like ceramics characterized by low coefficients of thermal conductivity are suitable alternatives. As a microscope could

not be provided for the new instrument contrary to the instrument operating at room temperature, prior calibration of indentation locations on the surface of the sample also is of high importance. It will be determined by the position of the specimen carrier relative to the loading shaft. Moreover, the optical test rig requires further developments. The orientation of the illumination source will have to be adapted to the device according to construction constraints. In addition, alternative processes to the FIB-technique, such as laser engraving, CVD and lithography, have to be tested for the manufacturing of line markers, with a view to further improve the reliability and the accuracy of the displacement measurement at high temperatures. This is an essential step to determine which process should be selected for the machining of indenter markers. Analyses performed at high temperature will help determining the influence of the heat at the marker locations in comparison to room temperature measurements, an assessment of thermal drift will be of high importance. The markers' thermal expansion and displacement due to the thermal expansion of the indenter should also be calibrated at different test temperatures defined. Installation of a fan between the inspection window of the chamber and the objective might be a solution to minimize the heat-induced effects responsible for worsening of the image quality.

Finally, comparisons of indentation tests performed at room temperatures and high temperatures will help defining more accurately the impact of the temperature on the change of the mechanical behaviors of irradiated RAFM steels. Test temperatures corresponding to the range of the irradiation temperatures studied in the present report should be considered. It is of high interest to establish to what extend both the temperature and the heating time are responsible for changes of the material strength. This will provide valuable information of how to perform annealing treatments to retrieve the original material properties. The work accomplished in the present report allows the construction of an instrumented indentation facility adapted for further characterization of irradiated materials at high temperatures.

List of Figures

List of Tables

References

[1] J. B. Lister, Y. Martin, C. D. Recherches, E. Polytechnique, F. D. Lausanne, T. Fukuda, R. Yoshino, J. Fusion, V. Mertens, and M.-p. I. Plasmaphysik, "THE CONTROL OF MODERN TOKAMAKS," in *International Conference on Accelerator and Large Experimental Physics Control Systems*, Trieste, Italy, 1999. 1

[2] "ITER." [Online]. Available: http://www.iter.org/. 1

[3] "EFDA," 2010. [Online]. Available: www.efda.org/the_iter_project/index.htm. 1

[4] "DEMO." [Online]. Available: http://fusionforenergy.europa.eu/3_4_demo_en.htm. 1

[5] "Iter-Design." [Online]. Available: http://images.iop.org/objects/phw/news/12/10/10/iter.jpg. 2

[6] A. Lucas, G.E., Odette, G.R., Rowcliffe, "Innovations in Testing Methodology for Fusion Reactor Materials Development," *MRS Bulletin*, vol. 14, no. 7, pp. 29–35, 1989. 2

[7] Materna-morris, E., Möslang, A., Schneider, H.-C., Rolli, R., "FT / P2-2 Microstructure and tensile properties in reduced activation 8-9 % Cr steels at fusion relevant He / dpa ratios , dpa rates and irradiation temperatures," in *Proc. 22nd IAEA Fusion Energy Conference*, 2008, pp. 1–5. 2

[8] N. Baluc, K. Abe, J. Boutard, V. Chernov, E. Diegele, S. Jitsukawa, a. Kimura, R. Klueh, a. Kohyama, R. Kurtz, R. Lässer, H. Matsui, a. Möslang, T. Muroga, G. Odette, M. Tran, B. van der Schaaf, Y. Wu, J. Yu, and S. Zinkle, "Status of R&D activities on materials for fusion power reactors," *Nuclear Fusion*, vol. 47, no. 10, pp. S696–S717, Oct. 2007. [Online]. Available: http://stacks.iop.org/0029-5515/47/i=10/a=S18?key=crossref.393b4860d0f91500162ab49eab547232. 2, 3

[9] F. W. Bloom, E. E., Conn, R. W., Davis, J. W., Golo, R. E., Little, R., Schultz, K. R., Smith, D.L., Wiffen, "Low activation Materials for Fusion Applications," *Journal of Nuclear Materials*, vol. 123, no. I 984, pp. 17–26, 1982. 3

[10] J. Ketema, D.J., Wolters, "SamPle Holder for Irradiation of Miniaturised Steel SpeCimens Simutaneously at Different Temperatures SPICE-T (330-01)," Petten, 2005. 4, 5

[11] H. Lohner, "Sample Holder for Irradiation of Miniaturised Steel Specimens Simutaneously at Different Temperatures SPICE-T (330-01)," Petten, 2005. 4

[12] C. Petersen, J. Aktaa, E. Diegele, E. Gaganidze, R. Lässer, and E. Lucon, "FT / 1-4Ra Mechanical Properties of Reduced Activation Ferritic / Martensitic Steels after European Reactor Irradiations," in *Proc. of 21st IAEA Fusion Energy Conference*, pp. 1–8. 4, 41, 42, 51, 52

[13] E. Gaganidze, H.-C. Schneider, C. Petersen, J. Aktaa, and A. Povstyanko, "FT / P2-1 Mechanical Properties of Reduced Activation Ferritic / Martensitic Steels after High Dose Neutron Irradiation," in *Proc. of 22nd IAEA Fusion Energy Conference*, Geneva, Switzerland, 2008, pp. 1–8. 4, 41, 42, 53

[14] E. Gaganidze, H. Schneider, B. Dafferner, and J. Aktaa, "High-dose neutron irradiation embrittlement of RAFM steels," *Journal of Nuclear Materials*, vol. 355, no. 1-3, pp. 83–88, Sep. 2006. [Online]. Available: http://linkinghub.elsevier.com/retrieve/pii/S0022311506002170. 4

[15] E. Gaganidze, H. Schneider, B. Dafferner, and J. Aktaa, "Embrittlement behavior of neutron irradiated RAFM steels," *Journal of Nuclear Materials*, vol. 367-370, pp. 81–85, Aug. 2007. [Online]. Available: http://linkinghub.elsevier.com/retrieve/pii/S002231150700342X. 4

[16] Rieth, M, Dafferner, B., Röhrig, H.-D., "Charpy impact properties of low activation alloys for fusion applications after neutron irradiation," *Journal of Nuclear Materials*, vol. 233-237, pp. 351–355, Oct. 1996. [Online]. Available: http://linkinghub.elsevier.com/retrieve/pii/S0022311596000943. 4

[17] Rieth, M, Dafferner, B., Röhrig, H.-D., "Embrittlement behaviour of different international low activation alloys after neutron irradiation," *Journal of Nuclear Materials*, vol. 258-263, pp. 1147–1152, Oct. 1998. [Online]. Available: http://linkinghub.elsevier.com/retrieve/pii/S0022311598001718. 4

[18] Schneider, H.-C., Dafferner, Aktaa, J., "Embrittlement behaviour of low-activation alloys with reduced boron content after neutron irradiation," *Journal of Nuclear Materials*, vol. 321, no. 2-3, pp. 135–140, Sep. 2003. [Online]. Available: http://linkinghub.elsevier.com/retrieve/pii/S0022311503002411. 4

[19] N. Huber, "Anwendung Neuronaler Netze bei nichtlinearen Problemen der Mechanik," Habiltationsschrift, Universität Karlsruhe, 2000. 4

[20] E. Tyulyukovskiy, "Identifikation von mechanischen Eigenschaften metallischer Werkstoffe mit dem Eindruckversuch," Scientic Report FZKA 7103 and Dissertation, Universität Karlsruhe, 2005. 4, 30, 31, 61

[21] N. Huber, E. Tyulyukovskiy, H.-C. Schneider, R. Rolli, and M. Weick, "An indentation system for determination of viscoplastic stress – strain behavior of small metal volumes before and after irradiation," *Journal of Nuclear Materials*, vol. 377, pp. 352–358, 2008. 4, 29, 44, 60

[22] S. Scherrer-Rudiy, "Bewertung von Unsicherheiten bei werkstoffmechanischen Fragestellungen mit dem Bayes-Verfahren," Dissertation, Univeristät Karlsruhe, 2008. 4

[23] E. Klötzer, D., Ullner, Ch., Tyulyukovskiy and N. Huber, "Identification of viscoplastic material parameters from spherical indentation data : Part II . Experimental validation of the method," *Journal of Materials Research*, vol. 21, no. 3, pp. 677–684, 2006. 4, 32

[24] M. Klimenkov, E. Materna-Morris, and a. Möslang, "Characterization of radiation induced defects in EUROFER 97 after neutron irradiation," *Journal of Nuclear Materials*, pp. 2010–2012, Jan. 2011. [Online]. Available: http://linkinghub.elsevier.com/retrieve/pii/S0022311510011086. 5

[25] E. Reimann, "Instrumentierter Eindringversuch im Makrobereich - Ergebnisse aus Zyklen steigender Prüfkraft." 5, 26, 27, 81

[26] Schneider, H.-C., Sacksteder, I., Materna-Morris, E., Huber, N., "Determining Tensile Behavior of Irradiated Steel by Instrumented Indentation," in *ICFRM-13*, 2007. 6

[27] O. Kraft and C. A. Volkert, "Mechanical testing of thin films and small structures," *Advanced engineering materials*, vol. 3, no. 3, pp. 99–110. [Online]. Available: http://cat.inist.fr/?aModele=afficheN\&cpsidt=1012233. 10

[28] R. Schwaiger and O. Kraft, "Analyzing the mechanical behavior of thin films using nanoindentation, cantilever microbeam deflection, and finite element modeling," *Journal of materials research*, vol. 19, no. 1, pp. 315–324. [Online]. Available: http://cat.inist.fr/?aModele=afficheN\&cpsidt=15542789. 10

[29] H. Hertz, *Über die Berührung fester elastische Körper und über die Härte (on the Contact of Rigid Elastic Solids and on Hardness)*, verhandlung des vereins zur beförderung des gewerbefleißes ed., Leipzig, 1882. 11, 12

[30] W. Doerner, M F, Nix, "A method for interpreting the data from depth-sensing indentation instruments," *Journal of Materials Research*, vol. 1, no. 4, 1986. 11

[31] G. Oliver, W.C., Pharr, "An improved technique for determining hardness and elastic modulus load and displacement sensing indentation experiments," *Journal of Materials Research*, vol. 7, no. 6, pp. 1565–1583, 1992. 11, 17

[32] I. N. Sneddon, "The relation between load and penetration in the axisymmetric boussinesq problem for a punch of arbitrary profile," *International Engineering Science*, vol. 3, no. 638, pp. 47–57, 1965. 11

[33] D. Tabor, *The Hardness of Metals*, Oxford University Press, Ed. Oxford Classics Series 2000, 1965. 11, 45

[34] A. Fischer-Cripps, *Nanoindentation*, second version ed., Springer, Ed., 2004. 12, 15, 16, 36, 46

[35] M. Huber, "Zur Theorie der Berührung fester elastischer Körper," 1904. 14

[36] C. A. Schuh, C. E. Packard, and A. C. Lund, "Nanoindentation and contact-mode imaging at high temperatures," *Journal of Materials Research*, vol. 21, no. 3, pp. 725–736, 2006. 16, 63

[37] B. N. Lucas and W. C. Oliver, "Indentation power-law creep of high-purity indium," *Metallurgical and Materials Transactions A*, vol. 30, no. 3, pp. 601–610, Mar. 1999. [Online]. Available: http://www.springerlink.com/index/10.1007/s11661-999-0051-7. 17

[38] "Hysitron." [Online]. Available: http://www.hysitron.com/page_attachments/0000/0535/TI_900TriboIndenter_nanomechanical_test_instrument.pdf. 17

[39] "Csm-instruments." [Online]. Available: http://www.csm-instruments.com/de/webfm_send/53. 17

[40] B. D. Beake, S. R. Goodes, and J. F. Smith, "Nanoscale materials testing under industrially relevant conditions: high-temperature nanoindentation testing," *Zeitschrift für Metallkunde*, vol. 94, no. 7, pp. 798–801. [Online]. Available: http://cat.inist.fr/?aModele=afficheN\&cpsidt=15044969. 18

[41] "Lot-oriel," 2007. [Online]. Available: http://www.lot-oriel.com/site/site_down/nt_nanotest_uken.pdf. 18

[42] Fischer-Cripps Laboratories Ptg. Limited. 19, 20

[43] R. Passilly, B., Mévrel, "Microindentation instrumentée de 20 à 900 °C sur matériaux constitutifs de barrières thermiques," *Matériaux & Techniques*, no. 93, pp. 289–300, 2005. 20, 21

[44] B. Passilly, P. Kanoute, F.-H. Leroy, and R. Mévrel, "High temperature instrumented microindentation: applications to thermal barrier coating constituent materials," *Philosophical Magazine*, vol. 86, no. 33-35, pp. 5739–5752, Nov. 2006. [Online]. Available: http://www.informaworld.com/openurl?genre=article\&doi=10.1080/14786430600726731\&magic=crossref||D404A21C5BB053405B1A640AFFD44AE3. 20, 57

[45] W. Nägele, "Die Heißen Zellen des Kernforschungszentrums Karlsruhe." 23

[46] K. Stefanov, T. Tsukamoto, a. Miyamoto, Y. Sugimoto, N. Tamura, K. Abe, T. Nagamine, and T. Aso, "Electron and neutron radiation damage effects on a two-phase CCD," *IEEE Transactions on Nuclear Science*, vol. 47, no. 3, pp. 1280–1291, Jun. 2000. [Online]. Available: http://ieeexplore.ieee.org/lpdocs/epic03/wrapper.htm?arnumber=856466. 23

[47] K. Farah, a. Kovacs, a. Mejri, and H. Benouada, "Effect of post-irradiation thermal treatments on the stability of gamma-irradiated glass dosimeter," *Radiation Physics and Chemistry*, vol. 76, no. 8-9, pp. 1523–1526, Aug. 2007. [Online]. Available: http://linkinghub.elsevier.com/retrieve/pii/S0969806X07001041. 23

[48] L. Holmes-Siedle, A., Adams, *Handbook of radiation effects*, O. U. Press, Ed., 1993. 23

[49] M. Fournier, "Charakterisierung von bestrahlten Materialien für die Kernfusion mit Hilfe des insrtrumentierten Eindrucksversuchs," Diplomarbeit, Forschungszentrum Karlsruhe, 2007. 24

[50] "DIN EN ISO 14577-1:2002, Instrumentierte eindringprüfung zur Bestimmung der Härte und anderer Werkstoffparameter," 2002. 24, 60

[51] "Heidenhain," 2007. [Online]. Available: http://www.heidenhain.de/fileadmin/pdb/media/img/571_470-14.pdf. 26, 81

[52] T. C. Huber, N, "A neural network tool for identifying the material parameters of a finite deformation viscoplasticity model with static recovery," *Computer Methods in Applied Mechanics and Engineering*, vol. 191, no. 31, pp. 353–384, May 2002. [Online]. Available: http://linkinghub.elsevier.com/retrieve/pii/S004578250100278X. 29

[53] C. Tsakmakis, "Methoden zur Darstellung inelastischen Materialverhaltens bei kleinen Deformationen," Habilitationsschrift, Universität Kassel, 1994. 29

[54] H. K. D. H. Bhadeshia, "Neural Networks in Materials Science." *ISIJ International*, vol. 39, no. 10, pp. 966–979, 1999. [Online]. Available: http://joi.jlc.jst.go.jp/JST.Journalarchive/isijinternational1989/39.966?from=CrossRef. 30

[55] Gaganidze, E., Dafferner B., Ries, H., Rolli, R., Schneider, H.-C., Aktaa, J., "Irradiation Programme HFR Phase IIb – SPICE Impact testing on up to 16.3 dpa irradiated RAFM steels Final Report for," Scientific Report FZKA 7371, Forschungszentrum Karlsruhe, 2008. 34, 42, 55

[56] W. Basuki, "Auswertung der durch den HIP-Prozess," Scientific Report, FZKA 7522 and Dissertation, Universität Karlsruhe, 2009. 34

[57] J.-i. Jang, "Estimation of residual stress by instruented indentation: A review," *Journal of Ceramic Processing Research*, vol. 10, no. 3, pp. 391–400, 2009. 35

[58] V. Pfaffenrot, "Numerische Simulation eines Probenhalters mit Berücksichtigung verschiedener Versuchsbedingungen," Diplomarbeit, Forschungszentrum Karlsruhe, 2010. 36

[59] L. Mansur, "Theory and experimental background on dimensional changes in irradiated alloys," *Journal of Nuclear Materials*, vol. 216, no. 1994, pp. 97–123, Oct. 1994. [Online]. Available: http://linkinghub.elsevier.com/retrieve/pii/0022311594900094. 41

[60] P. F. Mueller, "Finite Element Modeling and Experimental Study of Brittle Fracture in Tempered Martensitic Steels for," Ph.D. dissertation, École Polytechnique Fédérale de Lausanne. 41

[61] F. Abe, T. Noda, H. Araki, M. Narui, and H. Kayano, "Irradiation hardening and ductility loss of a low-activation 9Cr-1V ferritic steel at low temperatures," *Journal of Nuclear Materials*, vol. 166, no. 3, pp. 265–277, Aug. 1989. [Online]. Available: http://linkinghub.elsevier.com/retrieve/pii/0022311589902237. 41

[62] E. Materna-Morris, a. Möslang, R. Rolli, and H.-C. Schneider, "Effect of helium on tensile properties and microstructure in 9%Cr–WVTa–steel after neutron irradiation up to 15dpa between 250 and 450°C," *Journal of Nuclear Materials*, vol. 386-388, pp. 422–425, Apr. 2009. [Online]. Available: http://linkinghub.elsevier.com/retrieve/pii/S0022311508008933. 41, 42, 44, 46

[63] E. Materna-Morris, "Structural Material Eurofer97-2, Characterization of Rod and Plate Material: structural, Tensile, Charpy, and Creep Properties," Scientific Report, Interner Bericht 31.40.04, Forschungszentrum Karlsruhe, 2007. 43

[64] Sacksteder, I., Schneider, H.-C. Materna-Morris, E., "Determining Irradiation Damage and Recovery by Instrumented Indentation in RAFM Steel," *Journal of Nuclear Materials*, 2009. 43, 45

[65] Schneider, H.-C., Dafferner, B., Ries, H., Lautensack, S., Romer, O., "Bestrahlungsprogramm HFR Phase Ib Ergebnisse der Kerbschlagbiegeversuche mit den bis 2.4 dpa bestrahlten Werkstoffen," Scienific Report FZKA 6976, Forschungszentrum Karlsruhe, 2004. 45, 55

[66] H.-C. Schneider, "Entwicklung einer miniaturisierten bruchmechanischen Probe für Nachbestrahlungsuntersuchungen," Scientific Report FZKA 7066 and Dissertation, Universität Karlsruhe, 2005. 45, 55

[67] H. A. Francis, "Application of spherical indentation mechanics to reversible and irreversible contact between rough surfaces," *Wear*, vol. 45, pp. 221 – 269, 1977. 46

[68] K. Johnson, *Contacts Mechanics*, C. U. Press, Ed., Cambridge, U.K., 1985. 46

[69] J. T. Busby, M. C. Hash, and G. S. Was, "The relationship between hardness and yield stress in irradiated austenitic and ferritic steels," *Journal of Nuclear Materials*, vol. 336, no. 2-3, pp. 267–278, Feb. 2005. [Online]. Available: http://linkinghub.elsevier.com/retrieve/pii/S0022311504007287. 46

[70] Ryoei Katsura, Yoshihide Ishiyama, Norikatu Yokota, and Takahiko Kato, Nippon Nuclear Fuel Development Co. Ltd.; Kiyotomo Nakata, Hitachi Ltd.; Kouji Fukuya, and Hiroshi Sakamoto, Toshiba Corp.; Kyoichi Asano, "Post-Irradiation Annealing Effect of Austenitic Stainless Steels on IASCC," *CORROSION*, 1998. 51

[71] D. Klueh, R.L., Harries, *High-Chromium Ferritic and Martensitic Steels for Nuclear Applications*, ASTM, Ed., 2001. 51

[72] Sacksteder, I., Schneider, H.-C., "Development of an Instrumented Indentation Device for further Characterization of irradiated Steels at High Temperature," *Journal of Fusion Engineering and Design*, 2010. 53, 79

[73] C. Petersen, V. Shamardin, a. Fedoseev, G. Shimansky, V. Efimov, and J. Rensman, "The ARBOR irradiation project," *Journal of Nuclear Materials*, vol. 307-311, pp. 1655–1659, Dec. 2002. [Online]. Available: http://linkinghub.elsevier.com/retrieve/pii/S0022311502011042. 54

[74] T. Umwelt, H.-C. Schneider, M. Rieth, B. Dafferner, H. Ries, and O. Romer, "Bestrahlungsprogramm MANITU Ergebnisse der Kerbschlagbiegeversuche mit den bis 0,8 dpa bestrahlten Werkstoffen der zweiten Bestrahlungsphase," Scientific Report FZKA 6519, Forschungszentrum Karlsruhe, 2000. 55

[75] R. F. Cook and G. M. Pharr, "Direct Observation and Analysis of Indentation Cracking in Glasses and Ceramics," *Journal of the American Ceramic Society*, vol. 73, no. 4, pp. 787–817, Apr. 1990. [Online]. Available: http://doi.wiley.com/10.1111/j.1151-2916.1990.tb05119.x. 55

[76] T. Fett, "Computation of the crack opening displacements for Vickers indentation cracks," Scientific Report FZKA 6757, Forschungszentrum Karlsruhe, 2002. 55

[77] J. J. Kruzic, D. K. Kim, K. J. Koester, and R. O. Ritchie, "Indentation techniques for evaluating the fracture toughness of biomaterials and hard tissues." *Journal of the mechanical behavior of biomedical materials*, vol. 2, no. 4, pp. 384–95, Aug. 2009. [Online]. Available: http://www.ncbi.nlm.nih.gov/pubmed/19627845. 55

[78] D. Anstis, G.R., Chantikul, P., Lawn B.R., Marshall, "A Critical Evaluation of Indentation Techniques for Measuring Fracture Toughness: I, Direct Crack Measurements," *Journal of the American Ceramic Society*, vol. 46, no. September, pp. 533–538, 1981. 55

[79] E. Gaganidze, "Assessment of Fracture Mechanical Experiments on Irradiated EUROFER97 and F82H Specimens," Scientific Report FZKA 7310, Forschungszentrum Karlsruhe, 2007. 57

[80] N. Baluc, R. Schäublin, P. Spätig, and M. Victoria, "On the potentiality of using ferritic/martensitic steels as structural materials for fusion reactors," *Nuclear Fusion*, vol. 44, no. 1, pp. 56–61, Jan. 2004. [Online]. Available: http://stacks.iop.org/0029-5515/44/i=1/a=006?key=crossref.ed42bd87b8ec5af3a9c54be18f51f270. 63

[81] R. Lindau, a. Moslang, M. Rieth, M. Klimiankou, E. Maternamorris, a. Alamo, a. Tavassoli, C. Cayron, a. Lancha, and P. Fernandez, "Present development status of EUROFER and ODS-EUROFER for application in blanket concepts," *Fusion Engineering and Design*, vol. 75-79, pp. 989–996, Nov. 2005. [Online]. Available: http://linkinghub.elsevier.com/retrieve/pii/S0920379605003534. 63

[82] D. Young, *High temperature oxidation and corrosion of metals*, Elsevier, Ed., 2008. 64

[83] W.-D. Lassner, E., Schubert, *Tungsten*, 1999. 65

[84] C. Evans, T., Phaal, "The Kinetics of the Diamond-Oxygen Reaction," in *Proceedings of the 5th Conference on Carbon*, 1961. 69

[85] J. Field, *The properties of Natural and Synthetic Diamond*, Academic Press, Ed., 1992. 69

[86] J. Wheeler, R. Oliver, and T. Clyne, "AFM observation of diamond indenters after oxidation at elevated temperatures," *Diamond and Related Materials*, vol. 19, no. 11, pp. 1348–1353, Nov. 2010. [Online]. Available: http://linkinghub.elsevier.com/retrieve/pii/S0925963510002591. 70

[87] Q. He, H. Liu, J. Ye, and Q. Niu, "Laser Heat Treatment Analysis of 40Cr Steel for High Speed Spindle," *2009 Symposium on Photonics and Optoelectronics*, pp. 1–4, Aug. 2009. [Online]. Available: http://ieeexplore.ieee.org/lpdocs/epic03/wrapper.htm?arnumber=5230285. 71

[88] J.-H. Lee, J.-H. Jang, B.-D. Joo, Y.-M. Son, and Y.-H. Moon, "Laser surface hardening of AISI H13 tool steel," *Transactions of Nonferrous Metals Society of China*, vol. 19, no. 4, pp. 917–920, Aug. 2009. [Online]. Available: http://linkinghub.elsevier.com/retrieve/pii/S1003632608603775. 71

[89] D. M. Gureev, Y. M. Matveev, S. I. Mednikov, V. K. Shukhostanov, S. V. Yamshchikov, and a. E. Zaikin, "The use of a continuous-wave CO2 laser for hardening of wear-resistant high-chromium cast iron," *Journal of Russian Laser Research*, vol. 17, no. 6, pp. 607–622, Nov. 1996. [Online]. Available: http://www.springerlink.com/index/10.1007/BF02069176. 71

[90] N. Dogan Baydogan and a. B. Tugrul, "Evaluation of the optical changes for a soda-lime-silicate glass exposed to radiation," *Glass Physics and Chemistry*, vol. 32, no. 3, pp. 309–314, May 2006. [Online]. Available: http://www.springerlink.com/index/10.1134/S1087659606030096. 72

[91] "Watlow." [Online]. Available: http://www.watlow.com/products/heaters/ht_cart.cfm. 72, 73

[92] "Ansys Inc., Ansys Release 12.0 Manual." 72

[93] "Ansys Inc., Ansys Release 12.0 Simulation Help." 72

[94] F. Teufel, "Finite-Elemente- Simulation von Bauteilen einer Eindringprüfanlage," Studienarbeit, Forschungszentrum Karlsruhe, 2008. 72

[95] T. Munz, D., Fett, *Mechanisches Verhalten Keramischer Werkstoffe*, WFT Werkstoff-Forschung Und Technik 8, Ed. Springer-Verlag, 1989. 73

[96] D. P. D. Frank Incropera, P., *Fundamentals of Heat and Mass Transfer*, second edi ed., John Wiley & Sons, Ed., 2001. 74

[97] I. Benko, "Improvement of IR-emissivity of ceramic fibre by silicon carbide coating in furnaces," *Energy*, pp. 1–2. 75

[98] D. Nyce, *Linear Position Sensors, Theory and Application*, Wiley, Ed., 2004. 82

[99] "Aos-fiber." [Online]. Available: http://www.aos-fiber.com/eng/Sensors/Sensoren.html. 82

[100] "Micro-epsilon." [Online]. Available: http://www.micro-epsilon.de/products/displacement-position-sensors/capacitive-sensor/index.html. 82

[101] "Hbm." [Online]. Available: http://www.hbm.com/de/menu/produkte/aufnehmer-sensoren/weg/. 82

[102] "Capacitec." [Online]. Available: http://www.capacitec.com/index.cfm?pg=31. 82

[103] "Zygo." [Online]. Available: http://www.zygo.com/?/met/interferometers/. 82

[104] "Keyence." [Online]. Available: http://www.keyence.de/. 82

[105] P. Aswendt, "Speckle interferometry for materials testing under extreme thermal conditions," *Measurement*, vol. 23, no. 4, pp. 205–213, Jun. 1998. [Online]. Available: http://linkinghub.elsevier.com/retrieve/pii/S0263224198000177. 84

[106] M. Bretheau, T., Crépin, J., Doumalin, P., Bornet, "La microextensométrie: un outil de la mécanique des matériaux," *La Revue Métallurgie-CIT/Science et Génie des Matériaux*, 2003. 84

[107] B. Manser, H., Weiss, H., Zagar, "High resolution electronic speckle pattern phtography for strain measurement at high temperatures," in *IMEKO TC7, Int. Symp. on AIMAC91*, Kyoto, 1991. 84

[108] J. S. Lyons, J. Liu, and M. a. Sutton, "High-temperature deformation measurements using digital-image correlation," *Experimental Mechanics*, vol. 36, no. 1, pp. 64–70, Mar. 1996. [Online]. Available: http://www.springerlink.com/index/10.1007/BF02328699. 85, 90

[109] N. Sabaté, D. Vogel, a. Gollhardt, J. Marcos, I. Gràcia, C. Cané, and B. Michel, "Digital image correlation of nanoscale deformation fields for local stress measurement in thin films," *Nanotechnology*, vol. 17, no. 20, pp. 5264–5270, Oct. 2006. [Online]. Available: http://stacks.iop.org/0957-4484/17/i=20/a=037?key=crossref.db022182936fbee57c5da286f1ee4779. 85

[110] R. J. Thompson and K. J. Hemker, "Thermal Expansion Measurements on Coating Materials by Digital Image Correlation," in *Conference: 2007 2007 SEM Annual Conference & Exposition on Experimental and Applied Mechanics*. 85

[111] Eberl C., Thompson R., Gianola D., Sharpe Jr. W. and H. K., "mathworks," 2006. [Online]. Available: http://www.mathworks.com/matlabcentral/fileexchange. 85

[112] D. S. Gianola, "DEFORMATION MECHANISMS IN NANOCRYSTALLINE ALUMINUM THIN FILMS : AN EXPERIMENTAL INVESTIGATION," no. January, 2007. 85

[113] W. N. Sharpe, J. Pulskamp, D. S. Gianola, C. Eberl, R. G. Polcawich, and R. J. Thompson, "Strain Measurements of Silicon Dioxide Microspecimens by Digital Imaging Processing," *Experimental Mechanics*, vol. 47, no. 5, pp. 649–658, Feb. 2007. [Online]. Available: http://www.springerlink.com/index/10.1007/s11340-006-9010-z. 85

[114] W. N. Sharpe, "Mechanical property measurement at the micro/nano scale," Invited Paper, Johns Hopkins University. 85

[115] A. Hornberg, *Handbook of Machine Vision.* Wiley-VHC, 2006. 87, 89, 91

[116] "Zwick." [Online]. Available: http://www.zwick.de/. 103

[117] "Hke." [Online]. Available: http://www.hke-gmbh.com/. 103

[118] "Ero-fuehrungen." [Online]. Available: http://www.ero-fuehrungen.de. 106

[119] M. Weber, D., Nan, *Elektrische Temperaturmessung mit Thermoelementen und Widerstandsthermometern*, Jum, Ed. 107

[120] "Synton-mdp." [Online]. Available: http://www.synton-mdp.ch/. 108

Appendix A

Appendix: Material's Information

A.1 Chemical Composition of Tested Materials

Table A.1: Chemical composition of tested irradiated materials in wt%

Material	Eurofer97	F82H-mod
Heat	83697	9741
Cr	8.91	7.7
W	1.08	2.04
Mn	0.48	0.16
V	0.2	0.16
Ta	0.14	0.009
C	0.12	0.09
Si	0.04	0.11
P	0.005	0.002
S	0.004	0.002
Ni	0.02	0.021
Mo	<0.001	0.003
Nb	0.0017	0.0101
Al	0.009	0.0016
B	0.001	0.0004
N	0.02	0.008
O	0.0008	-
Co	0.006	0.0037
Cu	0.0015	0.0063
Zr	<0.005	0.0063
Ti	0.006	0.004
As	<0.005	-
Sb	<0.005	-
Sn	<0.005	-
Fe	balance	balance

A.2 Extrapolation of indentation data for high temperatures

Table A.2: Values used for the assessment of the second degree polynomial and the extrapolation of indentation data at high temperatures, tensile data are used here and were obtained samples made of Eurofer97 (unirradiated state; original heat treatment: 980°C+760°C)

T [°C]	rel. T [°C] =(T-T0)/T0	T [°K]	rel. T [°K] =(T-T0)/T0	$R_{p0.2}$ [N/mm^2]	rel. $R_{p0.2}$ [R/R0]
20	0.0	293	0.00	568	1.00
300	14.0	573	0.96	479	0.843
400	19.0	673	1.30	453	0.798
500	24.0	773	1.64	404	0.711

A.3 Experimental Data from Indentation Tests

Table A.3: $R_{p0.2}$ identified from indentation tests in MPa

Irradiation temperature	Eurofer97 Anl	Eurofer97 WB	F82H-mod
unirr.	550	460	503
250	854	853	-
300	942	-	800
350	672	657	-
400	584	-	538
450	562	540	-

Table A.4: Standard deviation for $R_{p0.2}$ identified from indentation tests in %

Irradiation temperature	Eurofer97 Anl	Eurofer97 WB	F82H-mod
unirr.	13	15	32
250	34	13	-
300	39	-	61
350		41	-
400	28	-	22
450	60	30	-

Table A.5: Standard deviation for $R_{p0.2}$ identified from indentation tests in comparison to corresponding tensile values in %

Irradiation temperature	Eurofer97 Anl	Eurofer97 WB	F82H-mod
unirr.	2.4	3.6	8.7
250	2.3	7.4	-
300	1.6	-	2.8
350	0.15	3.4	-
400	21.7	-	21.2
450	35.8	48.8	-

Table A.6: H_v measured by indentation tests in kgf·mm^{-2}

Irradiation temperature	Eurofer97 Anl	Eurofer97 WB	F82H-mod
unirr.	222	198	213
250	306	298	-
300	317	-	320
350	252	234	-
400	227	-	213
450	221	205	-

Table A.7: Standard deviation for H_v measured by indentation tests in %

Irradiation temperature	Eurofer97 Anl	Eurofer97 WB	F82H-mod
unirr.	1.5	-	2.9
250	4.6	0.8	-
300	1.5	-	-
350	2.1	2.8	-
400	0.6	-	2.3
450	2	2.4	-

Table A.8: Standard deviation for $R_{p0.2}$ identified from indentation tests in MPa (after post-irradiation annealing, irradiation condition: T_{irr}=250°C, 15 dpa)

	annealing 500°C/1 h	annealing 500°C/3 h	annealing 550°C/20 min	annealing 550°C/1 h	annealing 550°C/3 h
Eurofer97 Anl	870	-	636	604	516
Eurofer97 Anl	698	643	608	590	497

Table A.9: Standard deviation for $R_{p0.2}$ identified by indentation tests in % (after post-irradiation annealing, irradiation condition: T_{irr}=250°C, 15 dpa)

	annealing 500°C/1 h	annealing 500°C/3 h	annealing 550°C/20 min	annealing 550°C/1 h	annealing 550°C/3 h
Eurofer97 Anl	-	-	5.2	3.1	5.4
Eurofer97 Anl	-	3.9	12.2	5.8	7.2

Table A.10: H_v measured by indentation tests in kgf·mm^{-2} (after post-irradiation annealing, irradiation condition: T_{irr}=250°C, 15 dpa)

	annealing 500°C/1 h	annealing 500°C/3 h	annealing 550°C/20 min	annealing 550°C/1 h	annealing 550°C/3 h
Eurofer97 Anl	292	247	236	227	229
Eurofer97 Anl	256	247	226	208	205

Table A.11: Standard deviation for H_v identified by indentation tests in % (after post-irradiation annealing, irradiation condition: T_{irr}=250°C, 15 dpa)

	annealing 500°C/1 h	annealing 500°C/3 h	annealing 550°C/20 min	annealing 550°C/1 h	annealing 550°C/3 h
Eurofer97 Anl	2	2	2	1	2
Eurofer97 Anl	-	2	4	1	1

Appendix B

Appendix: Numerical Simulation

B.1 Simulation of indentation
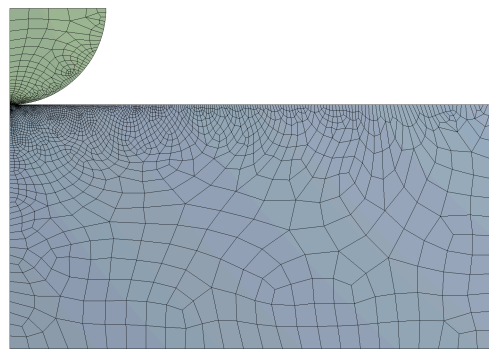
Figure B.1: 2D-Model indentation
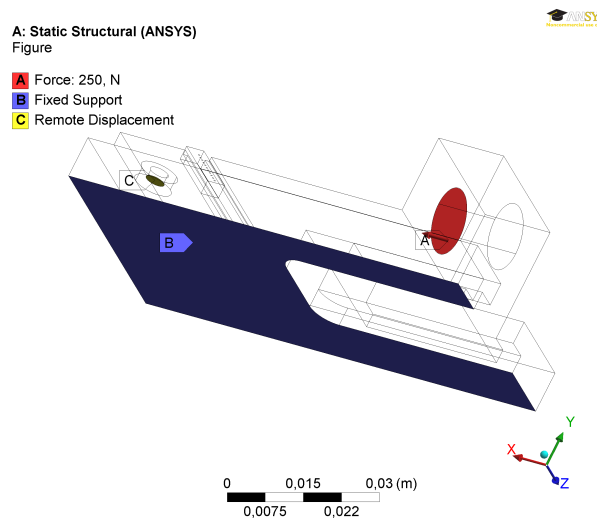
Figure B.2: 3D-Model of the sample holder and boundary conditions

B.2 Heating of the tip-loading shaft system
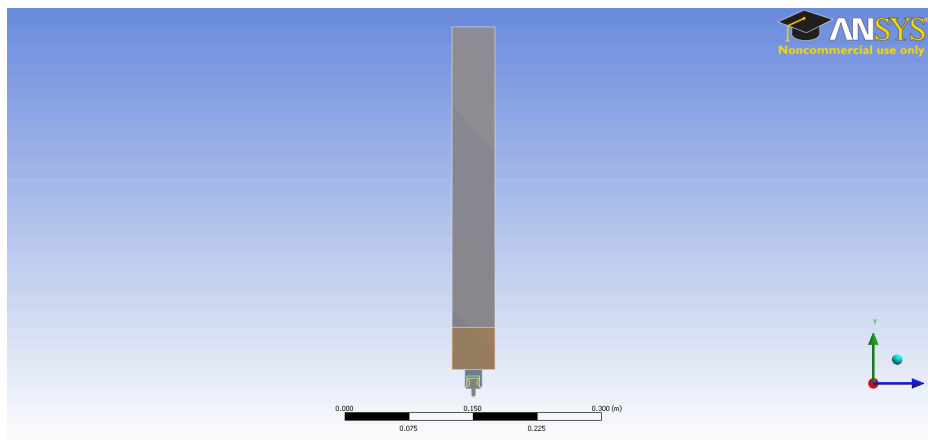
Figure B.3: Configuration of the first selected loading-shaft model
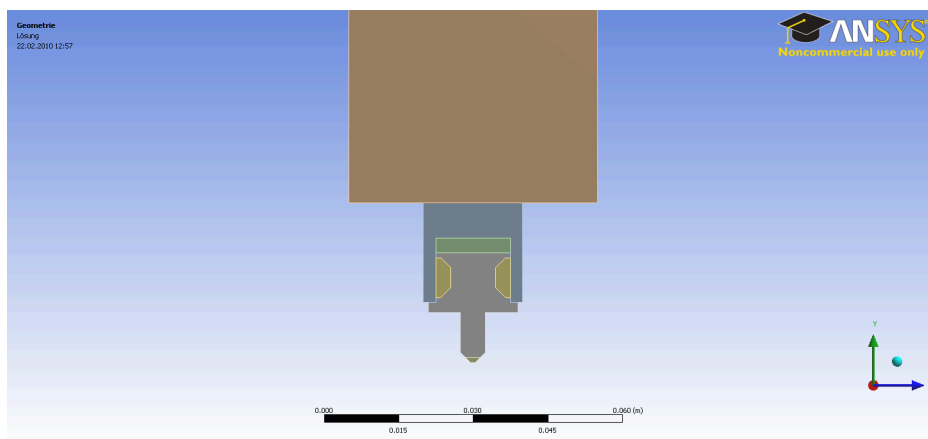
Figure B.4: First studied configuration of the tip-holder with the integrated heating plate resistor situated over the indenter holder
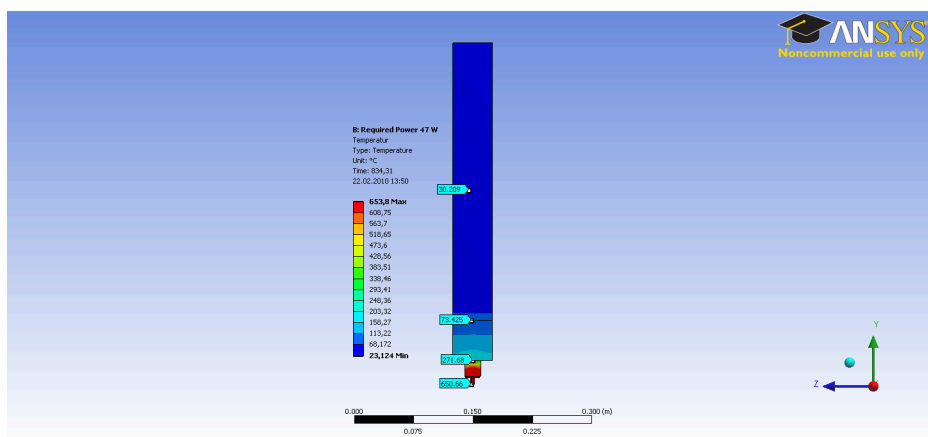
Figure B.5: Heating of the first studied configuration of the loading-shaft-indenter system
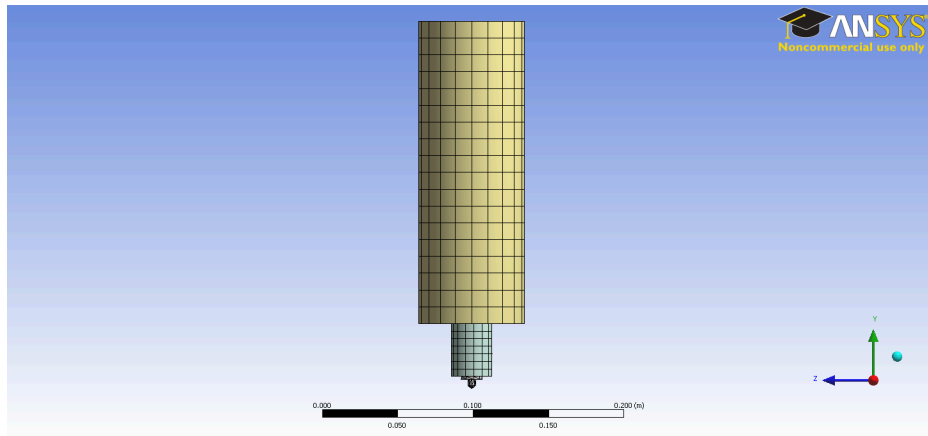
Figure B.6: Mesh of the final selected loading-shaft model with an integrated heater

B.3 Heating of the sample holder
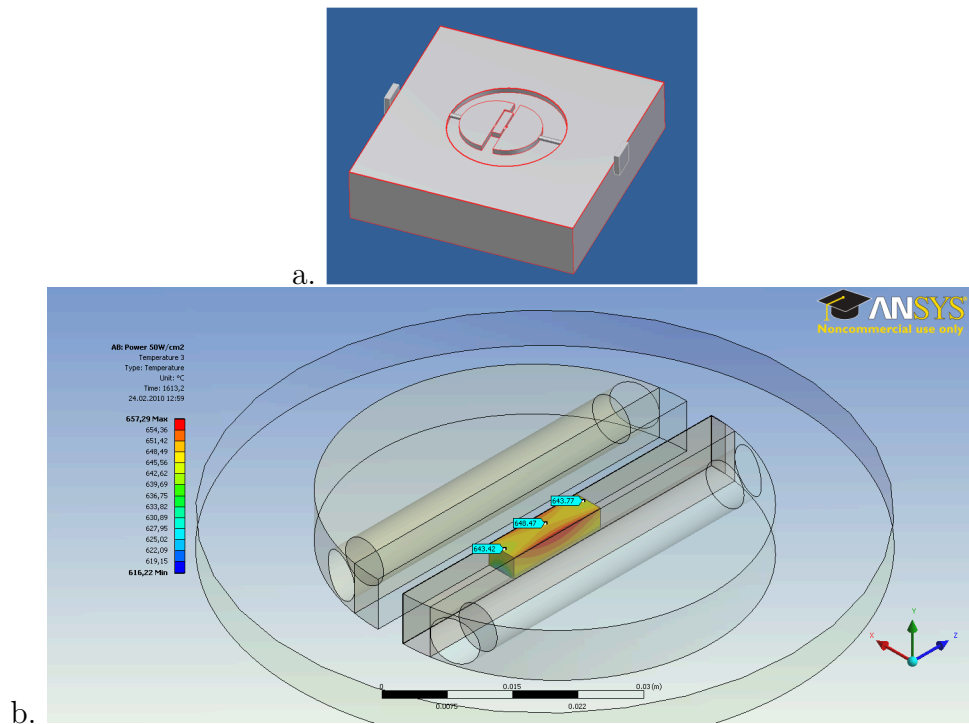
Figure B.7: (a) Concept of the heating stage-sample holder (b) Corresponding heating of the sample
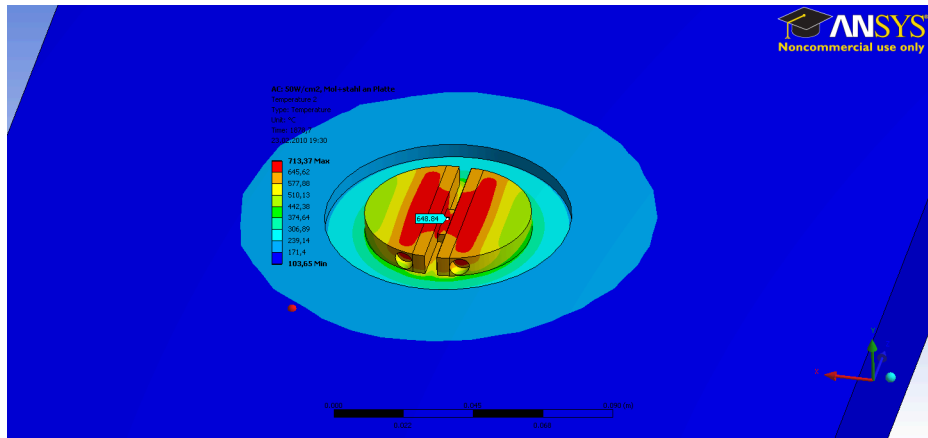
Figure B.8: Heating of the first studied configuration of the sample heating stage
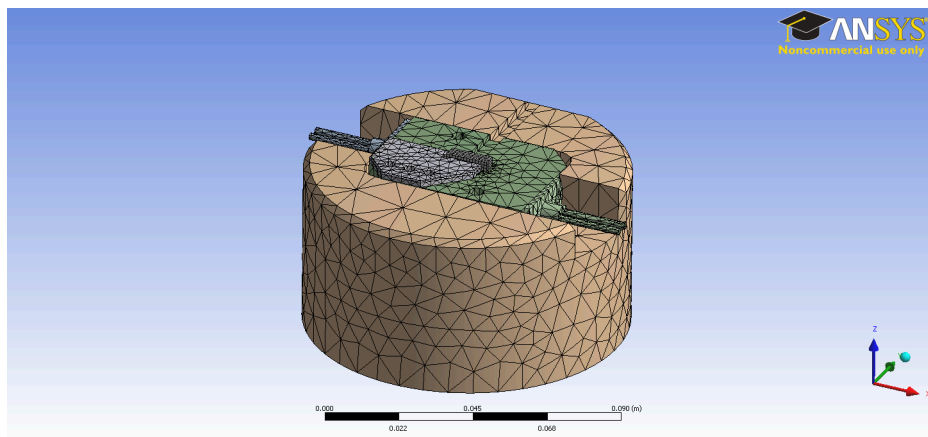
Figure B.9: Mesh of the final selected sample-heating stage model
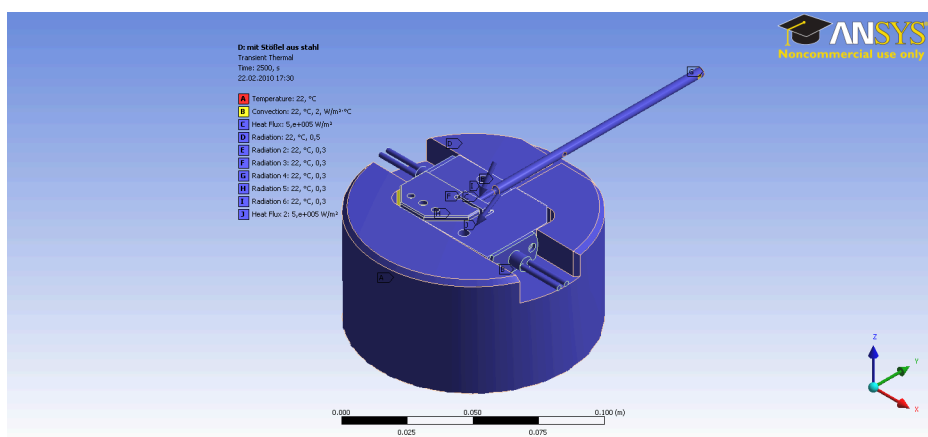
Figure B.10: Boundary conditions of the final selected sample-heating stage model
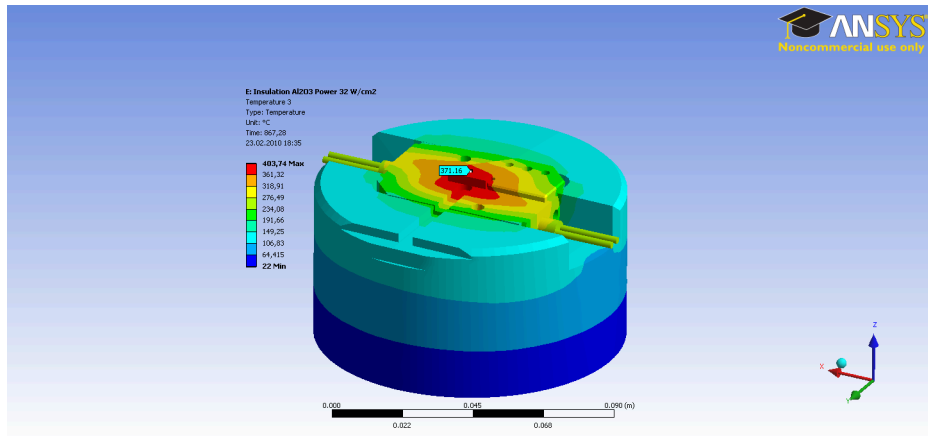
Figure B.11: Heating of the sample with a Al_2O_3 insulation at $32\,\mathrm{W/cm2}$
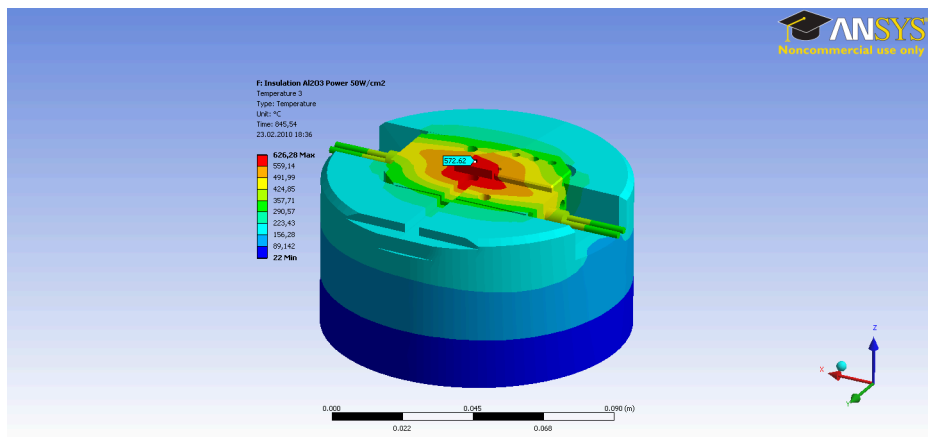
Figure B.12: Heating of the sample with a Al_2O_3 insulation at $50\,\mathrm{W/cm2}$
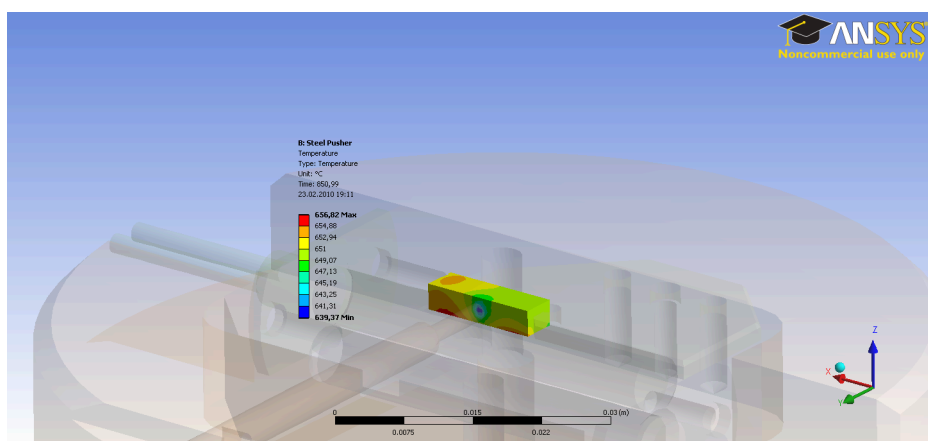
Figure B.13: Temperature distribution in the sample considering a pusher made of steel

Appendix C

Appendix: Specification of Components for the Indentation Facility

C.1 Camera specifications

SENSOR

Sensor	Cypress CMOS
Type	CMOS Rolling Shutter
Resolution	2208(H) x 3000(V) Color & Mono
Pixel Pitch	3.5 μm x 3.5 μm
Active Area	7.73 mm x 10.5 mm - 13.1 mm diagonal
Peak QE	25 % (mono) 24 % (color)
Max Datarate	40 MHz

COMPUTER & OPERATING SYSTEM

Processor	2.0 GHz or better
Memory	512 MB min. 1 GB recommended
Operating System	Windows 2000, XP and Vista (32bit)
Hard Drive Space	75 MB

POWER REQUIREMENTS

Voltage Req.	FireWire/GigE 8-32 V DC - USB 5 V DC
Power Req. PL-B781	FireWire 3.6 W, USB 3.2 W, GigE 4.6 W
Power Req. PL-B782	FireWire 4.6 W, USB 4.0 W, GigE 5.6 W

ENVIROMENTAL & REGULATORY

Compliance	FCC Class B, CE & RoHS
Shock & Vibration	300 G & 20 G (10Hz - 2KHz)
Operating Temp.	0°C to 50°C (non-condensing)
Storage Temp.	-45°C to 85°C

SOFTWARE

PixeLINK Capture OEM	Free Download (www.pixelink.com)
DirectShow (exl. GigE)	Bundled with PixeLINK Capture OEM
TWAIN	Bundled with PixeLINK Capture OEM
SDK	API, sample code and LabVIEW wrappers
DCAM 1394 Compliance	IIDC version 1.31

CAMERA CONTROLS & FEATURES

Auto & Manual White Balance, Color Temperature, Gain, Brightness (Dark Offset), Gamma, Saturation, Region of Interest (ROI), Histogram, Binning, Averaging, Resampling, Image Flip & Rotate, Programmable LUT, In-Camera Defective Pixel & Color Correction, Callbacks (Image Filters), FFC (Gain & Offset).

FRAME RATES

Resolution	Free Running Mode	Triggered Mode
2208 x 3000	5	4.9
2048 x 1536	11	10
1920 x 1080	16	15
1280 x 1024	25	22
640 x 480	89	75

Frame rates will vary based on host system and configuration

Specifications are subject to change without notice

PERFORMANCE SPECIFICATIONS *

Responsivity	Mono 4.4 DN/(nJ/cm²)
	Color 4 DN/(nJ/cm²)
FPN	Mono <1 % Color <1.5 %
PRNU	Mono <2 % Color <3 %
Read Noise	<1 DN
Dynamic Range	60 dB
Bit Depth	8 & 10-bit
Color Data Formats	Bayer 8, Bayer 16 and YUV422
Mono Data Formats	Raw, Mono 8 and Mono 16
Exposure Range	63 μs to 2 seconds free running
	63 μs to 2 seconds triggered
Gain	0 dB to 20.5 dB in 14 increments

*PL-B781 Settings: Typical values with 40ms integration time, 0dB gain, FFC on, 10-bit mode
*PL-B782 Settings: Typical values with 100ms integration time, 0dB gain, FFC on, 10-bit mode

MECHANICALS

Dimensions	102 x 50 x 41 mm (straight)
	110 x 50 x 41 mm (right angle)
Weight	Straight: 210 g - Right Angle: 264 g
Mounting	4 M3 threaded holes in front plate &
	4 M3 threaded holes in camera case
Tripod Mount	1/4" - 20 mount (optional)
Status LED	Amber - Start-up, Green - Idle or streaming
	Red - Warning or failed status
Lens Mount	C & CS-Mount, 1" optical format

INTERFACES

Interface / Date rate /	IEEE 1394A (2) / 400 Mbit / 6-pin
Connector	GigE / 1000 Mbit / RJ-45
	USB 2.0 / 480 Mbit / Type B
Trigger Connector	9-pin Micro D
Trigger Modes	Free running, software, hardware
Trigger Input	Optically isolated 5-12V DC @ 4-11 mA
GPO/Strobe	2 Optically Isolated - Maximum 40V DC
	differential. Maximum 15 mA

For more information, visit: http://www.pixelink.com/help

PIN OUTPUT DESCRIPTION

Pin   Pin Name & Function

1   POWER cable power, FireWire/GigE 8-32 V DC - USB 5 V DC
2   Gp2+ Positive terminal of GPO 2
3   Gp2- Negative terminal of GPO 2
4   Gp1+ Positive terminal of GPO 1
5   Gp1- Negative terminal of GPO 1
6   TRIGGER + Positive terminal of trigger input
7   TRIGGER - Negative terminal of trigger input
8   (no connection)
9   GROUND Logic and chassis ground

1 2 3 4 5

6 7 8 9
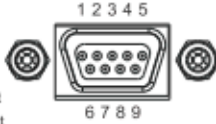
Figure C.1: Pixelink Camera specifications (from Edmund Optics)

C.2 Objective specifications

<u>Specifications</u>
Type: Maksutov Cassegrain Catadioptric
Working Range: 15 cm (6 inches) to 35 cm (14 inches), subject plane to front element.
Numerical Aperture:

Working Distance	N.A.	f/no
33.5 cm (14 inches)	.083	6.0
25.4 cm (10 inches)	.115	4.3
15 cm (6 inches)	.142	3.5

Resolution: 1.1 microns at 15 cm (6 inches).
Magnification: To 34 times at image plane.
Format: Diffraction Limited Field 12 mm.

<u>Optics</u>
Corrector Lens: BK7, Magnesium Fluoride Coated, 63 mm (2.5 inch) diameter.
Primary Mirror: Pyrex, Aluminum Coated, SiO overcoated 104 mm (4.1 inch) diameter.
Secondary Mirror: R1 Surface of Corrector, Aluminum Coated, 16 mm (.63 inch) diameter.
Baffling: Helical in central tube, all interior surfaces anti-reflection coated.

<u>Mechanical</u>
Barrel: Aluminum, machined from seamless stock, threaded lens cell black anodized.
                         Length 32 cm (12.6 inches), outside diameter 11.4 cm (4.5 inches), weight 2.27 kg (5 lbs).
Rear Closure Plate: Aluminum with stainless steel main tube holder plate, adjustable centering.
Focusing Mechanism: Mirror thimble integral with stainless steel sliding tube. Slides on fixed, stainless steel light baffle tube (centerless ground). Conical s.s. spring loaded Focus rod s.s. 303, precision ground, 24 TPI; integrated inside control box.
Control Box: Machined aluminum, selectable axial or 90û port. Internal beamsplitter standard flickknob controlled.
Knobs: Aluminum, 24S-T4, corrosion resistant, stainless steel shafts and levers.
Mount: Full barrel length, 1/4" - 20 and 3/8" -16 mounting holes.

Figure C.2: Specifications of the long-working-distance-microscope (from Questar)

C.3   Laser specifications

CDRH Class	1-5mW, Class IIIa; 10mW, Class IIIb, CDRH certified with key box
Max. Output Power	1mW, 5mW, or 10mW options
Typical Output Power	~75% of max output power
Wavelength	532nm±1nm
Beam Diameter	1.4 - 1.7mm diameter at exit of laser, at $1/e^2$
Beam Divergence	0.5 - 0.6mrad at $1/e^2$
Line Width, Focused Spot	<0.001" (25 microns) user adjustable
Focusing Distance	Face of module past collimation
Dimensions	
Module Only	0.750" (19.05mm) Diameter
Projection Head	0.734" (18.64mm) Diameter
Length	See Diagram
Bore Sighting (Beam vs. Housing Alignment)	< 3mrad, focus
Operating Temperature	15°C to 35°C (59°F to 95°F)
Frequency Drift	0.25nm/°C
ESD Protection	+8,000 volts
Diode MTBF, calculated	>10,000 hours
Current Draw	65 - 400mA, varies with model
Input Voltage	5 - 6V DC
Power Supply	220V AC, wall transformer (included)
Weight	200g
Housing Material	Black anodized aluminum

Figure C.3: Green laser diode module specifications (from Edmund Optics)

C.4 Heating-system specifications

Specifications

Line Voltage/Power
- All voltage levels represent minimums and maximums
- 85 to 264V~(ac), 47 to 63Hz
- 20 to 28V~(ac), +10/-15 percent; 50/60Hz, ±5 percent
- 12 to 40V⎓(dc)
- 10VA maximum power consumption
- Data retention upon power failure via nonvolatile memory
- Compliant with SEMI F47-0200, Figure R1-1 voltage sag requirements @ 24V~(ac) or higher

Environment
- -18 to 65°C (0 to 149°F) operating temperature
- -40 to 85°C (-40 to 185°F) storage temperature
- 0 to 90 percent RH, non-condensing

Accuracy
- Calibration accuracy and sensor conformity: ±0.1 percent
  of span, ±1°C @ the calibrated ambient temperature and rated line voltage
  • Type S, 0.2 percent
  • Type T, below -50°C; 0.2 percent
- Calibration ambient temperature @ 25°C ±3°C (77°F ±5°F)
- Accuracy span: 540°C (1000°F) minimum
- Temperature stability: ±0.1°C/°C (±0.1°F/°F) rise in ambient maximum

Agency Approvals
- UL®/EN 61010 Listed
- ANSI/ISA 12.12.01-2007 Class 1 Division 2 Groups A, B, C, D, Temperature Code T4A.
- UL® 50, NEMA 4X, EN 60529 IP66
- CSA C22.2 No. 24 File 158031
- RoHS, W.E.E.E.
- SEMI F47-0200

Controller
- User selectable heat/cool, on-off, P, PI, PD, PID or alarm action
- Auto-tune control algorithm
- Control sampling rates: input = 10Hz, outputs = 10Hz
- Input and output capacity per controller type ordering information

Serial Communications
- Isolated communications
- Standard Bus Configuration Protocol

Wiring Termination—Touch-Safe Terminals
- Input, power and controller output terminals are touch safe removable 12 to 22 AWG
- Use 75°C, Cu conductor only

Universal Input
- Thermocouple, grounded or ungrounded sensors
- >20MΩinput impedance
- Maximum of 2KΩ source resistance
- RTD 2- or 3-wire, platinum, 100Ω @ 0°C calibration to DIN curve (0.00385 Ω/Ω/°C)
- Process, 4-20mA @ 100Ω, or 0-10V⎓(dc) @ 20kΩ input impedance; scalable

Functional Operating Range
- Type J: -210 to 1200°C (-346 to 2192°F)
- Type K: -200 to 1370°C (-328 to 2500°F)
- Type N: -200 to 1300°C (-328 to 2372°F)
- Type S: -50 to 1767°C (-58 to 3214°F)
- Type T: -200 to 400°C (-328 to 750°F)
- RTD (DIN): -200 to 800°C (-328 to 1472°F)
- Process: -1999 to 9999 units

Output Hardware
- Switched dc, 22 to 32V⎓(dc) with a maximum of 40 mA supply current available.
- Open collector, maximum sink current 100 mA, @ 30V⎓(dc)
- Solid state relay (SSR), Form A, 0.5A @ 24V~(ac) minimum, 264V~(ac) maximum, opto-isolated, without contact suppression
- Electromechanical relay, Form C, 5A, 24 to 240V~(ac) or 30V⎓(dc) maximum, resistive load, 100,000 cycles at rated load
- Electromechanical relay, Form A, 5A, 24 to 240V~(ac) or 30V⎓(dc) maximum, resistive load, 100,000 cycles at rated load
- NO-ARC relay, Form A, 15A, 24 to 240V~(ac), no V⎓(dc), resistive load, 2 million cycles at rated load
- Universal process:
  - 0 to 10V⎓(dc) into a minimum 1,000Ω load
  - 4 to 20mA into maximum 800Ω load

Operator Interface
- Dual 4 digit, 7 segment LED displays
- Typical display update rate 1Hz
- Advance, infinity, up and down keys plus an EZ-KEY key (not available in 1⁄32 DIN)
- EZ-KEY automatically programmed as an Auto/Manual transfer mode function.

Figure C.4: Properties of the PID controller (from Watlow)

C.5   Vacuum-system specifications

Technische Daten	HiPace™ 10 mit TC 110, DN 25
Anschlussflansch (Ausgang)	DN 16 ISO-KF / G1/8"
Anschlussflansch (Eingang)	DN 25
Drehzahl ±2%	90000 min^{-1}
Enddruck mit OnTool™ DryPump	< 5 · 10^{-5} mbar
Gasdurchsatz bei Enddrehzahl für Ar	0,37 mbar l/s
Gasdurchsatz bei Enddrehzahl für H_2	2,78 mbar l/s
Gasdurchsatz bei Enddrehzahl für He	0,48 mbar l/s
Gasdurchsatz bei Enddrehzahl für N_2	0,37 mbar l/s
Gewicht	1,8 kg
Hochlaufzeit	0,9 min
Kompressionsverhältnis für Ar	2,5 · 10^7
Kompressionsverhältnis für H_2	3 · 10^2
Kompressionsverhältnis für He	3 · 10^3
Kompressionsverhältnis für N_2	3 · 10^6
Kühlart, Standard	Konvektion
Saugvermögen für Ar	11,5 l/s
Saugvermögen für H_2	3,7 l/s
Saugvermögen für He	6 l/s
Saugvermögen für N_2	10 l/s
Schalldruckpegel	< 45 dB (A)
Schnittstellen	RS-485, Remote
Schutzart	IP 54
Vorvakuum max. für N_2	25 mbar
Zulässiges Magnetfeld max.	3 mT

Figure C.5: Properties of the Vacuum-Pumps system (from the manufacturer Pfeiffer)

C.6   Glass specifications

Main Specifications			
	Super Precision	**High Precision**	**Standard Precision**
Material	BK7 grade A optical glass		
Size	Dia 5.0~80.0mm x thickness 0.5~10.0mm		
Diameter Tolerance	+0/-0.10mm		
Thickness Tolerance	±0.10mm		
Clear Aperture	> 85%		
Flatness (@633nm)	1/10	1/4	1 1 per 25mm
Parallelism	<10 arc seconds	<30 arc seconds	<1 arc minute
Surface Quality (S/D)	20/10	40/20	60/40
Bevel	0.25mm x 45°		
Coating	Available upon request		

Figure C.6: Glass specifications (from the manufacturer Red-Optronics), the "Super precison" category is considered to be suitable for the present application

C.7 Anti vibration stage specifications

Vibration Isolation System	
Frequency Range:	1 Hz – ∞
Isolation Performance:	> 5 Hz = 25 dB, > 10 Hz = 35 dB
Sensors:	Piezo-electric accelerometers sense horizontal and vertical vibrations
Actuators:	8 electro-dynamic transducers
Overload Indication:	16 LEDs indicating overload conditions in input and output stages
System Noise:	Less than 50 ng per root Hz from 0.1 to 200 Hz in any direction
Static Compliance:	Load-dependent: 8 µm/N in any direction at full load, 25 µm/N in any direction at small loads
Control Electronics:	Compact external control unit with isolation on/off switch
Standard Versions and Dimensions — Customised systems available on request	
MOD-Sandwich 800-4.0	Maximum load: 600 kg Dimensions: 800 x 800 x 130 mm³ Correction Forces: vertical max.: ± 16 N, horizontal max.: ± 8 N
MOD-Sandwich 1000-4.0	Maximum load: 600 kg Dimensions: 1000 x 800 x 130 mm³ Correction Forces: vertical max.: ± 16 N, horizontal max.: ± 8 N
MOD-Sandwich 1000-4.4	Maximum load: 750 kg Dimensions: 1000 x 800 x 130 mm³ Correction Forces: vertical max.: ± 16 N, horizontal max.: ± 8 N
MOD-Sandwich 1000-6.0	Maximum load: 900 kg Dimensions: 1000 x 800 x 130 mm³ Correction Forces: vertical max.: ± 24 N, horizontal max.: ± 12 N
MOD-Sandwich 1000-6.4	Maximum load: 1050 kg Dimensions: 1000 x 800 x 130 mm³ Correction Forces: vertical max.: ± 24 N, horizontal max.: ± 12 N
MOD-Sandwich 1000-8.0	Maximum load: 1200 kg Dimensions: 1000 x 800 x 130 mm³ Correction Forces: vertical max.: ± 32 N, horizontal max.: ± 16 N
Electrical Properties	
Power Requirements:	90-260 V AC, 98-338 V DC; 12 W typically, max. 50 W
Interfaces:	Analog diagnostic output

Figure C.7: Anti vibration stage specifications

Curriculum Vitæ

Personal Data:

Name:	Irène SACKSTEDER
Birthday:	1983-11-09
Birthplace:	Marseille, France
Nationality:	French

Education:

2007–2011:	Ph.D. thesis in supervision of the Karlsruhe Institute of Technology (KIT), Karlsruhe, Germany. The research work was accomplished at the Institute for Applied Materials (IAM) of the KIT.
2003–2006:	Three years at the engineering school ENSIB in Bourges, France. Specialization in the industrial risks management (Engineer diploma & Master degree of science in mechanical engineering).
2001–2003:	Two years at the University of Perpignan and Montpellier, France. Specialization in mathematical, physical and chemical sciences.
2001:	Scientific A-Levels (with distinction) at the Lycée Jean-Lurçat at Perpignan, France.